technische universität
dortmund

Arbeit zur Erlangung des akademischen Grades
Master of Science

Dynamic mean-field theory for spin ensembles

Timo Gräßer
geboren in Lüdenscheid

2019

Lehrstuhl für Theoretische Physik Ia
Fakultät Physik
Technische Universität Dortmund

Erstgutachter:	Prof. Dr. Götz S. Uhrig
Zweitgutachter:	Priv.-Doz. Dr. Jörg Bünemann
Abgabedatum:	19. Dezember 2019

Abstract

This thesis is aimed at establishing the dynamic mean-field theory as a method to describe large and thermally disordered spin ensembles. To this end, the theory is expounded in the context of an ongoing experiment, in which the dynamics of electronic defect spins on a diamond surface is investigated. Based on the experimental conditions, the Hamiltonian for a dipolar spin ensemble subjected to a global static field and a local magnetic noise is set up. Subsequently, a particular spin is considered and its local environment is substituted by a mean-field. A key aspect of the presented approach is that the mean-field is interpreted to be a Gaussian random variable with second moments following from quantum-mechanical expectation values of the original spin environment. This consideration leads to a self-consistency problem connecting the autocorrelation functions of the particular spin to those of the mean-field. Solving this issue by iteration requires only minor numerical effort. The finally obtained results are in a remarkable agreement with the experimental data supporting the settled theory. Moreover, this thesis confirms that the considered magnetic noise induces an enormous slowdown in the longitudinal spin decay relative to the transversal spin decay.

Kurzfassung

Im Rahmen dieser theoretischen Arbeit wird die dynamische Molekularfeldtheorie als Methode zur Erfassung großer, thermisch ungeordneter Spin Ensembles etabliert. Zu diesem Zweck wird die Theorie detailliert im Kontext eines aktuellen Experiments erläutert, in welchem die Dynamik von elektronischen Defektspins auf einer Diamantoberfläche erforscht wird. In Anlehnung an experimentelle Gegebenheiten wird der Hamiltonoperator für ein dipolares Spinsystem betrachtet, das einem starken statischen Magnetfeld inklusive einem lokalen magnetischen Rauschen ausgesetzt ist. Anschließend wird ein einzelner Defektspin separat betrachtet und dessen lokale Umgebung durch ein Molekularfeld ersetzt. Ein zentraler Aspekt des präsentierten Ansatzes ist das Molekularfeld als Gaußsche Zufallsvariable zu interpretieren, deren Momente mit quantenmechanischen Erwartungswerten der ursprünglichen Spinumgebung verknüpft sind. Daraus ergibt sich schließlich ein Selbstkonsistenzproblem für die Autokorrelationsfunktionen von Spin und Molekularfeld, die unter geringem numerischen Aufwand ermittelt werden können. Die resultierenden Ergebnisse stimmen sehr gut mit den experimentellen Daten überein und stützen damit die theoretischen Grundlagen. Außerdem wird in dieser Arbeit bestätigt, dass das berücksichtigte magnetische Rauschen eine erhebliche Verlangsamung des longitudinalen Zerfalls relativ zum transversalen Zerfall der Spinpolarisation induziert.

Contents

1 Introduction

Over the past decades, many research areas dealing with spin systems, in general, gained enormous attention due to applications in various contexts, reaching from physics and chemistry to quantum computing science, life science or even medicine. As an intrinsic fundamental particle property, spin interacts with the observable reality through an associated magnetic moment. Therefore, it can be elementarily exploited in several ways, e.g., as a reporter for local sensing targets, or as a quantum bit in the sense of quantum computing. In both cases, the spin has to be confined in some environment so that it is spatially localized and therefore can be readout properly as well as manipulated. For most applications, the environment forms a rather deleterious entity because it interacts with the spin and thereby lowers its decoherence time, i.e. the time where its initial alignment is conserved. Thus, it is indispensable to study the environmental coupling to the spin. In theory, this often requires to consider a large interacting spin ensemble - an issue that cannot be solved without applying fundamental approximations.

An example of this is a confined electron or hole in a quantum dot, which is said to form a promising candidate for a quantum bit [1, 2]. The environment of the spin is in this case given by a bath of nuclear spins coupling to it through the hyperfine interaction [3, 4]. For potential applications concerning quantum computing, it is of essential importance to understand the dynamics and, in particular, the decoherence induced by this interaction. To suitably realize the physical situation in a quantum dot, the central spin model originally introduced by Gaudin can be employed [5, 6]. Solving this model appears to be challenging due to a large number of around $10^4 - 10^6$ nuclear spins that are required to reflect the experimental reality [4]. Indeed, many various approaches have been applied to it in the past [3, 7–10]. It is worth mentioning that the bare central spin model does not incorporate a dipole-dipole coupling between the nuclear spins. For most considerations, this is unproblematic because the dipole-dipole interaction is by far weaker than the hyperfine interaction. However, for fairly long times it should be taken into account, e.g., with aid of a mean-field approach [11].

Due to their potential for highly-sensitive magnetic sensors the research of nitrogen-vacancy centers in diamond was highly pushed forward in recent years [12–14]. Their enormous advantages to be used as quantum reporters are not only established through thermal stability of their spin states up to the room temperature, but also due to their optical properties allowing for optically detected magnetic resonance (ODMR) [15–18]. As the name implies, a nitrogen-vacancy (NV) center consists of a substitutional nitrogen atom which is adjacent to a vacancy in the diamond lattice [18]. It carries a single spin of $s = 1$ with a low-energy state $m_s = 0$ and two degenerate excited states $m_s = \pm 1$ [18].

For most applications in the subject of magnetic sensing, the NV center needs to be close to the diamond surface ($< 10\,\mathrm{nm}$) so that proximity to sensing targets is given [19]. However, several experiments observed that the coherence time of shallow NV spins is considerably reduced due to the presence of other spins at the surface [19–22]. Those result from paramagnetic defects and carry an electronic spin of $s = \frac{1}{2}$ including a Landè factor of $g \approx 2$ for properly prepared diamond surfaces [20, 23]. Due to the lowered coherence time, the exploitability of shallow NV centers is considerably decreased so that they become uninteressant for potential applications. To prevent this, one could either try to mitigate the induced decoherence, or even employ the surface spins for spin amplification [23, 24]. For several goals, it is inevitable to gain insight into the surface-spin dynamics so that it can be influenced properly.

An ongoing experiment [25] intends to examine the dynamics at ambient conditions through measuring the surface-spin polarizations over time. To be able to address the surface spins and a single NV spin at different resonance frequencies, the experimental setup contains a strong static magnetic field. In fact, the spin polarizations are measured in the reference frame rotating at the surface-spin Larmor frequency induced by this field. The experimental results in transversal as well as in longitudinal direction are shown in Fig. 1.1. What strikes is the vast difference between the decay of both polarizations, which is reasoned due to a magnetic noise induced by surface-near proton spins [25]. This theoretical thesis intends, amongst others, to rebuild the experimental situation employing a dipole-dipole model expanded by the strong static field and the observed noise. The model is treated utilizing a mean-field-based approach.

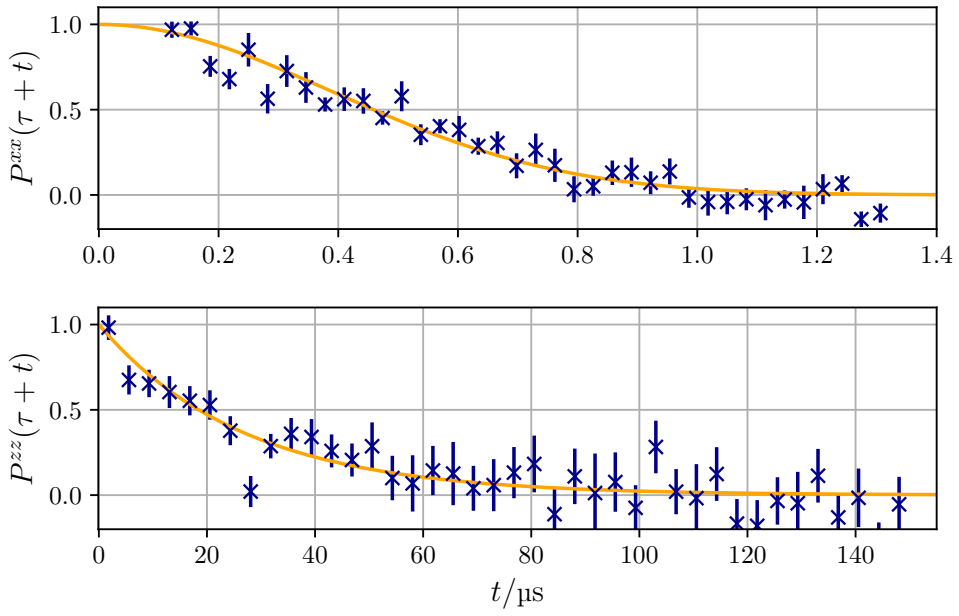

Figure 1.1: Transversal and longitudinal spin polarizations, $P^{xx}(\tau + t)$ and $P^{zz}(\tau + t)$, of dipolar surface spins on a diamond surface [25].

It is especially the non-perturbative nature that impedes the most approximations trying to keep up with strongly correlated many-body systems, such as spin lattices. In these cases mean-field theories (MFT) often score with their key property to be exact in the limit of infinite spatial dimensions or number of nearest-neighbors, respectively, because this feature allows for accessing the systems from a specific limit. Certainly, one of the most familiar examples for a mean-field approach is the Weiss MFT applied to the ferromagnetic Ising model [26, 27]. The main idea is to replace the environment of a single spin by a static averaged value reducing the lattice model to an effective single-site model with very few degrees of freedom. To study dynamics, the classical MFT is insufficient, though, because any fluctuations are frozen out by the static substitution. In this sense, the search for an extended MFT incorporating dynamical features is certainly motivated. For strongly correlated fermionic systems such a dynamic mean-field theory (DMFT), which is somehow an extension of the Hartree-Fock theory, was elaborated some decades ago [26–28]. A spin version of this (S-DMFT) was considered in Ref. [29] by means of a bosonic representation and with a focus on ordered phases. It is also worthwhile mentioning that several studies in the topic of quantum "spin glasses" are strongly related to a S-DMFT, but they rather deal with phase transitions [30–33]. In contrast, this thesis aims at establishing S-DMFT for thermally disordered spins and represented in spin-space, while applying it to the elucidated experimental scenario.

The structure is organized as follows. At first, the theoretical foundation is built up in chapter 2. Thereby, S-DMFT is established by applying it to a system of dipolar surface spins subjected to a strong static field and a local magnetic noise based on the experiment. The approach leads to a semiclassical Hamiltonian accompained by a self-consistency problem allowing for feasible numerical computation. At the end, the considered system is studied in the zero-field limit utilizing the elaborated theory. In chapter 3, the numerical procedure to solve the self-consistency problem through iteration is furnished. Moreover, it is expounded on how to sample dynamic Gaussian random variables and how to compute time evolution operators efficiently. Subsequently, numerical results are presented in chapter 4. After providing an error analysis in the beginning, the autocorrelations resulting in the strong-field regime are shown and compared with the received experimental data. Finally, the results in the zero-field limit are also presented and discussed. The last chapter, 5, summarizes the established theory and the obtained results to propose an ambitious outlook at the end.

2 Theory

In the introduction we described an experimental background concerning dipolar surface spins on a diamond surface. In particular, we emphasized that their autocorrelation functions[1] are interesting due to considerably different timescales of the transversal and longitudinal decays. The current chapter establishes a fundamental theoretical model by which we capture the dynamics of the surface spins. At first, we consider a strong external magnetic field acting on a spin ensemble. After setting up the Hamiltonian, we turn to a rotating frame and apply a rotating wave approximation. Subsequently, a detailed description of a dynamic mean-field approach for the considered spin system is provided. We formulate a self-consistency problem linking the mean-field autocorrelations to the single-spin autocorrelations. Moreover, the system and thus the self-consistency problem is extended to include a magnetic field noise because this is observed experimentally. At the end, we also treat the case of a zero external field by same manner. Henceforth, operators and matrices are represented by boldface symbols and we set $\hbar = 1$.

2.1 Spin ensemble subjected to a static magnetic field

To build the model, we start by formulating the fundamental Hamiltonian for both the dipole-dipole coupling and the external field coupling. For an ensemble of N pairwise interacting spin-$\frac{1}{2}$ the Hamiltonian is given by [34]

$$\boldsymbol{H}_{\mathrm{DD}} = \sum_{0\leq i<j\leq N-1} J\left(R_{ij}\right)\left(R_{ij}^2\left(\vec{\boldsymbol{S}}_i\cdot\vec{\boldsymbol{S}}_j\right) - 3\left(\vec{\boldsymbol{S}}_i\cdot\vec{R}_{ij}\right)\left(\vec{\boldsymbol{S}}_j\cdot\vec{R}_{ij}\right)\right). \tag{2.1}$$

The distance R_{ij} between two spins i and j is not an operator in contrast to the spin operators $\boldsymbol{S}_i$ und $\boldsymbol{S}_j$ because we consider localized spins. Furthermore, we remind the reader that the spins and hence the distance vectors are located on a planar surface. The coupling constant reads [34]

$$J(R) = \frac{\mu_0\gamma_{\mathrm{s}}^2}{4\pi R^5}, \tag{2.2}$$

where we call γ_{s} the gyromagnetic ratio of the spins. In line with experimental observations [20, 25] we adopt

$$\gamma_{\mathrm{s}} = g_{\mathrm{s}}\mu_{\mathrm{B}} \approx 2\mu_{\mathrm{B}}. \tag{2.3}$$

[1] In our case ($s = \frac{1}{2}$), they are simply given by a quarter of the spin polarizations.

According to (2.1) and (2.2) we see that the interaction strength decreases with $1/R^3$.

In addition to the dipole-dipole Hamiltonian we consider an external static and homogeneous magnetic field B. Per definition we choose the z-axis parallel to this field leading to the Zeeman coupling

$$\boldsymbol{H}_{\mathrm{Z}} = \gamma_{\mathrm{s}} B \sum_{i=0}^{N-1} \boldsymbol{S}_i^z. \tag{2.4}$$

Moreover, we assume an angle α between the normal vector of the surface and the magnetic field so that the z-axis is not perpendicular to the surface. The total system underlying the Hamiltonian

$$\boldsymbol{H}_{\mathrm{T}} = \boldsymbol{H}_{\mathrm{DD}} + \boldsymbol{H}_{\mathrm{Z}} \tag{2.5}$$

is illustrated in Fig. 2.1.

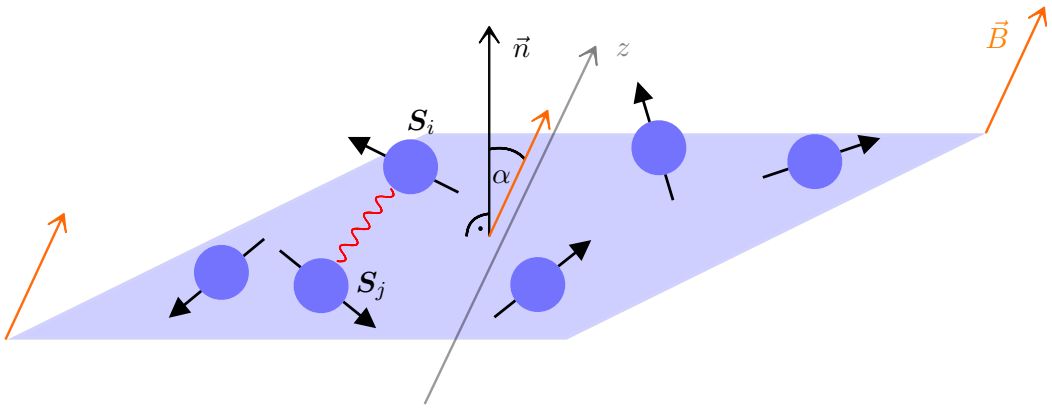

Figure 2.1: Schematic illustration of localized surface spins subjected to an external magnetic field. Exemplarily, the red wavy line indicates the interaction between a pair of spins. Corresponding to (2.1) such an interaction exists between all pairs of spins.

Due to the external field the spins precess at the Larmor frequency

$$\omega_{\mathrm{L}} = \gamma_{\mathrm{s}} B \tag{2.6}$$

around the z-axis. As explained in the introduction, the studied autocorrelation functions are experimentally measured in the Larmor rotating frame. For a comparison between numerical and experimental results it is necessary to turn to this frame. Viewed from a resting laboratory frame the time evolution of the spin operators $\boldsymbol{S}_i$ is based on $\boldsymbol{H}_{\mathrm{T}}$. An observer in a reference frame rotating at ω_{L} views an additional time evolution based on $-\boldsymbol{H}_{\mathrm{Z}}$, because from the obervers point of view the spins additionaly rotate at ω_{L} against the rotational direction. Therefore, the autocorrelation functions in the Larmor rotating frame obey

$$\langle \boldsymbol{S}^{\alpha}_{\mathrm{rot}}(t)\boldsymbol{S}^{\alpha}_{\mathrm{rot}}(0)\rangle = \langle \boldsymbol{U}_{\mathrm{Z}}^{\dagger}(-t)\boldsymbol{U}_{\mathrm{T}}^{\dagger}(t)\boldsymbol{S}^{\alpha}(0)\boldsymbol{U}_{\mathrm{T}}(t)\boldsymbol{U}_{\mathrm{Z}}(-t)\boldsymbol{U}_{\mathrm{Z}}^{\dagger}(0)\boldsymbol{S}^{\alpha}(0)\boldsymbol{U}_{\mathrm{Z}}(0)\rangle \tag{2.7a}$$

$$= \langle \boldsymbol{U}_{\mathrm{Z}}(t)\boldsymbol{U}_{\mathrm{T}}^{\dagger}(t)\boldsymbol{S}^{\alpha}(0)\boldsymbol{U}_{\mathrm{T}}(t)\boldsymbol{U}_{\mathrm{Z}}^{\dagger}(t)\boldsymbol{S}^{\alpha}(0)\rangle, \tag{2.7b}$$

$$= \langle \boldsymbol{U}_{\mathrm{eff}}^{\dagger}(t)\boldsymbol{S}^{\alpha}(0)\boldsymbol{U}_{\mathrm{eff}}(t)\boldsymbol{S}^{\alpha}(0)\rangle, \tag{2.7c}$$

where we introduced the effective time evolution operator

$$\boldsymbol{U}_{\text{eff}}(t) = \boldsymbol{U}_{\text{T}}(t)\boldsymbol{U}_{\text{Z}}^{\dagger}(t) \tag{2.8}$$

and

$$\boldsymbol{U}_{\text{Z}}(t) = \mathrm{e}^{-\mathtt{i}\boldsymbol{H}_{\text{Z}}t}, \qquad \boldsymbol{U}_{\text{T}}(t) = \mathrm{e}^{-\mathtt{i}\boldsymbol{H}_{\text{T}}t}. \tag{2.9}$$

With aid of the general differential equation

$$\mathtt{i}\partial_t \boldsymbol{U}_{\text{eff}}(t) = \boldsymbol{H}_{\text{eff}}(t)\boldsymbol{U}_{\text{eff}}(t) \tag{2.10}$$

one obtains the effective Hamiltonian[2]

$$\boldsymbol{H}_{\text{eff}}(t) = \boldsymbol{U}_{\text{Z}}(t)\boldsymbol{H}_{\text{T}}\boldsymbol{U}_{\text{Z}}^{\dagger}(t) - \boldsymbol{H}_{\text{Z}} = \boldsymbol{U}_{\text{Z}}(t)\boldsymbol{H}_{\text{DD}}\boldsymbol{U}_{\text{Z}}^{\dagger}(t). \tag{2.11}$$

Obviously, the dipole-dipole Hamiltonian is rotated backwards at frequency ω_{L}. This leads to a precession of the occurring spin operators according to

$$\vec{\boldsymbol{S}}_i(t) = \mathrm{e}^{-\mathtt{i}\omega_{\text{L}}t\,\boldsymbol{S}_i^z}\,\vec{\boldsymbol{S}}_i(0)\,\mathrm{e}^{\mathtt{i}\omega_{\text{L}}t\,\boldsymbol{S}_i^z} = \begin{pmatrix} \boldsymbol{S}_i^x\cos(\omega_{\text{L}}t) + \boldsymbol{S}_i^y\sin(\omega_{\text{L}}t) \\ \boldsymbol{S}_i^y\cos(\omega_{\text{L}}t) - \boldsymbol{S}_i^x\sin(\omega_{\text{L}}t) \\ \boldsymbol{S}_i^z \end{pmatrix}, \tag{2.12a}$$

wherein we have used

$$\mathrm{e}^{-\mathtt{i}\omega\,\boldsymbol{S}^{\alpha}}\;\boldsymbol{S}^{\beta}\;\mathrm{e}^{\mathtt{i}\omega\,\boldsymbol{S}^{\alpha}} = \Big(\cos(\omega) + \delta_{\alpha\beta}\left[1-\cos(\omega)\right]\Big)\boldsymbol{S}^{\beta} + \sum_{\gamma}\sin(\omega)\epsilon_{\alpha\beta\gamma}\boldsymbol{S}^{\gamma}. \tag{2.13}$$

Correspondingly, the effective Hamiltonian reads

$$\begin{aligned}\boldsymbol{H}_{\text{eff}} = \sum_{0\le i<j\le N-1} J\left(R_{ij}\right)\Bigg(& R_{ij}^2\left(\vec{\boldsymbol{S}}_i\cdot\vec{\boldsymbol{S}}_j\right) - 3R_{ij,z}^2\boldsymbol{S}_i^z\boldsymbol{S}_j^z - \frac{3}{2}R_{ij}^2\left(\boldsymbol{S}_i^x\boldsymbol{S}_j^x + \boldsymbol{S}_i^y\boldsymbol{S}_j^y\right) \\ & - 3\cos(\omega_{\text{L}}t)\boldsymbol{A}_{ij} - 3\sin(\omega_{\text{L}}t)\boldsymbol{B}_{ij} - 3\cos(2\omega_{\text{L}}t)\boldsymbol{C}_{ij} - 3\sin(2\omega_{\text{L}}t)\boldsymbol{D}_{ij}\Bigg)\end{aligned} \tag{2.14a}$$

$$\begin{aligned}= \sum_{0\le i<j\le N-1} J\left(R_{ij}\right)\Bigg(& \left(R_{ij}^2 - 3R_{ij,z}^2\right)\boldsymbol{S}_i^z\boldsymbol{S}_j^z - \frac{R_{ij}^2}{2}\left(\boldsymbol{S}_i^x\boldsymbol{S}_j^x + \boldsymbol{S}_i^y\boldsymbol{S}_j^y\right) \\ & - 3\cos(\omega_{\text{L}}t)\boldsymbol{A}_{ij} - 3\sin(\omega_{\text{L}}t)\boldsymbol{B}_{ij} - 3\cos(2\omega_{\text{L}}t)\boldsymbol{C}_{ij} - 3\sin(2\omega_{\text{L}}t)\boldsymbol{D}_{ij}\Bigg),\end{aligned} \tag{2.14b}$$

with

$$\boldsymbol{A}_{ij} = R_{ij,z}\boldsymbol{S}_i^z\left(R_{ij,x}\boldsymbol{S}_j^x + R_{ij,y}\boldsymbol{S}_j^y\right) + R_{ij,z}\boldsymbol{S}_j^z\left(R_{ij,x}\boldsymbol{S}_i^x + R_{ij,y}\boldsymbol{S}_i^y\right), \tag{2.15a}$$

$$\boldsymbol{B}_{ij} = R_{ij,z}\boldsymbol{S}_i^z\left(R_{ij,x}\boldsymbol{S}_j^y - R_{ij,y}\boldsymbol{S}_j^x\right) + R_{ij,z}\boldsymbol{S}_j^z\left(R_{ij,x}\boldsymbol{S}_i^y - R_{ij,y}\boldsymbol{S}_i^x\right), \tag{2.15b}$$

$$\boldsymbol{C}_{ij} = \tfrac{1}{2}\left(R_{ij,x}^2 - R_{ij,y}^2\right)\left(\boldsymbol{S}_i^x\boldsymbol{S}_j^x - \boldsymbol{S}_i^y\boldsymbol{S}_j^y\right) + R_{ij,x}R_{ij,y}\left(\boldsymbol{S}_i^x\boldsymbol{S}_j^y + \boldsymbol{S}_i^y\boldsymbol{S}_j^x\right), \tag{2.15c}$$

$$\boldsymbol{D}_{ij} = \tfrac{1}{2}\left(R_{ij,x}^2 - R_{ij,y}^2\right)\left(\boldsymbol{S}_i^x\boldsymbol{S}_j^y + \boldsymbol{S}_i^y\boldsymbol{S}_j^x\right) + R_{ij,x}R_{ij,y}\left(\boldsymbol{S}_i^y\boldsymbol{S}_j^y - \boldsymbol{S}_i^x\boldsymbol{S}_j^x\right). \tag{2.15d}$$

[2] The presented procedure corresponds to using the interaction picture. To this end, it is selected $\boldsymbol{H}_{\text{Z}}$ to be the non-perturbative and $\boldsymbol{H}_{\text{DD}}$ to be the perturbative part.

The first term in (2.1) is not affected by the precession, since both spins in the scalar product are rotated at the same frequency. Though, $\boldsymbol{H}_{\text{eff}}$ is time-dependent because the second term yields several terms oscillating at ω_{L} and $2\omega_{\text{L}}$. In the following section, we employ the common approximation to average the time dependence. Henceforth any sum over spin sites runs from 0 to $N-1$, if not explicitly restricted.

2.2 Rotating Wave Approximation

In general, a rotating wave approximation (RWA) is worth considering for systems, where two kinds of dynamics happen at essentially different timescales [35, 36]. Then, one may replace fast oscillations in the Hamiltonian by their temporal average to uncover the slow dynamics[3]. There it applies, the larger the difference between the timescales, the better the quality of the approximation. The RWA reveals to be suitable for our case, since the external magnetic field is strong leading to a fast Larmor precession in the considered experiment. To quantify this accuracy, we require a large Larmor frequency compared to the typical frequency of the dipole-dipole interaction, i.e.,

$$\omega_{\text{L}} = \gamma_{\text{s}} B \gg \omega_{\text{DD}} = J(R_{\text{DD}}) R_{\text{DD}}^2. \tag{2.16}$$

From the experiment we roughly estimate the typical dipole field from the typical interaction distance [25] according to

$$R_{\text{DD}} = 5\,\text{nm}, \tag{2.17a}$$
$$\omega_{\text{DD}} \approx 2.6\,\text{MHz}, \tag{2.17b}$$
$$B_{\text{DD}} \approx 15\,\mu\text{T}. \tag{2.17c}$$

Indeed, the experimental static magnetic field is approximately given by [25]

$$B \approx 0.13\,\text{T} \tag{2.18}$$

and hence four orders of magnitude larger than the dipole field strength. Thus we conclude that the RWA is justified.

Correspondingly, we replace the oscillating terms in the effective Hamiltonian (2.11) by their temporal average according to

$$\sin(\omega_{\text{L}} t) \to 0, \qquad \sin(2\omega_{\text{L}} t) \to 0, \tag{2.19a}$$
$$\cos(\omega_{\text{L}} t) \to 0, \qquad \sin(2\omega_{\text{L}} t) \to 0. \tag{2.19b}$$

[3] This corresponds to a first order truncation of the Magnus expansion [36, 37].

Hence, the approximated Hamiltonian reads

$$\boldsymbol{H}_{\text{eff}} \approx \sum_{i<j} J\left(R_{ij}\right)\left(\left(R_{ij}^2 - 3R_{ij,z}^2\right)\boldsymbol{S}_i^z\boldsymbol{S}_j^z - \frac{R_{ij}^2}{2}\left(\boldsymbol{S}_i^x\boldsymbol{S}_j^x + \boldsymbol{S}_i^y\boldsymbol{S}_j^y\right)\right) \tag{2.20a}$$

$$= \sum_{i<j} \tilde{J}_{ij}\left(4\boldsymbol{S}_i^z\boldsymbol{S}_j^z - 2\boldsymbol{S}_i^x\boldsymbol{S}_j^x - 2\boldsymbol{S}_i^y\boldsymbol{S}_j^y\right) \tag{2.20b}$$

$$= \frac{1}{2}\sum_{i\neq j} \tilde{J}_{ij}\left(4\boldsymbol{S}_i^z\boldsymbol{S}_j^z - 2\boldsymbol{S}_i^x\boldsymbol{S}_j^x - 2\boldsymbol{S}_i^y\boldsymbol{S}_j^y\right), \tag{2.20c}$$

where we introduced the shorthand

$$\tilde{J}_{ij} = \frac{1}{4}J\left(R_{ij}\right)\left(R_{ij}^2 - 3R_{z,ij}^2\right). \tag{2.21}$$

Due to the RWA we eliminated any time dependence and thereby simplified the problem essentially. However, a direct analytical or numerical treatment of the resulting Hamiltonian is still not accessible due to the large number of spins. Therefore, we justify and employ a dynamic mean-field approach in the upcoming section.

2.3 Dynamic mean-field theory for spins

2.3.1 Introduction of the local Overhauser fields

To pave the way for S-DMFT, we focus on the dynamics of one particular spin and argue that it represents the whole ensemble. At first, we introduce collective fields as

$$\vec{\boldsymbol{V}}_j = \sum_{\substack{i \\ i\neq j}} \tilde{J}_{ij}\,\vec{\boldsymbol{S}}_i, \tag{2.22}$$

where j can take the values from 0 to $N-1$. In analogy to the Overhauser field in the central spin model (CSM) [10], we denote these fields as local Overhauser fields due to their similar structure. Moreover, we use them to rewrite the effective Hamiltonian

$$\boldsymbol{H}_{\text{eff}} = \frac{1}{2}\sum_j 4\boldsymbol{S}_j^z\boldsymbol{V}_j^z - 2\boldsymbol{S}_j^x\boldsymbol{V}_j^x - 2\boldsymbol{S}_j^y\boldsymbol{V}_j^y. \tag{2.23}$$

The local Overhauser fields clearly differ from each other because the considered spins are randomly distributed on the surface and thus the $\tilde{J}_{ij}$ vary. However, the dipole-dipole interaction is long-range since the interaction strength decreases weakly ($\propto 1/R^3$). Because of this, the number of spins which considerably contribute to the sum in each $\vec{\boldsymbol{V}}_j$ is large allowing for the following approximation: We assume that the local Overhauser fields are equal on average and therefore neglect the local inhomogeneities of the system. Any pair of expectation values which only differ by the local indices of the fields are assumed to be equal, e.g.

$$\langle\vec{\boldsymbol{V}}_i\rangle = \langle\vec{\boldsymbol{V}}_j\rangle \qquad\qquad \forall i,j.$$

Hence, the environment of each spin is equal on average so that we consider the dynamics of a particular spin $\boldsymbol{S}_0$ to be valid for any of the ensemble. The Hamiltonian for this particular spin reads

$$\boldsymbol{H}_{\mathrm{eff},0} = 4\boldsymbol{S}_0^z \boldsymbol{V}^z - 2\boldsymbol{S}_0^x \boldsymbol{V}^x - 2\boldsymbol{S}_0^y \boldsymbol{V}^y, \tag{2.24}$$

where

$$\vec{\boldsymbol{V}} = \sum_{i>0} \tilde{J}_{i0}\, \vec{\boldsymbol{S}}_i \tag{2.25}$$

denotes the corresponding local Overhauser field. We remind the reader that this Hamiltonian in its bare form does not capture the system adequately since interactions between two spins in $\vec{\boldsymbol{V}}$ are omitted. However, when replacing $\vec{\boldsymbol{V}}$ in (2.24) by a classical field as part of S-DMFT those interactions are implicitly considered.

In the following, we justify and employ S-DMFT in three steps:

1. At first, we expound why the local Overhauser field can be substituted by a classical time-dependent field which we call “mean-field”.

2. Subsequently, we reason why this mean-field can be interpeted as a Gaussian random variable with zero average.

3. Finally, the second moments of the Gaussian mean-field are determined.

Since we need to calculate several expectation values during these steps, we require the density operator and thus the temperature of the considered system. The experiments are executed at ambient conditions, $T \approx 300\,\mathrm{K}$ [25], leading to a characteristic thermal energy of roughly

$$E_{\mathrm{th}} = k_{\mathrm{B}} T \approx 26\,\mathrm{meV}. \tag{2.26}$$

By inserting the typical interaction distance (2.17a) into the general dipole-dipole coupling we estimate the energy scale as

$$E_{\mathrm{DD}} \propto J(R_{\mathrm{DD}}) R_{\mathrm{DD}}^2 = \frac{\mu_0 \gamma_{\mathrm{s}}^2}{4\pi R_{\mathrm{DD}}^3} \approx 1.7\,\mathrm{neV}. \tag{2.27}$$

Since this value is about seven orders of magnitude smaller than E_{th} we conclude that the system is disordered. Correspondingly, the density operator is proportional to the identity

$$\boldsymbol{\rho} = \frac{\mathbb{1}}{d}, \tag{2.28}$$

where d is the Hilbert space dimension. In the following subsection we discuss the first S-DMFT step 1.

2.3.2 Substitution by a dynamic mean-field

Our goal is to justify a substitution of the local Overhauser field by a classical time-dependent field. To this end, we show that quantum fluctuations of $\vec{\boldsymbol{V}}$ are subdominant and, furthermore, that back actions of $\vec{\boldsymbol{S}}_0$ are negligible. This is done while comparing our model to the CSM where apparently the semiclassical substitution does not succeed. Let us first introduce the CSM.

The CSM basically describes an interaction between a single central spin $\boldsymbol{S}_0$ with a bath of spins $\boldsymbol{S}_i$ through varying coupling constants J_i, $0 < i \leq N_{\mathrm{CSM}}$. Its Hamiltonian therefore reads [38]

$$\boldsymbol{H}_{\mathrm{CSM}} = \vec{\boldsymbol{S}}_0 \cdot \sum_i J_i \, \vec{\boldsymbol{S}}_i = \vec{\boldsymbol{S}}_0 \cdot \vec{\boldsymbol{P}}, \tag{2.29}$$

where the so-called Overhauser field

$$\vec{\boldsymbol{P}} = \sum_i J_i \, \vec{\boldsymbol{S}}_i \tag{2.30}$$

represents the spin bath. The model is, e.g., used to capture the hyperfine coupling of an electronic spin to a bath of nuclear spins in a quantum dot. For our comparison we focus on a semiclassical approach for the CSM provided in Ref. [38].

First of all, we adapt an analytical argument from Ref. [38] (pp.103-105) supporting the classical-field substitution for both models. To this end, we introduce the Frobenius norm of an operator $\boldsymbol{A}$

$$||\boldsymbol{A}||^2 = \frac{1}{d}\mathrm{Tr}\Big(\boldsymbol{A}^\dagger \boldsymbol{A}\Big). \tag{2.31}$$

One may interpret it as an analogue to the absolut value of a classical vector. Since we are interested in the behavior of the local Overhauser field, we compute the norm of a field component $\boldsymbol{V}^\alpha$ and of the commutator of two components $[\boldsymbol{V}^\alpha, \boldsymbol{V}^\beta]$. Inserting $\boldsymbol{V}^\alpha$ into (2.31) one obtains

$$||\boldsymbol{V}^\alpha||^2 = \frac{1}{d}\sum_{i,j>0} \tilde{J}_{0i}\tilde{J}_{0j}\,\mathrm{Tr}\Big(\boldsymbol{S}_i^\alpha \boldsymbol{S}_j^\alpha\Big) = \frac{1}{d}\sum_{i,j>0} \tilde{J}_{0i}\tilde{J}_{0j}\,\frac{\delta_{ij} d}{4} = \frac{J_{\mathrm{Q}}^2}{4}, \tag{2.32}$$

where we introduced the quadratic dipole-dipole coupling constant

$$J_{\mathrm{Q}}^2 = \sum_{i>0} \tilde{J}_{0i}^2 = \sum_{i>0} \frac{1}{16} J^2\left(R_{0i}\right)\left(R_{0i}^2 - 3R_{z,0i}^2\right)^2. \tag{2.33}$$

Moreover, the norm of the commutator $[\boldsymbol{V}^\alpha, \boldsymbol{V}^\beta]$ obeys

$$\Big|\Big|[\boldsymbol{V}^\alpha, \boldsymbol{V}^\beta]\Big|\Big|^2 = \frac{1}{d}\sum_{i,j>0} \tilde{J}_{0i}^2\tilde{J}_{0j}^2\,\mathrm{Tr}\Big(\boldsymbol{S}_i^\gamma \boldsymbol{S}_j^\gamma\Big) = \frac{1}{d}\sum_{i,j>0} \tilde{J}_{0i}^2\tilde{J}_{0j}^2\,\frac{\delta_{ij} d}{4} \propto \frac{J_{\mathrm{Q}}^4}{4N_{\mathrm{eff}}}, \tag{2.34}$$

where we consider pairwisely different components α, β, γ. Since one of the sums in (2.34) vanishes due to the Kronecker delta, we estimate the expression by adding a factor $1/N_{\text{eff}}$ where N_{eff} denotes the number of spins that considerably contribute to the summation. Note that this number may be smaller than the total number of spins, but nevertheless large due to the long-range interactions. Except for the different coupling constant one obtains the same results for our model as for the central spin model [38]. With the same manner, we argue that the norm of the commutator $[\boldsymbol{V}^\alpha, \boldsymbol{V}^\beta]$ is suppressed relative to the norm of a component $\boldsymbol{V}^\alpha$ according to

$$\left(\left|\left|[\boldsymbol{V}^\alpha, \boldsymbol{V}^\beta]\right|\right|^2\right)^{\frac{1}{2}} \propto \frac{J_{\text{Q}}^2}{2\sqrt{N_{\text{eff}}}} \ll ||\boldsymbol{V}^\alpha||^2 = \frac{J_{\text{Q}}^2}{4}.$$

In contrast, the commutator norm of a quantum mechanical angular momentum operator (small J) is of the same order as the operator norm due to

$$\left(\left|\left|[\boldsymbol{J}^\alpha, \boldsymbol{J}^\beta]\right|\right|^2\right)^{\frac{1}{2}} = \left(||\boldsymbol{J}^\gamma||^2\right)^{\frac{1}{2}} \propto ||\boldsymbol{J}^\gamma||^2$$

for pairwisely different components α, β, γ. Thus, the local Overhauser field $\vec{\boldsymbol{V}}$ behaves like a classical vector and its operator character can be neglected. The same conclusion is drawn in Ref. [38] for the Overhauser field of the CSM. By means of this, the substitution of $\vec{\boldsymbol{V}}$ in our model or $\vec{\boldsymbol{P}}$ in the CSM, respectively, by a static classical field is justified. However, to justify this substitution for a dynamic classical field one also requires that any back actions of $\boldsymbol{S}_0$ are negligible because they are completely neglected throughout the substitution. This issue is treated below, where we discuss a substantial difference between the dipole-dipole model and the CSM leading to a fundamentally different applicability of the semiclassical substitution.

Apart from different couplings and anisotropy, the Hamiltonians (2.24) and (2.29) seem to be similar. However, we have to keep in mind interactions between different spins included in $\vec{\boldsymbol{V}}$, since they are not explicitly appearing in (2.24). In fact, the terms occurring in (2.24) form only a tiny fraction $\propto 1/N$ of the total number of interactions. To comprehend this, one may look at Fig. 2.2a. In addition to the black lines starting at $\vec{\boldsymbol{S}}_0$ the other spins of the ensemble are also connected with one another, illustrated by the orange lines. In contrast, in the CSM there are only connections between the central spin and each nuclear spin, see Fig. 2.2b. We deduce that the compared models have an essentially different geometrical topology leading to an essentially different importance of the central spin. Taking $\vec{\boldsymbol{S}}_0$ out of the dipole-dipole system will hardly affect the dynamics, since the particular spin only contributes marginally and a huge interacting ensemble remains (orange lines in 2.2a). Thereby, the dynamics of $\vec{\boldsymbol{V}}(t)$ can be assumed to be independent on the particular dynamics of $\vec{\boldsymbol{S}}_0(t)$. No back action needs to be taken into account in the model of interacting dipoles. In contrast, omitting $\vec{\boldsymbol{S}}_0$ in the CSM leads to a non-interacting nuclear spin ensemble without any dynamics. Assuming a time-dependent mean-field of which the dynamics is independent of the one of $\vec{\boldsymbol{S}}_0$ is therefore not justified. Correspondingly, the semiclassical substitution is not successful for the CSM, see Ref. [38].

In conclusion, we found an analytical argument supporting to treat $\vec{\boldsymbol{V}}(t)$ as a classical vector by means of the Frobenius norm. Moreover, we discussed why the first step of S-DMFT is well reasoned for our model in contrast to the CSM due to substantial differences between both. Therefore, we continue with step 2.

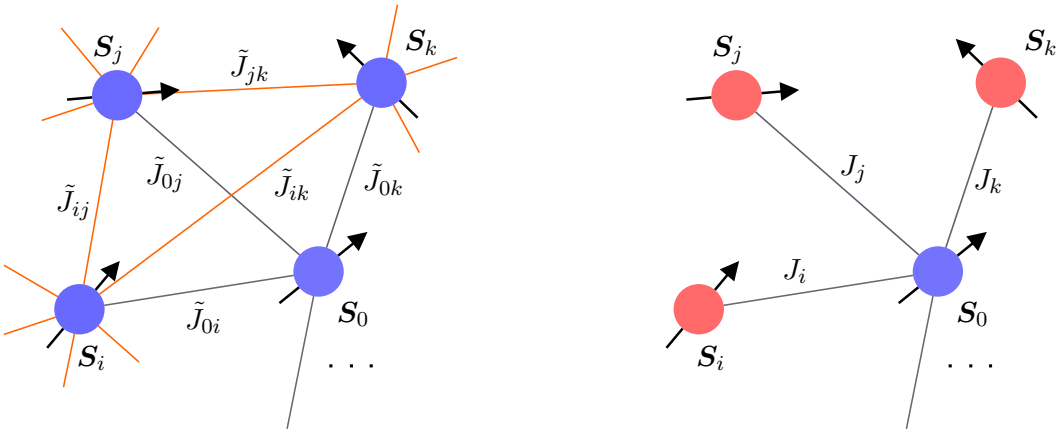

(a) Dipole-dipole model. **(b)** Central spin model.

Figure 2.2: Schematic representation of the interactions in the dipole-dipole model corresponding to (2.24) and in the central spin model corresponding to (2.29).

2.3.3 Properties of the dynamic mean-field

In the last subsection we justified a substitution of $\vec{\boldsymbol{V}}$ by a time-dependent mean-field $\vec{V}(t)$. The corresponding semiclassical Hamiltonian reads

$$\boldsymbol{H}_{\mathrm{mf}}(t) = 4\boldsymbol{S}_0^z V^z(t) - 2\boldsymbol{S}_0^x V^x(t) - 2\boldsymbol{S}_0^y V^y(t). \tag{2.35}$$

It is a key aspect of the approach that the fundamental properties of the mean-field result from expectation values of the local Overhauser field due to the substitution. For a single component we find

$$\langle \boldsymbol{V}^\alpha(t)\rangle_{\mathrm{qm}} = \sum_{i>0} \tilde{J}_{0i} \langle \boldsymbol{S}_i^\alpha(t)\rangle_{\mathrm{qm}}, \tag{2.36}$$

where the index qm implies that the corresponding time evolution refers to the Hamiltonian (2.20). Inserting the density operator (2.28) into the single spin expectation value one obtains

$$\langle \boldsymbol{S}_i^\alpha(t)\rangle_{\mathrm{qm}} = \langle \boldsymbol{S}_i^\alpha(0)\rangle_{\mathrm{qm}} = \frac{1}{d}\mathrm{Tr}\left(\boldsymbol{S}_i^\alpha\right) = 0 \tag{2.37}$$

and thus

$$\langle \boldsymbol{V}^\alpha(t)\rangle_{\mathrm{qm}} = 0. \tag{2.38}$$

It is obvious that a common mean-field approach where $\vec{\boldsymbol{V}}$ is replaced by its expectation value is trivial in our case. The Hamiltonian would simply vanish because we assume thermal disorder. In fact, we want to study the dynamics of the spin system and not its static magnetization. Therefore, we interpret the mean-field as a dynamic random variable and average over different configurations to compute any expectation values of the system. Correspondingly, we require the distribution function of $\vec{V}(t)$. Since the properties of the mean-field follow from that of the local Overhauser field, we equate any classical averages of $\vec{V}(t)$ to the corresponding quantum mechanical expectation values of $\vec{\boldsymbol{V}}(t)$. This scheme is illustrated in Fig. 2.3. In what follows, we justify that the dynamic mean-field resulting from $\vec{\boldsymbol{V}}(t)$ follows a Gaussian distribution due to the central limit theorem [39].

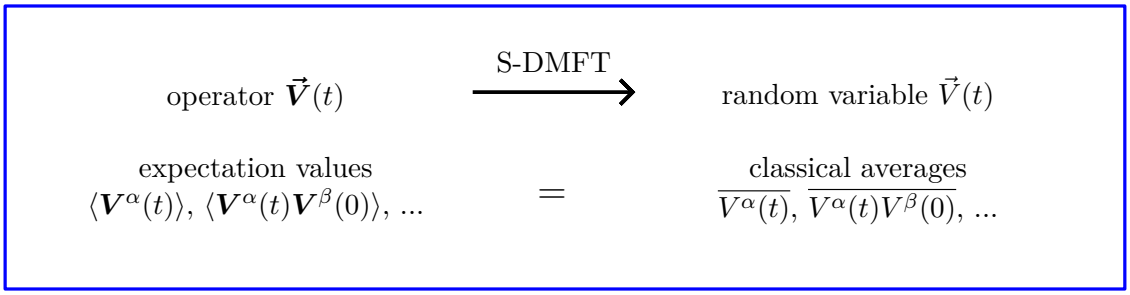

Figure 2.3: Scheme of the random-field substitution in S-DMFT.

To this end, we have to clarify that on the one hand, $\vec{\boldsymbol{V}}(t)$ sums over a large number of variables and on the other hand, these variables are uncorrelated to each other. The first condition is clearly satisfied because the local Overhauser field (2.25) sums over a large number of spin operators. To justify the second statement, however, we have to demand that any pair correlations between two sites vanish which is not obvious. In the following, we discuss this issue while distinguishing between one-time pair correlations a) and two-time pair correlations b).

a) For the first sort we find

$$\langle \boldsymbol{S}_i^\alpha(t)\boldsymbol{S}_j^\beta(t)\rangle = \langle \boldsymbol{S}_i^\alpha(0)\boldsymbol{S}_j^\beta(0)\rangle = \frac{1}{d}\mathrm{Tr}\left(\boldsymbol{S}_i^\alpha \boldsymbol{S}_j^\beta\right) = 0, \tag{2.39}$$

because the time evolution operator commutes with the density operator and $i \neq j$. Hence, they do not violate the second condition for the central limit theorem.

b) The two-time pair correlations $\langle \boldsymbol{S}_i^\alpha(t_1)\boldsymbol{S}_j^\beta(t_2)\rangle$, where $i \neq j$, are generally not zero. From this point, though, we assume them to be subdominant and therefore neglect them against the autocorrelations. An analytical argument for this assumption is furnished in App. A. There, we introduce a Bethe lattice consisting of spins with a nearest-neighbor interaction. We are able to show that pair correlations are suppressed for increasing number of nearest neighbors. By means of this, we conclude that the central limit theorem is approximately applicable.

Summarizingly, the dynamic mean-field behaves Gaussian so that we only need the first two moments to capture it completely. The average value is already determined through

$$\overline{\vec{V}(t)} = \langle \vec{\boldsymbol{V}}(t) \rangle_{\mathrm{qm}} = 0. \tag{2.40}$$

In the next subsection we compute the second moments as part of step 3.

2.3.4 Self-consistency problem for the mean-field autocorrelations

We established that the dynamic mean-field is Gaussian, since it consists of a large number of weakly correlated variables. To quantify this behavior, we relate the mean-field autocorrelations to the autocorrelations of the local Overhauser field via

$$\begin{aligned} \overline{V^\alpha(t)V^\beta(0)} = \langle \boldsymbol{V}^\alpha(t)\boldsymbol{V}^\beta(0)\rangle_{\mathrm{qm}} &= \sum_{i,j>0} \tilde{J}_{0i}\tilde{J}_{0j}\, \langle \boldsymbol{S}_i^\alpha(t)\boldsymbol{S}_j^\beta(0)\rangle_{\mathrm{qm}} \\ &= \sum_{i>0} \tilde{J}_{0i}^2 \langle \boldsymbol{S}_i^\alpha(t)\boldsymbol{S}_i^\beta(0)\rangle_{\mathrm{qm}} + 2\sum_{0<i<j} \tilde{J}_{0i}\tilde{J}_{0j}\, \langle \boldsymbol{S}_i^\alpha(t)\boldsymbol{S}_j^\beta(0)\rangle_{\mathrm{qm}}. \end{aligned} \tag{2.41}$$

The first term sums the autocorrelations for each spin interacting with $\boldsymbol{S}_0$. Since an equal behavior of all spins is assumed on average, we are allowed to take the autocorrelations out of the sum and omit the site index i. The second term contains all time-dependent pair correlations except the ones with $\boldsymbol{S}_0$. As explained in b) we neglect these contributions, since we assume them to be subdominant. We refer to App. A for an analytical argument. In conclusion, the mean-field autocorrelation obeys

$$\overline{V^\alpha(t)V^\beta(0)} = J_{\mathrm{Q}}^2 \langle \boldsymbol{S}^\alpha(t)\boldsymbol{S}^\beta(0)\rangle_{\mathrm{qm}} = J_{\mathrm{Q}}^2 \langle \boldsymbol{S}^\alpha(t)\boldsymbol{S}^\beta(0)\rangle_{\mathrm{mf}}, \tag{2.42}$$

where J_{Q}^2 is the quadratic coupling constant, see (2.2). In line with our approach we replaced the expectation value corresponding to (2.20) by a mean-field expectation value. The latter is computed while calculating an expectation value with regard to the mean-field Hamiltonian (2.35) multiple times for different configurations of the mean-field, i.e. different temporal trends $\vec{V}(0 \to t)$. We denote the expectation values corresponding to a single configuration simply by

$$\langle \boldsymbol{S}^\alpha(t)\boldsymbol{S}^\beta(0)\rangle := \langle \boldsymbol{S}^\alpha(t)\boldsymbol{S}^\beta(0)\rangle \left(\vec{V}(0 \to t)\right). \tag{2.43}$$

Subsequently, one averages over the single-configuration results according to

$$\langle \boldsymbol{S}^\alpha(t)\boldsymbol{S}^\beta(0)\rangle_{\mathrm{mf}} = \overline{\langle \boldsymbol{S}^\alpha(t)\boldsymbol{S}^\beta(0)\rangle}, \tag{2.44}$$

where the line on the right-hand-side refers to an average over different configurations $\vec{V}(0 \to t)$. Those are sampled based on a Gaussian distribution which is determined through the autocorrelations of the mean-field (2.42). We refer to 3.2 for details about the sampling procedure.

By (2.42) the mean-field autocorrelations are connected to the single-spin autocorrelations. Since the computation of the second sort requires the first sort and vice versa, we call

equation (2.42) a self-consistency condition. Indeed, this is common for mean-field approaches due to the substitution of operators by quantities which depend on the expectation values of the operators. Basically, to solve the self-consistency problem numerically one selects initial functions for the mean-field autocorrelations, determines the single-spin autocorrelations via sampling and computes new mean-field autocorrelations with aid of (2.42) as part of the first iteration step $(0) \to (1)$. With the same manner one iterates from an arbitrary step $(n) \to (n+1)$ to optimize the results. The procedure is stopped when an adequate convergence is achieved. Since there are three spin components $\alpha, \beta \in \{x, y, z\}$, we have to consider nine autocorrelations at maximum. However, by exploiting symmetries of the system we reduce this number considerably in the following subsection.

2.3.5 Simplification of the self-consistency problem by symmetries

Generally, for the symmetry discussion we consider the full q.m. Hamiltonian (2.20) in the rotating frame without mean-field approximation. The first thing we realize is that all autocorrelations are invariant to shifts in time because of

$$\langle \boldsymbol{S}^{\alpha}(t_1)\boldsymbol{S}^{\beta}(t_2)\rangle = \langle \boldsymbol{U}^{\dagger}(t_1)\boldsymbol{S}^{\alpha}(0)\boldsymbol{U}(t_1)\boldsymbol{U}^{\dagger}(t_2)\boldsymbol{S}^{\beta}(0)\boldsymbol{U}(t_2)\rangle \tag{2.45a}$$

$$= \langle \boldsymbol{U}^{\dagger}(t_1 - t_2)\boldsymbol{S}^{\alpha}(0)\boldsymbol{U}(t_1 - t_2)\boldsymbol{S}^{\beta}(0)\rangle \tag{2.45b}$$

$$= \langle \boldsymbol{S}^{\alpha}(t_1 - t_2)\boldsymbol{S}^{\beta}(0)\rangle, \tag{2.45c}$$

where we used the group property of the time evolution operator and the fact that any operator commutes with the density operator since the latter is proportional to unity. Secondly, we study the behavior of the autocorrelation functions under time reversal. To this end, we introduce the antiunitary time reversal operator [40]

$$\Theta = -\left(\Theta^{\dagger}\right)^{-1} \tag{2.46}$$

acting on quantum mechanical states as

$$\Theta\,|\Psi(t)\rangle = |\Psi(-t)\rangle\,. \tag{2.47}$$

Spin operators or general angular momentum operators transform as

$$\Theta \boldsymbol{S}^{\alpha}\Theta^{-1} = -\boldsymbol{S}^{\alpha} \tag{2.48}$$

due to their fundamental commutator relations. Since the Hamiltonian is bilinear in spin operators, it commutes with Θ. Thus, the time evolution operator is transformed according to

$$\Theta \boldsymbol{U}(t)\Theta^{-1} = \boldsymbol{U}(-t). \tag{2.49}$$

Note that this does not hold anymore when an external field is applied to the system. Using (2.48) and (2.49) we find

$$\langle \boldsymbol{S}^{\alpha}(t)\boldsymbol{S}^{\beta}(0)\rangle = \langle \Theta^{-1}\underbrace{\Theta \boldsymbol{U}^{\dagger}(t)\Theta^{-1}}_{\boldsymbol{U}^{\dagger}(-t)}\underbrace{\Theta \boldsymbol{S}^{\alpha}(0)\Theta^{-1}}_{-\boldsymbol{S}^{\alpha}(0)}\underbrace{\Theta \boldsymbol{U}(t)\Theta^{-1}}_{\boldsymbol{U}(-t)}\underbrace{\Theta \boldsymbol{S}^{\beta}(0)}_{-\boldsymbol{S}^{\beta}(0)\Theta}\rangle \tag{2.50a}$$

$$= \langle \Theta^{-1}\boldsymbol{S}^{\alpha}(-t)\boldsymbol{S}^{\beta}(0)\Theta\rangle \tag{2.50b}$$

$$= \langle \boldsymbol{S}^{\alpha}(-t)\boldsymbol{S}^{\beta}(0)\rangle \tag{2.50c}$$

and thus time-reversal symmetry for all autocorrelations. Furthermore, we notice that the Hamiltonian (2.20) is isotropic with respect to the x- and y-components of the spins. Applying a spin rotation of $\pi/2$ around the z-axis results in

$$\boldsymbol{S}^{x} \longrightarrow +\boldsymbol{S}^{y}, \qquad \boldsymbol{S}^{y} \longrightarrow -\boldsymbol{S}^{x}, \tag{2.51}$$

which does not affect $\boldsymbol{H}_{\text{eff}}$ since the crucial terms do not change

$$\boldsymbol{S}_i^{x}\boldsymbol{S}_j^{x} + \boldsymbol{S}_i^{y}\boldsymbol{S}_j^{y} \longrightarrow \boldsymbol{S}_i^{y}\boldsymbol{S}_j^{y} + \boldsymbol{S}_i^{x}\boldsymbol{S}_j^{x}. \tag{2.52}$$

In summary, we found three important symmetries of the system, namely time translation invariance (TTI), time reversal symmetry (TRS) and $\pi/2$-spin-rotational symmetry around z (SRZ). Combining them we obtain

$$\langle \boldsymbol{S}^{x}(t)\boldsymbol{S}^{y}(0)\rangle \overset{\text{SRZ}}{=} -\langle \boldsymbol{S}^{y}(t)\boldsymbol{S}^{x}(0)\rangle \overset{\text{TRS}}{=} -\langle \boldsymbol{S}^{y}(-t)\boldsymbol{S}^{x}(0)\rangle \tag{2.53a}$$

$$\overset{\text{TTI}}{=} -\langle \boldsymbol{S}^{y}(0)\boldsymbol{S}^{x}(t)\rangle = -\langle \boldsymbol{S}^{x}(t)\boldsymbol{S}^{y}(0)\rangle, \tag{2.53b}$$

and hence

$$\langle \boldsymbol{S}^{x}(t)\boldsymbol{S}^{y}(0)\rangle = \langle \boldsymbol{S}^{y}(t)\boldsymbol{S}^{x}(0)\rangle = 0. \tag{2.54}$$

Moreover, one finds

$$\langle \boldsymbol{S}^{x}(t)\boldsymbol{S}^{z}(0)\rangle \overset{\text{SRZ}}{=} \langle \boldsymbol{S}^{y}(t)\boldsymbol{S}^{z}(0)\rangle \overset{\text{SRZ}}{=} -\langle \boldsymbol{S}^{x}(t)\boldsymbol{S}^{z}(0)\rangle, \tag{2.55a}$$

$$\langle \boldsymbol{S}^{z}(t)\boldsymbol{S}^{x}(0)\rangle \overset{\text{SRZ}}{=} \langle \boldsymbol{S}^{z}(t)\boldsymbol{S}^{y}(0)\rangle \overset{\text{SRZ}}{=} -\langle \boldsymbol{S}^{z}(t)\boldsymbol{S}^{x}(0)\rangle, \tag{2.55b}$$

and by this,

$$\langle \boldsymbol{S}^{x}(t)\boldsymbol{S}^{z}(0)\rangle = \langle \boldsymbol{S}^{y}(t)\boldsymbol{S}^{z}(0)\rangle = \langle \boldsymbol{S}^{z}(t)\boldsymbol{S}^{x}(0)\rangle = \langle \boldsymbol{S}^{z}(t)\boldsymbol{S}^{y}(0)\rangle = 0. \tag{2.56}$$

Furthermore, the rotational symmetry implies the eqivalence of two of the three remaining functions

$$\langle \boldsymbol{S}^{x}(t)\boldsymbol{S}^{x}(0)\rangle \overset{\text{SRZ}}{=} \langle \boldsymbol{S}^{y}(t)\boldsymbol{S}^{y}(0)\rangle. \tag{2.57}$$

Since the mean-field autocorrelations are given by the single-spin autocorrelations according to (2.42), clearly the symmetry relations hold for them as well. The resulting self-consistency problem reads

$$v^{xx}(t) = v^{yy}(t) = J_{\text{Q}}^{2}\, g^{xx}(t), \tag{2.58a}$$

$$v^{zz}(t) = J_{\text{Q}}^{2}\, g^{zz}(t), \tag{2.58b}$$

where we denoted

$$g^{\alpha\beta} = \langle \boldsymbol{S}^{\alpha}(t)\boldsymbol{S}^{\beta}(0)\rangle_{\mathrm{qm}} = \langle \boldsymbol{S}^{\alpha}(t)\boldsymbol{S}^{\beta}(0)\rangle_{\mathrm{mf}}, \tag{2.59a}$$

$$v^{\alpha\beta} = \overline{V^{\alpha}(t)V^{\beta}(0)}. \tag{2.59b}$$

Below we will extend the system and thus the self-consistency condition to magnetic field noise to capture the experimental setup.

2.4 Extension to a local magnetic noise

As mentioned in the introduction, there is a local magnetic noise resulting from proton spins near the surface [25]. For simplicity, we assume this noise to be Gaussian. This assumption is justified by the central limit theorem because the magnetic field at each surface spin consists of many rather independent contributions. Since the electronic Larmor frequency is in general considerably larger than that of the protons due to

$$\gamma_{\mathrm{s}} = 2\mu_{\mathrm{B}} \gg \gamma_{\mathrm{p}} \approx 0.003\mu_{\mathrm{B}}, \tag{2.60}$$

we assume the noise to be approximately static at timescales of the electronic spin dynamics. To consider this noise in our theoretical approach we include the additional term

$$\boldsymbol{H}_{\mathrm{N}} = \gamma_{\mathrm{s}} \sum_i \vec{b}_i \cdot \vec{\boldsymbol{S}}_i \tag{2.61}$$

in the fundamental Hamiltonian (2.5), where $\vec{b}_i$ represents the static noise vector varying in space. Note that $\vec{b}_i$ is not considered to be an operator but a real vector because we do not consider back actions of the surface spins on the noise. Indeed, we interpret it as a random variable so that we basically have to average over multiple configurations $\{\vec{b}_i\}$. By turning to the Larmor rotating frame and applying a RWA the x- and y-components of the noise vanish. This is the case because they acquire oscillating prefactors $\sin(\omega_{\mathrm{L}}t)$ and $\cos(\omega_{\mathrm{L}}t)$ in the rotating frame which are zero on average. We stress that we do not consider a precession of the noise itself, since the protonic Larmor frequency is considerably small. In line with Sec. 2.2, the effective Hamiltonian reads

$$\boldsymbol{H}_{\mathrm{eff,N}} = \boldsymbol{H}_{\mathrm{eff}} + \gamma_{\mathrm{s}} \sum_i b_i^z \boldsymbol{S}_i^z. \tag{2.62}$$

Corresponding expectation values are averaged over different noise configurations according to

$$\begin{aligned}\langle \boldsymbol{A}(t_1,t_2,...)\rangle_{\mathrm{qm,N}} = \left(\prod_{i=0}^{N-1}\int_{-\infty}^{\infty} \mathrm{d}b_i^z \left(\sqrt{2\pi}\,\overline{b^2}^{\mathrm{N}}\right) \mathrm{e}^{-\left(b_i^z\right)^2\left(2\overline{b^2}^{\mathrm{N}}\right)^{-1}}\right) \\ \cdot \langle \boldsymbol{A}(t_1,t_2,...)\rangle_{\mathrm{qm}}\left(\{b_i^z\}\right),\end{aligned} \tag{2.63}$$

where $\overline{b^2}^{\mathrm{N}} := \overline{\left(b_i^z\right)^2}^{\mathrm{N}}, \forall i$, denotes the variance of the noise and the expectation value in the integral refers to a single noise configuration $\{b_i^z\}$. One may realize that due to the

magnetic noise the Hamiltonian (2.62) is not time-reversal invariant anymore. Applying time reversal to it induces a sign in front of the noise sum. However, since the expectation values are determined through noise averaging (2.63), this sign can simply be eliminated by substitution. Correspondingly, the physical results are time-reversal invariant and any symmetries observed in 2.3.5 hold for the extended system as well. Thus, we still only require $g^{\alpha\alpha}(t)$ and $v^{\alpha\alpha}(t)$ for $\alpha \in \{x, z\}$ in the following.

For the dynamic mean-field approach we include the magnetic noise in the z-component of the local Overhauser fields as

$$\boldsymbol{V}^z_{\mathrm{N},j} = \gamma_\mathrm{s} b^z_j + \boldsymbol{V}^z_j = \gamma_\mathrm{s} b^z_j + \sum_{\substack{i \\ i \neq j}} \tilde{J}_{ij}\, \boldsymbol{S}^z_i. \tag{2.64}$$

Then, the Hamiltonian for a particular spin reads

$$\boldsymbol{H}_{\mathrm{eff,N},0} = 4\boldsymbol{S}^z_0 \boldsymbol{V}^z_\mathrm{N} - 2\boldsymbol{S}^x_0 \boldsymbol{V}^x - 2\boldsymbol{S}^y_0 \boldsymbol{V}^y. \tag{2.65}$$

We emphasize that by this definition the expectation values of $\boldsymbol{V}^z_{\mathrm{N},j}$ are still independent of j when neglecting local inhomogenities since the noise is averaged out. Moreover, the three steps in 2.3 to justify the dynamic mean-field approach are still valid, because the included noise is assumed to be Gaussian with zero average. Thus, it conserves the fundamental behavior of the mean-field. The self-consistency condition for the longitudinal autocorrelation needs to be recalculated, though. We obtain

$$\overline{V^z_\mathrm{N}(t) V^z_\mathrm{N}(0)} = \overline{V^z(t) V^z(0)} + \frac{1}{4}\gamma_\mathrm{s} \overline{b}^\mathrm{N} \left(\overline{V^z(t)} + \overline{V^z(0)} \right) + \frac{1}{16}\gamma_\mathrm{s}^2 \overline{b^2}^\mathrm{N} \tag{2.66a}$$

$$= \overline{V^z(t) V^z(0)} + \frac{1}{16}\gamma_\mathrm{s}^2 \overline{b^2}^\mathrm{N}, \tag{2.66b}$$

where the index N denotes a pure noise averaging. Therefore, the mean-field Hamiltonian reduces to

$$\boldsymbol{H}_{\mathrm{mf,N}}(t) = 4V^z_\mathrm{N}(t)\boldsymbol{S}^z_0 - 2V^x(t)\boldsymbol{S}^x_0 - 2V^y(t)\boldsymbol{S}^y_0, \tag{2.67}$$

which is equal to (2.35) apart from the adjusted second moment of the mean-field z-component. Eventually, the self-consistency problem reads

$$v^{xx}(t) = v^{yy}(t) = J_\mathrm{Q}^2\, g^{xx}(t), \tag{2.68a}$$

$$v^{zz}(t) = J_\mathrm{Q}^2 \left(g^{zz}(t) + C \right), \tag{2.68b}$$

where we introduced the unitless constant

$$C = \frac{1}{J_\mathrm{Q}^2} \frac{1}{16} \gamma_s^2 \overline{b^2}^\mathrm{N}, \tag{2.69}$$

and set $v^{zz}(t) := \overline{V^z_\mathrm{N}(t) V^z_\mathrm{N}(0)}$. In conclusion, the numerical implementation is not hampered by the magnetic noise because we only have to consider a constant offset in $v^{zz}(t)$. However, by C we have to consider another phenomenological parameter which influences the results.

In the following, we furnish an approximate analytical expression for the autocorrelation functions in the case of large C.

We completely neglect the time-dependent terms in (2.65) relative to the strongly fluctuating magnetic noise b so that

$$\boldsymbol{H}_{\mathrm{eff,N},0} \approx \gamma_{\mathrm{s}} b \boldsymbol{S}_0^z. \tag{2.70}$$

Since this expression is time-independent, one simply calculates the single-spin autocorrelations with aid of the time evolution operator given by

$$\boldsymbol{U}(t,0) = \mathrm{e}^{-\mathtt{i}\gamma_{\mathrm{s}} b t\, \boldsymbol{S}_0^z}. \tag{2.71}$$

Inserting this we find

$$g^{xx}(t) = \overline{\langle \boldsymbol{S}_0^x(t)\boldsymbol{S}_0^x(0)\rangle}^{\mathrm{N}} = \frac{1}{2}\overline{\mathrm{Tr}\Big(\Big[\boldsymbol{S}^x\cos(\gamma_{\mathrm{s}}bt) - \boldsymbol{S}^y\sin(\gamma_{\mathrm{s}}bt)\Big]\boldsymbol{S}^x\Big)}^{\mathrm{N}} = \frac{1}{4}\overline{\cos(\gamma_{\mathrm{s}}bt)}^{\mathrm{N}}. \tag{2.72a}$$

To carry out the averaging, we use the assumed Gaussian noise distribution

$$p_{\mathrm{N}}(b) = \left(2\pi\overline{b^2}^{\mathrm{N}}\right)^{-\frac{1}{2}} \mathrm{e}^{-b^2\left(2\overline{b^2}^{\mathrm{N}}\right)^{-1}}, \tag{2.73}$$

Then, the autocorrelation fulfills

$$g^{xx}(t) = \frac{1}{4}\int_{-\infty}^{\infty}\left(2\pi\overline{b^2}^{\mathrm{N}}\right)^{-\frac{1}{2}} \mathrm{e}^{-b^2\left(2\overline{b^2}^{\mathrm{N}}\right)^{-1}}\cos\left(\gamma_{\mathrm{s}}bt\right)\mathrm{d}b \tag{2.74a}$$

$$= \frac{1}{4}\left(2\pi\overline{b^2}^{\mathrm{N}}\gamma_{\mathrm{s}}^2\right)^{-\frac{1}{2}}\int_{-\infty}^{\infty}\mathrm{e}^{-\omega^2\left(2\gamma_{\mathrm{s}}^2\overline{b^2}^{\mathrm{N}}\right)^{-1}}\mathrm{e}^{\mathtt{i}\omega t}\mathrm{d}\omega \tag{2.74b}$$

$$= \frac{1}{4}\mathrm{e}^{-8CJ_{\mathrm{Q}}^2t^2}. \tag{2.74c}$$

Furthermore, we find

$$g^{zz}(t) = \overline{\langle \boldsymbol{S}_0^z(t)\boldsymbol{S}_0^z(0)\rangle}^{N} = \frac{1}{2}\overline{\mathrm{Tr}\left(\boldsymbol{S}^z\boldsymbol{S}^z\right)}^{\mathrm{N}} = \frac{1}{4}. \tag{2.75}$$

Clearly, even for very large C we do not expect a static $g^{zz}(t)$ because the time-dependent mean-field contributions are non-zero leading to decoherence at some time. Though, we expect its decay to slow down when the noise strength is raised. Moreover, through (2.74c) we predict a Gaussian behavior of $g^{xx}(t)$ for large C.

In chapter 3 we present an algorithm to solve the self-consistency problem through iteration. In the next section we estimate J_{Q}^2 by means of a continuum limit.

2.5 Quadratic coupling constant

We remind the reader of the quadratic coupling

$$J_{\mathrm{Q}}^2 = \sum_{i>0} \tilde{J}_{0i}^2 = \sum_{i>0} \frac{1}{16} J^2\left(R_{0i}\right)\left(R_{0i}^2 - 3R_{z,0i}^2\right)^2 . \tag{2.76}$$

The z-component of the distance vector clearly depends on the alignment of the magnetic field $\vec{B}$, since the z-axis is per definition parallel to $\vec{B}$. Before considering the continuum limit, we express $R_{z,0i}$ by polar coordinates (R, φ) on the surface, see 2.4.

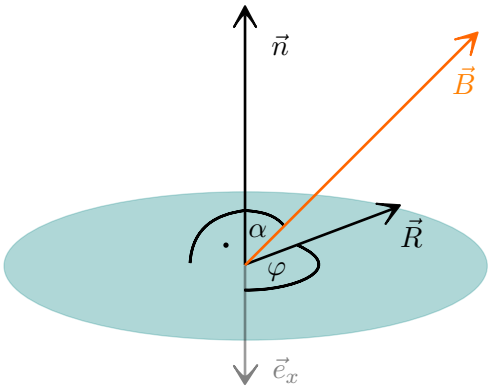

Figure 2.4: Schematic plot of polar coordinates on the considered planar surface. The x-axis is choosen perpendicular to $\vec{B}$ and $\vec{n}$ without loss of generality.

The polar angle results from

$$\vec{R}_{0i} \cdot \vec{e}_x = R_{x,0i} = R\cos\varphi, \tag{2.77}$$

while the normal vector of the surface plane is given by

$$\vec{n} = \begin{pmatrix} 0 \\ -\sin(\alpha) \\ \cos(\alpha) \end{pmatrix} . \tag{2.78}$$

By means of this, we obtain

$$\vec{n} \cdot \vec{R}_{0i} = -R_{y,i0}\sin(\alpha) + R_{z,i0}\cos(\alpha) \tag{2.79a}$$

$$= -\sqrt{R^2\sin^2\varphi - R_{z,i0}^2}\sin(\alpha) + R_{z,i0}\cos(\alpha) \stackrel{!}{=} 0 \tag{2.79b}$$

Solving for $R_{z,i0}$ leads to

$$R_{z,i0} = R\sin(\alpha)\sin(\varphi), \tag{2.80}$$

and eventually

$$J_{\mathrm{Q}}^2 = \sum_{i>0} \frac{1}{16} J^2\left(R_{0i}\right) R_{0i}^4 \left(1 - 3\sin^2(\alpha)\sin^2(\varphi_{i0})\right)^2 . \tag{2.81}$$

Now, we replace the sum by a two-dimensional integral over the surface according to

$$J_{\mathrm{Q}}^2 \approx 2\pi I(\alpha) n_0 \int_{r_{\min}}^{\infty} \mathrm{d}R \, \frac{1}{16} J^2(R) R^5, \tag{2.82a}$$

$$I(\alpha) = \frac{1}{2\pi} \int_0^{2\pi} \mathrm{d}\varphi \left(1 - 3\sin^2(\alpha)\sin^2(\varphi)\right)^2, \tag{2.82b}$$

where n_0 is the spin density and $r_{\min}$ stands for the average distance between two neighbor spins. Since the considered system is two-dimensional, these quantities are related through

$$n_0 = \frac{1}{r_{\min}^2}. \tag{2.83}$$

For the φ-integration we find

$$I(\alpha) = \left(\frac{27}{8}\sin^4(\alpha) - 3\sin^2(\alpha) + 1\right), \tag{2.84}$$

while the r-integral yields

$$n_0 \int_{r_{\min}}^{\infty} \mathrm{d}R \, \frac{1}{16} J^2(R) R^5 = \frac{n_0 \mu_0^2 \gamma_{\mathrm{s}}^4}{(16\pi)^2} \int_{r_{\min}}^{\infty} \mathrm{d}R \, \frac{1}{R^5} = \frac{\mu_0^2 \gamma_{\mathrm{s}}^4}{(16\pi)^2} \frac{1}{4 r_{\min}^6}, \tag{2.85}$$

leading to

$$J_{\mathrm{Q}}(\alpha) = \sqrt{2\pi I(\alpha)} \frac{\mu_0 \mu_{\mathrm{B}}^2}{8\pi} \frac{1}{r_{\min}^3}. \tag{2.86}$$

We plotted $\sqrt{I(\alpha)}$ vs. α in Fig. 2.5. At the magic angle

$$\alpha_{\mathrm{mag}} = \arcsin\sqrt{\frac{2}{3}} \approx 0.304\pi, \tag{2.87}$$

where the autocorrelations are measured in experiment [25], the angular function yields

$$\sqrt{I(\alpha_{\mathrm{mag}})} = \frac{1}{\sqrt{2}}. \tag{2.88}$$

In the following section we will consider the surface-spin system in the zero-field limit.

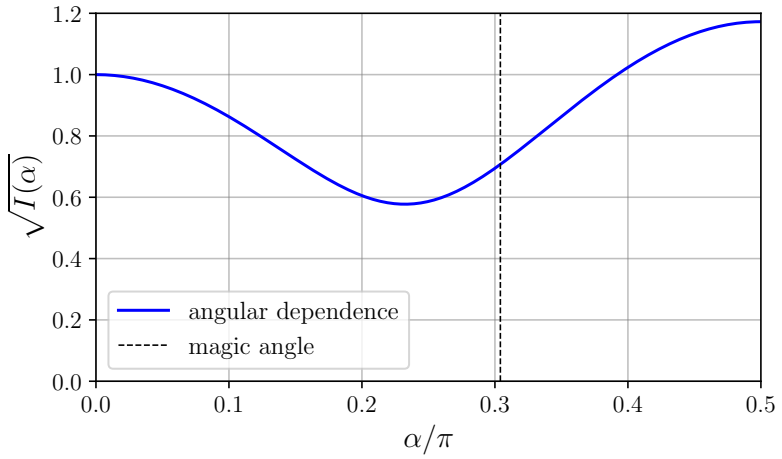

Figure 2.5: Plot of the angular dependence of $\sqrt{I(\alpha)}$.

2.6 Zero-field limit

To the end of this chapter, we deal with a dipolar surface-spin system subjected to a local static magnetic noise. In contrast to the previously considered system, we do not consider any static fields and thus stay in the resting reference frame. Any other properties of the previous system, such as ambient conditions, are taken over. Correspondingly, the fundamental Hamiltonian reads

$$\boldsymbol{H}_{\mathrm{ZF}} = \boldsymbol{H}_{\mathrm{DD}} + \boldsymbol{H}_{\mathrm{N}} \tag{2.89a}$$

$$= \sum_{i<j} J\left(R_{ij}\right) \left(R_{ij}^2 \left(\vec{\boldsymbol{S}}_i \cdot \vec{\boldsymbol{S}}_j\right) - 3 \left(\vec{\boldsymbol{S}}_i \cdot \vec{R}_{ij}\right) \left(\vec{\boldsymbol{S}}_j \cdot \vec{R}_{ij}\right) \right) + \gamma_{\mathrm{s}} \sum_i \vec{b}_i \cdot \vec{\boldsymbol{S}}_i. \tag{2.89b}$$

Again, the noise shall be Gaussian with zero average and for simplicity, we assume it to be isotropic and on average equal at each site

$$\overline{\left(b_i^\alpha\right)^2}^{\mathrm{N}} =: \overline{b^2}^{\mathrm{N}}, \qquad \forall \alpha, i. \tag{2.90}$$

Moreover, any of its autocorrelations shall vanish

$$\overline{b^\alpha b^\beta}^{\mathrm{N}} = 0, \qquad \forall \alpha \neq \beta. \tag{2.91}$$

This restriction is supported by the fact that the noise results from disordered proton spins with dynamics at considerably larger timescales than the electronic dynamics. According to these assumptions, any physical expectation values of the system are determined

through

$$\langle \boldsymbol{A}(t_1,t_2,...)\rangle_{\mathrm{N}} = \left(\prod_{\alpha}\prod_{i=0}^{N-1}\int_{-\infty}^{\infty}\mathrm{d}b_i^{\alpha}\left(\sqrt{2\pi}\,\overline{b^2}^{\mathrm{N}}\right)^{-1}\mathrm{e}^{-\left(b_i^{\alpha}\right)^2\left(2\overline{b^2}^{\mathrm{N}}\right)^{-1}}\right) \cdot \langle \boldsymbol{A}(t_1,t_2,...)\rangle\left(\{\vec{b}_i\}\right), \tag{2.92}$$

where the expectation value in the integral is computed from the Hamiltonian (2.89) with the inserted noise configuration $\{\vec{b}_i\}$.

Since we do not consider an external field, we simply set the z-axis perpendicular to the surface so that the distance vectors read

$$\vec{R}_{ij} = \begin{pmatrix} R_{x,ij} \\ R_{y,ij} \\ 0 \end{pmatrix} = R_{ij}\begin{pmatrix} \cos(\varphi_{ij}) \\ \sin(\varphi_{ij}) \\ 0 \end{pmatrix}. \tag{2.93}$$

By means of this, the Hamiltonian simplifies to

$$\begin{aligned}\boldsymbol{H}_{\mathrm{ZF}} = \boldsymbol{H}_{\mathrm{N}} + \sum_{i>j} R_{ij}^2 J(R_{ij})\Big(&\boldsymbol{S}_i^z\boldsymbol{S}_j^z + \left(1-3\cos^2(\varphi_{ij})\right)\boldsymbol{S}_i^x\boldsymbol{S}_j^x \\ &+ \left(1-3\sin^2(\varphi_{ij})\right)\boldsymbol{S}_i^y\boldsymbol{S}_j^y - 3\sin(\varphi_{ij})\cos(\varphi_{ij})\left(\boldsymbol{S}_i^x\boldsymbol{S}_j^y + \boldsymbol{S}_i^y\boldsymbol{S}_j^x\right)\Big).\end{aligned} \tag{2.94}$$

In order to apply S-DMFT, we introduce local Overhauser fields $\vec{\boldsymbol{V}}_j$ each representing the environment of a single spin $\vec{\boldsymbol{S}}_j$. From the Hamiltonian (2.94), their components read

$$\boldsymbol{V}_j^x = \sum_{i\neq j} R_{ij}^2 J(R_{ij})\Big(\left(1-3\cos^2(\varphi_{ij})\right)\boldsymbol{S}_i^x - 3\cos(\varphi_{ij})\sin(\varphi_{ij})\boldsymbol{S}_i^y\Big), \tag{2.95a}$$

$$\boldsymbol{V}_j^y = \sum_{i\neq j} R_{ij}^2 J(R_{ij})\Big(\left(1-3\sin^2(\varphi_{ij})\right)\boldsymbol{S}_i^y - 3\cos(\varphi_{ij})\sin(\varphi_{ij})\boldsymbol{S}_i^x\Big), \tag{2.95b}$$

$$\boldsymbol{V}_j^z = \sum_{i\neq j} R_{ij}^2 J(R_{ij})\boldsymbol{S}_i^z, \tag{2.95c}$$

and

$$\vec{\boldsymbol{V}}_{j,\mathrm{N}} = \vec{\boldsymbol{V}}_j + \gamma_{\mathrm{s}}\vec{b}_j, \tag{2.96}$$

with included noise. In fact, $\boldsymbol{V}_j^x$ and $\boldsymbol{V}_j^y$ are essentially different from the original Overhauser field components (2.22) due to the additional terms $\propto \boldsymbol{S}^x\boldsymbol{S}^y$ in the Hamiltonian (2.94). In the original system, these terms are eliminated through the strong field and the RWA. Though, it is still justified to neglect local inhomogeneities due to the large number of contributions in (2.95). The Hamiltonian for the particular spin $\boldsymbol{S}_0$ reads

$$\boldsymbol{H}_{\mathrm{ZF},0} = \vec{\boldsymbol{V}}_{0,\mathrm{N}}\cdot\vec{\boldsymbol{S}}_0. \tag{2.97}$$

Henceforth, the site index (0) of the Overhauser field is omitted. In the following, we employ S-DMFT according to the steps presented in Sec. 2.3.1.

The first step is to justify that the Overhauser field in (2.97) can be replaced by a classical mean-field. To do so, we stress that although the new and the original Overhauser field (2.22) differ from each other, their fundamental structure, namely a large sum over terms that are linear in spin operators, is the same. Therefore, the Frobenius norms of the commutators are still suppressed relative to the norms of the components. Moreover, back actions of $\boldsymbol{S}_0$ can still be neglected so that concludingly, the first step of S-DMFT is justified. The Overhauser field $\vec{\boldsymbol{V}}_\mathrm{N}$ is replaced by a time-dependent mean-field $\vec{V}(t)$ resulting in

$$\boldsymbol{H}_{\mathrm{ZF,mf}}(t) = \vec{V}(t) \cdot \vec{\boldsymbol{S}}_0. \tag{2.98}$$

The second step of S-DMFT aims at determining the behavior, i.e., the distribution of the mean-field. Completely analogous to Sec. 2.3.3, we find that it behaves Gaussian with zero average due to the central limit theorem. Note that the analytical argument provided in App. A is done for arbitrary couplings $\propto \boldsymbol{S}^\alpha \boldsymbol{S}^\beta$ and thus also serves for this case.

Finally, as part of the third step, we calculate the mean-field autocorrelations and thereby formulate a self-consistency problem. At first, we discuss the symmetries of the system to figure out, whether any single-spin autocorrelations vanish:

(i) Since the density operator is proportional to the unity, time translation invariance (TTI) still holds (see (2.45)).

(ii) Applying time reversal to the Hamiltonian (2.94) leads to a sign in front of $\boldsymbol{H}_\mathrm{N}$, as it is linear in spin operators. However, this sign does not affect any physical expectation values due to the noise averaging (2.92). Thus, time reversal symmetry (TRS) is also valid in the zero-field limit (see (2.50)).

(iii) In contrast to this, $\pi/2$-spin-rotational symmetry around z (SRZ) is not given here because the Hamiltonian (2.94) is clearly not invariant by the corresponding transformation. However, we remind the reader that any local inhomogeneities of the system are neglected so that every spin has the same environment on average. According to this, it is certainly justified to assume the system to be invariant under a real-space rotation at $\pi/2$ around z. Applying this rotation in both the spin space and the real space (BRZ) leaves the dipolar part of the Hamiltonian (2.89) invariant because obviously all of the scalar products remain unchanged. In the noise Hamiltonian, on the other hand, the rotation leads to

$$b_i^x \boldsymbol{S}_i^x + b_i^y \boldsymbol{S}_i^y \longrightarrow b_i^x \boldsymbol{S}_i^y - b_i^y \boldsymbol{S}_i^x \tag{2.99}$$

which, again, does not harm any physical expectation values due to the noise averaging (2.92). In conclusion, BRZ symmetry is fulfilled in the zero-field limit.

With aid of these observations, we deduce

$$g^{\alpha\beta}(t) = 0, \qquad \forall \alpha \neq \beta, \tag{2.100a}$$

$$g^{xx}(t) = g^{yy}(t), \tag{2.100b}$$

with the same manner as in Sec. 2.3.5. This leads to

$$\overline{V^x(t)V^z(0)} = \overline{V^z(t)V^x(0)} = \overline{V^y(t)V^z(0)} = \overline{V^z(t)V^y(0)} = 0, \tag{2.101}$$

because they only consist of vanishing single-spin autocorrelations (2.100a). Note that this conclusion cannot be drawn for $\overline{V^x(t)V^y(0)}$ and $\overline{V^y(t)V^x(0)}$ at this point because they could contain non-zero contributions through $g^{xx}(t)$ and $g^{yy}(t)$. In summary, we derive self-consistency conditions connecting three single-spin autocorrelations to five mean-field autocorrelations. While neglecting correlations between different sites and assuming each spin to behave the same on average, we obtain

$$\overline{V^x(t)V^x(0)} = \langle \boldsymbol{V}^x_{\mathrm{N}}(t)\boldsymbol{V}^x_{\mathrm{N}}(0)\rangle = \langle \boldsymbol{V}^x(t)\boldsymbol{V}^x(0)\rangle + \langle \gamma_{\mathrm{s}}^2\,(b^x)^2\rangle \tag{2.102a}$$

$$\begin{aligned} &= \sum_{i>0} R_{i0}^4 J\left(R_{i0}\right)^2 \Big(\left(1-3\cos^2(\varphi_{i0})\right)^2 \langle \boldsymbol{S}_i^x(t)\boldsymbol{S}_i^x(0)\rangle \\ &\qquad - 3\left(1-3\cos^2(\varphi_{i0})\right)\cos(\varphi_{i0})\sin(\varphi_{i0})\langle \boldsymbol{S}_i^x(t)\boldsymbol{S}_i^y(0)\rangle \\ &\qquad - 3\left(1-3\cos^2(\varphi_{i0})\right)\cos(\varphi_{i0})\sin(\varphi_{i0})\langle \boldsymbol{S}_i^y(t)\boldsymbol{S}_i^x(0)\rangle \\ &\qquad + 9\cos^2(\varphi_{i0})\sin^2(\varphi_{i0})\langle \boldsymbol{S}_i^y(t)\boldsymbol{S}_i^y(0)\rangle \Big) + \gamma_{\mathrm{s}}^2\overline{b^2}^{\mathrm{N}} \end{aligned} \tag{2.102b}$$

$$\begin{aligned} &\overset{(2.100)}{=} \sum_{i>0} R_{i0}^4 J\left(R_{i0}\right)^2 \Big(\left(1-3\cos^2(\varphi_{i0})\right)^2 \\ &\qquad + 9\cos^2(\varphi_{i0})\sin^2(\varphi_{i0})\Big)\langle \boldsymbol{S}_i^x(t)\boldsymbol{S}_i^x(0)\rangle + \gamma_{\mathrm{s}}^2\overline{b^2}^{\mathrm{N}} \end{aligned} \tag{2.102c}$$

$$= J_{\perp,1}^2\, g^{xx}(t) + \gamma_{\mathrm{s}}^2\overline{b^2}^{\mathrm{N}}, \tag{2.102d}$$

where we defined

$$J_{\perp,1}^2 := \sum_{i>0} R_{i0}^4 J\left(R_{i0}\right)^2 \Big(\left(1-3\cos^2(\varphi_{i0})\right)^2 + 9\cos^2(\varphi_{i0})\sin^2(\varphi_{i0})\Big) \tag{2.103a}$$

$$= \sum_{i>0} R_{i0}^4 J\left(R_{i0}\right)^2 \left(1+3\cos^2(\varphi_{i0})\right). \tag{2.103b}$$

With the same manner, the other mean-field autocorrelations yield

$$\overline{V^y(t)V^y(0)} = J_{\perp,2}^2\, g^{xx}(t) + \gamma_{\mathrm{s}}^2\overline{b^2}^{\mathrm{N}} \tag{2.104a}$$

$$\overline{V^z(t)V^z(0)} = J_{\parallel}^2\, g^{zz}(t) + \gamma_{\mathrm{s}}^2\overline{b^2}^{\mathrm{N}} \tag{2.104b}$$

$$\overline{V^x(t)V^y(0)} = \overline{V^y(t)V^x(0)} = J_{\mathrm{c}}^2\, g^{xx}(t) \tag{2.104c}$$

wherein

$$J_{\perp,2}^2 = \sum_{i>0} R_{i0}^4 J\left(R_{i0}\right)^2 \left(1 + 3\sin^2(\varphi_{i0})\right), \tag{2.105a}$$

$$J_{\parallel}^2 = \sum_{i>0} R_{i0}^4 J\left(R_{i0}\right)^2, \tag{2.105b}$$

$$J_{\mathrm{c}}^2 = \sum_{i>0} R_{i0}^4 J\left(R_{i0}\right)^2 3\cos(\varphi_{i0})\sin(\varphi_{i0}). \tag{2.105c}$$

However, we stress that the introduced couplings must be invariant under rotation at $\pi/2$ around z, since this symmetry is assumed in (iii). Applying the transformation leads to

$$J_{\perp,1}^2 \longrightarrow J_{\perp,2}^2, \qquad J_{\perp,2}^2 \longrightarrow J_{\perp,1}^2, \tag{2.106a}$$

$$J_{\parallel}^2 \longrightarrow J_{\parallel}^2, \qquad J_{\mathrm{c}}^2 \longrightarrow -J_{\mathrm{c}}^2. \tag{2.106b}$$

Thus, we find that

$$J_{\perp,1}^2 = J_{\perp,2}^2 =: J_{\perp}^2, \tag{2.107a}$$

$$J_{\mathrm{c}}^2 = 0, \tag{2.107b}$$

in consistency with our previous assumptions. By means of the continuum limit, we estimate the remaining coupling constants

$$J_{\parallel}^2 \approx n_0 \int_0^{2\pi} \mathrm{d}\varphi \int_{r_{\min}}^{\infty} \mathrm{d}R R^5 J(R)^2 = \frac{\mu_0^2 \gamma_{\mathrm{s}}^4}{32\pi} \frac{1}{r_{\min}^6}, \tag{2.108a}$$

$$J_{\perp}^2 \approx n_0 \int_0^{2\pi} \mathrm{d}\varphi \left(1 + 3\sin^2(\varphi)\right) \int_{r_{\min}}^{\infty} \mathrm{d}R R^5 J(R)^2 = \frac{5}{2} J_{\parallel}^2. \tag{2.108b}$$

Furthermore, we choose

$$J_{\parallel} = \frac{\mu_0 \mu_{\mathrm{B}}^2}{\sqrt{2\pi}} \frac{1}{r_{\min}^3} = 4\sqrt{2} J_{\mathrm{Q}}(\alpha_{\mathrm{mag}}) \tag{2.109}$$

to be the natural energy scale so that the time is measured in units of $J_{\parallel}^{-1}$. Finally, by introducing the unitless quantity

$$C_{\mathrm{ZF}} = \frac{1}{J_{\parallel}^2} \gamma_{\mathrm{s}}^2 \overline{b^2}^{\mathrm{N}} \overset{(2.109)}{=} \frac{C}{2}, \tag{2.110}$$

the self-consistency conditions reduce to

$$v^{xx}(t) = v^{yy}(t) = J_{\parallel}^2 \left(C_{\mathrm{ZF}} + \frac{5}{2} g^{xx}(t) \right), \tag{2.111a}$$

$$v^{zz}(t) = J_{\parallel}^2 \left(C_{\mathrm{ZF}} + g^{zz}(t) \right). \tag{2.111b}$$

Similar to Sec. 2.4, we consider the case of a large C_{ZF} analytically. To this end, we neglect all other interactions against that of the noise so that

$$\boldsymbol{H}_{0,\mathrm{N}} = \vec{\boldsymbol{S}}_0 \cdot \vec{b}, \tag{2.112}$$

where $\vec{b}$ follows from the distribution

$$p(\vec{b}) = \left(2\pi\overline{b^2}^{\mathrm{N}}\right)^{-\frac{3}{2}} \mathrm{e}^{-\left(\vec{b}\right)^2\left(2\overline{b^2}^{\mathrm{N}}\right)^{-1}}. \tag{2.113}$$

Basically, this issue was also treated in Ref. [8] in a different context. There, the hyperfine interaction between an electron spin and an ensemble of nuclei is described through the CSM. To gain access to the short-time dynamics, the Overhauser field is replaced by a static isotropic Gaussian random field leading to the same theoretical issue. We adopt their results for the averaged electron-spin polarization [8]

$$\langle \vec{\boldsymbol{S}}_0(t)\rangle = \frac{\vec{\boldsymbol{S}}_0(0)}{3}\left(1 + 2\left(1 - 2\frac{t^2}{T_\Delta^2}\right)\mathrm{e}^{-\frac{t^2}{T_\Delta^2}}\right), \tag{2.114}$$

where

$$T_\Delta = \frac{1}{\mu_{\mathrm{B}} g_{\mathrm{s}} \Delta_B}, \qquad \Delta_B = \sqrt{2\overline{b^2}^{\mathrm{N}}}. \tag{2.115}$$

Thus, we find

$$g_{\mathrm{app}}^{\alpha\alpha}(t) = \frac{1}{12}\left(1 + 2\left(1 - 2t^2 J_\parallel^2 C_{\mathrm{ZF}}\right)\mathrm{e}^{-t^2 J_\parallel^2 C_{\mathrm{ZF}}}\right) \tag{2.116}$$

in the zero-field limit and for large C. In Sec. 4.3, this analytical prediction is compared to our numerical results. The following chapter treats the numerical implementation of the derived self-consistency problems.

3 Methods

In the previous chapter we applied S-DMFT to the considered surface spin system and derived self-consistency conditions linking single-spin autocorrelations to mean-field autocorrelations. In the current chapter we intend to provide a numerical iteration procedure by which the autocorrelations can be computed. At first, we present a step-by-step pseudo-algorithm to solve the self-consistency problem. Subsequently, we expound on how to sample dynamic Gaussian random variables which obey an autocorrelation given at equidistant time steps. Finally, an efficient method to compute time evolution operators is furnished. Technical refinements concerning the choice of the numerical parameters are discussed in the next chapter during an error analysis in Sec. 4.1. It is necessary to mention that we denote matrices by double underlined letters throughout this chapter.

3.1 Pseudo-algorithm for the self-consistency problem

As already mentioned, we solve the self-consistency problem through numerical iteration. To this end, one sets the initial mean-field autocorrelations $v^{\alpha\beta}_{(0)}(t_m)$ on an equidistant time domain $t_m := m\delta t, m \in [0, 1, ..., L]$, while regarding starting conditions and symmetries of the system. Subsequently, they are inserted to the algorithm and optimized during the iteration-steps $(n) \to (n+1)$. The iteration stops, when the error between the latest $(n+1)$ and the previous (n) results exceeds a certain error threshold. The estimation of the iteration-error $\Delta I_{(n+1)}$ and the choice of the threshold ΔI_{th} is discussed in Sec. 4.1.

Basically, the algorithm (1) consists of three nested loops: one for the iteration, one for the statistical simulation and one for the time evolution. At first during an iteration-step, the covariance matrix is constructed from the latest mean-field autocorrelations according to

$$M^{\alpha\beta}_{m_1 m_2} = v^{\alpha\beta}_{(n)}(|t_{m_1} - t_{m_2}|), \qquad m_1, m_2 \in [0, ..., L], \tag{3.1}$$

and then diagonalized by

$$\underline{\underline{D}} = \underline{\underline{O}}^{\top} \underline{\underline{M}}\, \underline{\underline{O}}. \tag{3.2}$$

Right after this, the loop for the statistical simulation starts. Each of the M runs begins with drawing a single temporal course

$$\vec{V}_{(i)}(0 \to t_L) := \left\{ \vec{V}_{(i)}(0), ..., \vec{V}_{(i)}(t_L) \right\} \tag{3.3}$$

of the mean-field through $\underline{\underline{D}}$ and $\underline{\underline{O}}$. For details about the construction of the covariance matrix and the mean-field sampling, see Sec. 3.2. Next, the loop for the time evolution starts. Throughout every run, the time evolution operator propagating from t_m to t_{m+1} is computed from the considered mean-field Hamiltonian at both times. We refer to Sec. 3.3 for an efficient method to perform this. Moreover, the time evolution operator propagating from 0 to t_{m+1} is determined using group property. The final step in the loop for the time evolution is to compute the single-spin autocorrelations at t_{m+1} for the drawn sample (i) through

$$\tilde{g}^{\alpha\beta}_{(n+1),(i)}(t_{m+1}) = \langle \boldsymbol{S}^{\alpha}(t_{m+1})\boldsymbol{S}^{\beta}(0)\rangle. \tag{3.4}$$

With aid of the Pauli matrices

$$\underline{\underline{\sigma}}^{x} = \begin{pmatrix} 0 & 1 \\ 1 & 0 \end{pmatrix}, \qquad \underline{\underline{\sigma}}^{y} = \begin{pmatrix} 0 & -\mathtt{i} \\ \mathtt{i} & 0 \end{pmatrix}, \qquad \underline{\underline{\sigma}}^{z} = \begin{pmatrix} 1 & 0 \\ 0 & -1 \end{pmatrix}, \tag{3.5}$$

as well as

$$\underline{\underline{U}}(t,0) = \begin{pmatrix} U_{11} & U_{12} \\ U_{21} & U_{22} \end{pmatrix}, \tag{3.6}$$

the autocorrelations can be simplified yielding

$$\tilde{g}^{xx}(t) = \tfrac{1}{4}\mathtt{Re}\left(U_{11}\overline{U}_{22} + U_{12}\overline{U}_{21}\right), \tag{3.7a}$$
$$\tilde{g}^{yy}(t) = \tfrac{1}{4}\mathtt{Re}\left(U_{11}\overline{U}_{22} - U_{12}\overline{U}_{21}\right), \tag{3.7b}$$
$$\tilde{g}^{zz}(t) = \tfrac{1}{4}\left(|U_{11}|^2 + |U_{22}|^2 - 1\right), \tag{3.7c}$$
$$\tilde{g}^{xy}(t) = \tfrac{1}{4}\mathtt{Im}\left(U_{11}\overline{U}_{22} + U_{21}\overline{U}_{12}\right), \tag{3.7d}$$
$$\tilde{g}^{yx}(t) = \tfrac{1}{4}\mathtt{Im}\left(U_{22}\overline{U}_{11} + U_{21}\overline{U}_{12}\right), \tag{3.7e}$$
$$\tilde{g}^{xz}(t) = \tfrac{1}{4}\mathtt{Re}\left(U_{11}\overline{U}_{21} - U_{22}\overline{U}_{12}\right), \tag{3.7f}$$
$$\tilde{g}^{zx}(t) = \tfrac{1}{4}\mathtt{Re}\left(U_{11}\overline{U}_{12} - U_{22}\overline{U}_{21}\right), \tag{3.7g}$$
$$\tilde{g}^{yz}(t) = \tfrac{1}{4}\mathtt{Im}\left(U_{21}\overline{U}_{11} + U_{12}\overline{U}_{22}\right), \tag{3.7h}$$
$$\tilde{g}^{yx}(t) = \tfrac{1}{4}\mathtt{Im}\left(U_{11}\overline{U}_{12} + U_{22}\overline{U}_{21}\right). \tag{3.7i}$$

After they are computed for all time steps and samples both the time evolution and the statistical simulation loop end. Then, the results are averaged according to

$$g^{\alpha\beta}_{(n+1)}(t_m) = \frac{1}{M}\sum_{i=1}^{M} \tilde{g}^{\alpha\beta}_{(n+1),(i)}(t_m), \qquad \forall m \in [1, ..., L], \tag{3.8}$$

where M is the number of drawn samples. Moreover, we regard the starting condition

$$g^{\alpha\beta}_{(n+1)}(0) = \frac{1}{8}\mathrm{Tr}\left(\underline{\underline{\sigma}}^{\alpha}\underline{\underline{\sigma}}^{\beta}\right) = \frac{\delta_{\alpha\beta}}{4}. \tag{3.9}$$

Finally, the new mean-field autocorrelations $v^{\alpha\beta}_{(n+1)}(t_m)$ are determined through the self-consistency conditions (2.68). In the next section we expound on how to sample the Gaussian mean-field to clarify lines 3,4 and 7 of the algorithm.

Algorithm 1: Iteration procedure

$n = 0$ // iteration-step
do
  construct the covariance matrix $\underline{\underline{M}}$ from $v^{\alpha\beta}_{(n)}(t_m)$
  diagonalize $\underline{\underline{M}}$
  for $i = 1$ **to** M // statistical simulation loop
  do
    draw $\vec{V}_{(i)}(0 \to t_L)$
    for $m = 0$ **to** $L - 1$ // time evolution loop
    do
      estimate $\boldsymbol{H}\left(\vec{V}_{(i)}(t_m)\right)$ and $\boldsymbol{H}\left(\vec{V}_{(i)}(t_{m+1})\right)$
      compute $\boldsymbol{U}_{(i)}(t_{m+1}, t_m)$
      $\boldsymbol{U}_{(i)}(t_{m+1}, 0) = \boldsymbol{U}_{(i)}(t_{m+1}, t_m) \cdot \boldsymbol{U}_{(i)}(t_m, 0)$
      compute all $\tilde{g}^{\alpha\beta}_{(n+1),(i)}(t_{m+1})$
  determine the average $g^{\alpha\beta}_{(n+1)}(t_m)$ for all time steps
  determine $v^{\alpha\beta}_{(n+1)}(t_m)$ from $g^{\alpha\beta}_{(n+1)}(t_m)$ by the self-consistency conditions
  $n \leftarrow n + 1$
while $\Delta I_{(n+1)} > \Delta I_{th}$ // iteration loop

3.2 Sampling of dynamic Gaussian random variables

To sample a Gaussian random field obeying a given autocorrelation we use the method provided in Ref. [38] (pp.177-182). First, we discuss the case where all correlations $v^{\alpha\beta}(t)$ with $\alpha \neq \beta$ vanish. There, the sampling can be handled separately for every dimension and, thus, reduces to three one-dimensional problems.

We consider a discretized autocorrelation function

$$v^{\alpha\alpha}(t_m) = \overline{V^\alpha(t_m) V^\alpha(0)} \tag{3.10}$$

on a time domain

$$t_m = m\delta t, \qquad m \in [0, ..., L]. \tag{3.11}$$

Our aim is, to sample a time-evolving field

$$\vec{V}^\alpha := (V^\alpha(0), ..., V^\alpha(t_L))^\top \tag{3.12}$$

fulfilling the multi-dimensional Gaussian distribution

$$p(\vec{V}^\alpha) = \frac{1}{(2\pi)^{(L+1)/2}\sqrt{\det \underline{\underline{M}}^{\alpha\alpha}}} \exp\left(-\frac{1}{2}\left(\vec{V}^\alpha\right)^\top \left(\underline{\underline{M}}^{\alpha\alpha}\right)^{-1} \vec{V}^\alpha\right), \tag{3.13}$$

where $\underline{\underline{M}}^{\alpha\alpha}$ is the covariance matrix and

$$M^{\alpha\alpha}_{m_1 m_2} = v^{\alpha\alpha}(|t_{m_1} - t_{m_2}|) \tag{3.14}$$

its elements. Note that the vector arrow in $\vec{V}^{\alpha}$ does not refer to the spatial dimensions here but to the time discretization. In general, $\underline{\underline{M}}^{\alpha\alpha}$ is non-diagonal so that the variables $V^{\alpha}(t_m)$ cannot be drawn independently of each other.

In the case of white noise, however, the covariance matrix results from

$$h^{\alpha\alpha}(|t_{m_1} - t_{m_2}|) = \sigma^2_{m_1}\delta_{m_1 m_2} \tag{3.15}$$

and is thus diagonal due to the Kronecker delta. Thereby, the multi-dimensional Gaussian distribution factorizes into a product of one-dimensional Gaussian distributions given by

$$p_{\mathrm{wn}}(V^{\alpha}(t_m)) = \frac{1}{\sqrt{2\pi\sigma^2_m}} \exp\left(-\frac{(V^{\alpha})^2(t_m)}{2\sigma^2_m}\right). \tag{3.16}$$

Correspondingly, one simply draws $(L+1)$ independent Gaussian random variables to sample the fluctuations $\vec{V}^{\alpha}$. In the following, this idea is used to solve the general problem.

The covariance matrix $\underline{\underline{M}}^{\alpha\alpha}$ is real and symmetric. Hence, it can be diagonalized by an orthogonal transformation $\underline{\underline{O}}$ based on

$$\underline{\underline{D}} = \underline{\underline{O}}^{\top}\,\underline{\underline{M}}^{\alpha\alpha}\,\underline{\underline{O}}, \tag{3.17}$$

where $\underline{\underline{D}}$ is the diagonal matrix containing the eigenvalues d_m. With aid of this, we rewrite the multi-dimensional Gaussian distribution (3.13) corresponding to

$$p(\vec{V}^{\alpha}) = \frac{1}{(2\pi)^{(L+1)/2}\sqrt{\det\underline{\underline{O}}\,\underline{\underline{D}}\,\underline{\underline{O}}^{\top}}} \exp\left(-\frac{1}{2}\left(\vec{V}^{\alpha}\right)^{\top}\underline{\underline{O}}\,\underline{\underline{D}}^{-1}\underline{\underline{O}}^{\top}\,\vec{V}^{\alpha}\right) \tag{3.18a}$$

$$= \frac{1}{(2\pi)^{(L+1)/2}\sqrt{\det\underline{\underline{D}}}} \exp\left(-\frac{1}{2}\left(\vec{K}^{\alpha}\right)^{\top}\underline{\underline{D}}^{-1}\,\vec{K}^{\alpha}\right), \tag{3.18b}$$

where we defined new random variables

$$\vec{K}^{\alpha} := (K^{\alpha}_0, ..., K^{\alpha}_L)^{\top} = \underline{\underline{O}}^{\top}\vec{V}^{\alpha}. \tag{3.19}$$

Since $\underline{\underline{D}}^{-1}$ is diagonal, we can factorize (3.18b) into $(L+1)$ one-dimensional Gaussian distributions reading

$$p_{\mathrm{diag}}(K^{\alpha}_m) = \frac{1}{\sqrt{2\pi d_m}} \exp\left(-\frac{(K^{\alpha}_m)^2(t_m)}{2d_m}\right). \tag{3.20}$$

Correspondingly, we present the following strategy:

1. Construct the covariance matrix based on (3.14).
2. Diagonalize $\underline{\underline{M}}^{\alpha\alpha}$ according to (3.17) and estimate the eigenvalues d_m and eigenvectors $\vec{o}_m$ which form the columns of the orthogonal transformation $\underline{\underline{O}}$.
3. Draw Gaussian random numbers K_m^α in the diagonal basis with the variance $\sigma_m^2 = d_m$ and zero average.
4. Calculate Gaussian random numbers obeying (3.13) through back-transformation

$$\vec{V}^\alpha = \underline{\underline{O}}\vec{K}^\alpha. \tag{3.21}$$

In step 2 one may obtain negative eigenvalues due to numerical deviations. If their absolut values are small ($|d_m| < \propto 10^{-6} - 10^{-5}$ [38]) they can be set to zero so that the variances are well defined.

For non-vanishing autocorrelations $v_{(0)}^{\alpha\beta}(t_m)$, $\alpha \neq \beta$, the three-dimensional problem is not separable as above. Instead, we consider a $(3L+3)$-dimensional covariance matrix according to

$$\underline{\underline{M}} = \begin{pmatrix} \underline{\underline{M}}^{xx} & \underline{\underline{M}}^{xy} & \underline{\underline{M}}^{xz} \\ \underline{\underline{M}}^{yx} & \underline{\underline{M}}^{yy} & \underline{\underline{M}}^{yz} \\ \underline{\underline{M}}^{zx} & \underline{\underline{M}}^{zy} & \underline{\underline{M}}^{zz} \end{pmatrix}. \tag{3.22}$$

Its matrix elements follow from the relation

$$M_{m_1 m_2}^{\alpha\beta} = v^{\alpha\beta}(|t_{m_1} - t_{m_1}|). \tag{3.23}$$

The remaining steps 2, 3 and 4 are carried out with $(3L+3)$-dimensional vectors

$$\vec{V} = \left(\left(\vec{V}^x\right)^\top, \left(\vec{V}^y\right)^\top, \left(\vec{V}^z\right)^\top \right)^\top = (V^x(0), ..., V^z(t_L))^\top \tag{3.24a}$$

$$\vec{K} = (K_0, ..., K_{3L+2})^\top. \tag{3.24b}$$

Now that we explained the sampling procedure, lines 3,4 and 7 of the algorithm are clarified. In what follows, we present the method of commutator-free exponential time propagation.

3.3 Commutator-free exponential time propagation

In line 11 of the algorithm, we compute time evolution operators propagating over short time steps. The aim of this section is to furnish a method for computing these operators efficiently. At first, we remind the reader of the fundamental differential equation for the time evolution operator (TEO)

$$\mathtt{i}\partial_t \boldsymbol{U}(t, t_0) = \boldsymbol{H}(t)\boldsymbol{U}(t, t_0). \tag{3.25}$$

In that case, where the Hamiltonian commutes with itself at different times according to

$$[\boldsymbol{H}(t), \boldsymbol{H}(t_0)] = 0, \qquad \forall t, t_0, \tag{3.26}$$

the TEO simply yields

$$\boldsymbol{U}(t, t_0) = \mathrm{e}^{-\mathtt{i}\int_{t_0}^{t} \mathrm{d}\tau\, \boldsymbol{H}(\tau)}. \tag{3.27}$$

However, the general case where the commutator is non-zero is much more difficult and usually not solvable without a truncation scheme. For short-step propagators it is certainly practical to use an expansion in orders of t, such as the Magnus expansion [37, 41–43]. It is given by

$$\boldsymbol{U}(t, t_0) = \mathrm{e}^{\boldsymbol{\Omega}(t,t_0)} = \mathrm{e}^{\sum_{k=1}^{\infty} \boldsymbol{\Omega}_k(t,t_0)}, \tag{3.28}$$

where the $\boldsymbol{\Omega}_k(t, t_0)$ are multi-dimensional time integrals over nested commutators of the Hamiltonian. An Nth-order truncation of the expansion according to

$$\boldsymbol{U}(t, t_0) \approx \mathrm{e}^{\sum_{k=1}^{N} \boldsymbol{\Omega}_k(t,t_0)}, \tag{3.29}$$

leads to an error of the order [43]

$$\Delta q = \delta t^{N+1}, \tag{3.30}$$

where $\delta t = t - t_0$ is the step width. Exemplarily, we provide the first three orders [42]

$$\boldsymbol{\Omega}_1(t, t_0) = -\mathtt{i} \int_{t_0}^{t} \mathrm{d}\tau\, \boldsymbol{H}(\tau), \tag{3.31a}$$

$$\boldsymbol{\Omega}_2(t, t_0) = -\frac{1}{2} \int_{t_0}^{t} \mathrm{d}\tau_1 \int_{t_0}^{\tau_1} \mathrm{d}\tau_2 \left[\boldsymbol{H}(\tau_1), \boldsymbol{H}(\tau_2)\right], \tag{3.31b}$$

$$\begin{aligned} \boldsymbol{\Omega}_3(t, t_0) = \frac{\mathtt{i}}{6} \int_{t_0}^{t} \mathrm{d}\tau_1 \int_{t_0}^{\tau_1} \mathrm{d}\tau_2 \int_{t_0}^{\tau_2} \mathrm{d}\tau_3 \Big(&[\boldsymbol{H}(\tau_1), [\boldsymbol{H}(\tau_2), \boldsymbol{H}(\tau_3)]] \\ &+ [\boldsymbol{H}(\tau_3), [\boldsymbol{H}(\tau_2), \boldsymbol{H}(\tau_1)]] \Big), \end{aligned} \tag{3.31c}$$

which indicate that the complexity strongly increases with k. Because the computation of nested commutators in higher orders of the Magnus expansion is very costly, we turn to another truncation scheme which avoids commutators in general. Before doing this, however, we stress that the Magnus expansion has an important property: it preserves operator structures such as Lie algebras [37, 43]. This is very advantageous for the considered mean-field Hamiltonians $\boldsymbol{H}(t)$ because all of them consist of a superposition of spin operators at any times. Clearly, any integrations and nested commutators occurring in $\boldsymbol{\Omega}(t, t_0)$ do not violate this structure due to the fundamental commutator relation

$$\left[\boldsymbol{S}^{\alpha}, \boldsymbol{S}^{\beta}\right] = \mathtt{i} \sum_{\gamma} \epsilon_{\alpha\beta\gamma} \boldsymbol{S}^{\gamma}. \tag{3.32}$$

By means of this, any truncation of $\boldsymbol{\Omega}(t, t_0)$ is skew-hermitian so that unitarity of the TEO is ensured. Estimating it by other methods, e.g., solving the differential equation (3.25) directly, may lead to violation of unitarity and therefore to numerical instability. In the following, we introduce an efficient truncation scheme which also provides unitary TEOs.

We use the method of commutator-free exponential time propagation (CFET) from Ref. [43]. The fundamental idea is to start from the Magnus expansion and split the single exponential into a product of multiple exponentials by using the Baker-Campbell-Hausdorff (BCH) formula

$$\exp\left(\sum_{u=1}^{s} \boldsymbol{X}_u + \frac{1}{2}\sum_{1\leq u<v\leq s} [\boldsymbol{X}_u, \boldsymbol{X}_v] + ...\right) = \mathrm{e}^{\boldsymbol{X}_1} ... \, \mathrm{e}^{\boldsymbol{X}_s}. \tag{3.33}$$

By this, the numerical effort is reduced because the exponents on the right-hand side are computed commutator-free. To implement this idea, we first expand the Hamiltonian in the shifted Legendre polynomials which are given by recurrence

$$P_0(t) = 1, \tag{3.34a}$$
$$P_1(t) = 2t - 1, \tag{3.34b}$$
$$P_{j+1}(t) = \frac{2j+1}{j+1}(2t-1)P_j(t) - \frac{j}{j+1}P_{j-1}(t). \tag{3.34c}$$

Usefull properties are symmetry with respect to $t = \frac{1}{2}$ and orthogonality according to

$$P_j(1-t) = (-1)^j P_j(t), \tag{3.35a}$$
$$\int_0^1 P_j(t)P_l(t)\mathrm{d}t = \frac{1}{2j+1}\delta_{jl}. \tag{3.35b}$$

Moreover, one finds

$$\int_0^1 f(t)P_j(t)\mathrm{d}t = 0 \tag{3.36}$$

for any polynomials $f(t)$ of degree less than j. Now, to compute a short-step propagator $\boldsymbol{U}^{(N)}(t_0 + \delta t, t_0)$ of order N we expand the Hamiltonian

$$\boldsymbol{H}(t) = \frac{1}{\delta t}\left(\sum_{j=1}^{N} \boldsymbol{A}_j P_{j-1}\left(\frac{t-t_0}{\delta t}\right) + \mathcal{O}\left(\delta t^{N+1}\right)\right), \qquad t \in [t_0, t_0 + \delta t], \tag{3.37}$$

where the operator-valued coefficients read

$$\boldsymbol{A}_j = -\mathtt{i}(2j-1)\int_{t_0}^{t_0+\delta t} \boldsymbol{H}(\tau)P_{j-1}\left(\frac{\tau - t_0}{\delta t}\right)\mathrm{d}\tau. \tag{3.38}$$

With aid of (3.36), we conclude that the first contribution of $\boldsymbol{H}(\tau)$ in the integral (3.38) is of order δt^{j-1}. Regarding this and the differential $\mathrm{d}\tau$ the coefficients $\boldsymbol{A}_j$ are of order

δt^j so that the error in the large bracket of (3.37) is finally of order δt^{N+1}. We insert this expansion into the Magnus expansion (3.28) and exemplarily collect all terms up to order δt^4 resulting in

$$\boldsymbol{\Omega}(t,0) = \boldsymbol{A}_1 - \frac{1}{6}\left[\boldsymbol{A}_1, \boldsymbol{A}_2\right] + \mathcal{O}\left(\delta t^5\right). \tag{3.39}$$

Now, to eliminate the commutators one chooses a general approach for an Nth-order CFET with s exponentials according to

$$\boldsymbol{U}^{(N)}_{\mathrm{CF}:s}(t,0) = \mathrm{e}^{\boldsymbol{X}_1} \ldots \mathrm{e}^{\boldsymbol{X}_s}, \tag{3.40}$$

where we defined

$$\boldsymbol{X}_u = \sum_{j=1}^{N} f_{u,j} \boldsymbol{A}_j. \tag{3.41}$$

The prefactors $f_{u,j}$ are computed by combining the exponentials through the BCH formula (3.33) and comparing the resulting exponential to the reshaped Magnus expansion (3.39). This requires to work in a so-called Hall basis because the expanded terms in (3.39) are not unique in contrast to the Magnus expansion. See Ref. [43] for more details. Summarizingly, the use of CFETs is advantageous for our applications because the computation of TEOs happens commutator-free and furthermore their unitarity is ensured.

In this thesis we employ a second-order CFET reading [43]

$$\boldsymbol{U}^{(2)}_{\mathrm{CF}:1}(t+\delta t, t) = \mathrm{e}^{\boldsymbol{A}_1}, \tag{3.42}$$

which is equivalent to the first-order Magnus expansion (3.31a), and an optimized fourth-order CFET given by [43]

$$\begin{aligned}\boldsymbol{U}^{(4)}_{\mathrm{CF}:3,\mathrm{Opt}}(t+\delta t, t) = \exp\left(\frac{11}{40}\boldsymbol{A}_1 + \frac{20}{87}\boldsymbol{A}_2 + \frac{7}{50}\boldsymbol{A}_3\right) \exp\left(\frac{9}{20}\boldsymbol{A}_1 - \frac{7}{25}\boldsymbol{A}_3\right) \\ \cdot \exp\left(\frac{11}{40}\boldsymbol{A}_1 - \frac{20}{87}\boldsymbol{A}_2 + \frac{7}{50}\boldsymbol{A}_3\right).\end{aligned} \tag{3.43}$$

Since we use an iteration procedure to compute our results, we must conserve the number of time steps during our iteration steps. Therefore, we are limited to the Trapezoidal rule when determining the integrals (3.38). Correspondingly, the coefficients yield

$$\boldsymbol{A}_j = -\mathtt{i}(2j-1)\frac{\delta t}{2}\Big(\boldsymbol{H}(t+\delta t) - (-1)^j \boldsymbol{H}(t)\Big), \tag{3.44}$$

where we used $P_j(1) = 1$ and (3.35a). Moreover, any CFET exponents can be written as a superposition of the Pauli matrices (3.5) for the considered Hamiltonians according to

$$\mathrm{e}^{\boldsymbol{X}_u} = \mathrm{e}^{-\mathtt{i}\sum_\alpha F_\alpha \underline{\underline{\sigma}}^\alpha} = \mathrm{e}^{-\mathtt{i}\vec{F}\cdot\vec{\underline{\underline{\sigma}}}} \tag{3.45}$$

and finally simplified by

$$\mathrm{e}^{-\mathtt{i}\vec{F}\cdot\vec{\underline{\underline{\sigma}}}} = \cos\left(|\vec{F}|\right)\underline{\underline{\sigma}}^0 - \mathtt{i}\sin\left(|\vec{F}|\right)\frac{\vec{F}\cdot\vec{\underline{\underline{\sigma}}}}{|\vec{F}|}. \tag{3.46}$$

Now that all steps of the algorithm 1 have been clarified, we proceed with presenting our numerical results in the next chapter.

4 Results

In the previous chapters we described a theoretical model and furnished a corresponding implementation to compute autocorrelation functions of dipolar surface spins. On this basis, we present our numerical results including a comparison to experimental data in the current chapter. At first, we discuss numerical errors and convergence of the self-consistency problem. Subsequently, the results in the strong-field regime are shown in dependence of the magnetic noise. We fit them to experimental data and determine optimal values for energy scale and noise variance. Finally, we also present and discuss our results in the zero-field limit, where the effect of the magnetic noise is different. Pseudo random variables are drawn by the Mersenne twister generator *mt19937* implemented in the *C++ standard library*.

4.1 Error Analysis

During the modelling in 2 we already realized two error sources. While deviations by the RWA were determined to be small, the applicability of S-DMFT was rather justified qualitatively. This section provides a brief analysis of the numerical error sources. We aim at a reliable and efficient choice of the numerical parameters and furthermore some first self-checks of our algorithm. In particular, we study the statistical error, the time-discretization error and the iteration error as well as we demonstrate convergence of the self-consistency problem at the end.

4.1.1 Statistical error

Because a finite number of random variables is drawn to realize the mean-field fluctuations, the results are clearly subject to a finite statistical error. Within each iteration step we calculate the autocorrelations $\tilde{g}^{\alpha\beta}_{(i)}(t)$ for every drawn sample (i) and average over the multitude of results using

$$g^{\alpha\beta}(t) = \frac{1}{M}\sum_{i=1}^{M} \tilde{g}^{\alpha\beta}_{(i)}(t). \tag{4.1}$$

Since the single-sample results $\tilde{g}^{\alpha\beta}(t)$ are (pseudo-) independent of each other, the variance of the averaged autocorrelations yields [39]

$$\sigma^2_{\text{average}}(M,t) = \frac{1}{M}\,\sigma^2_{\text{sample}}(t), \tag{4.2}$$

where σ_{sample} is the standard deviation of a single result. Equation (4.2) is verified numerically in the following.

We consider the strong-field regime with zero noise, insert the initial mean-field autocorrelations

$$v_{(0)}^{\alpha\beta}(t) = \delta_{\alpha\beta}\frac{J_{\mathrm{Q}}^2}{4}\mathrm{e}^{-|t|J_{\mathrm{Q}}}, \qquad \forall\alpha,\beta, \tag{4.3}$$

and estimate $g^{zz}(t)$ by averaging over M different samples. In doing so, we do not iterate over the solution, as this is not necessary for an analysis of the statistical error. Moreover, the calculation is repeated $P = 500$ times each with a different set of samples. By means of this, the variance of the averaged autocorrelation $g^{zz}(t)$ is computed via

$$\sigma^2_{\text{average}}(M,t) = \overline{\left(g^{zz}(t) - \overline{g^{zz}(t)}\right)^2} = \frac{1}{P}\sum_{\rho=1}^{P}\left(g_\rho^{zz}(t)\right)^2 - \left(\frac{1}{P}\sum_{\rho=1}^{P} g_\rho^{zz}(t)\right)^2. \tag{4.4}$$

Note that we added an index ρ to the averaged autocorrelation to represent a certain set of samples. The procedure is carried out for a varying number of samples per set

$$M = 10^k, \qquad k \in \{0,1,2,3,4,5,6,7\}. \tag{4.5}$$

In order to compute errorbars of the data, we determine the variance of $(g^{zz}(t) - \overline{g^{zz}(t)})^2$ through

$$\Sigma^2(M,t) = \overline{\left((g-\overline{g})^2 - \sigma^2\right)^2} = \overline{(g-\overline{g})^4} - \sigma^4 \tag{4.6a}$$

$$= \overline{g^4} - 4\overline{g^3}\overline{g} + 8\overline{g^2}\overline{g}^2 - 4\overline{g}^4 - \overline{g^2}^2, \tag{4.6b}$$

where $g := g^{zz}(t)$. The variance of $\sigma^2_{\text{average}}$ is then given by

$$\Sigma^2_{(P)}(M,t) = \frac{\Sigma^2(M,t)}{P}, \tag{4.7}$$

which is similar to (4.2). The results for $\sigma^2_{\text{average}}$ including its standard deviation $\Sigma_{(P)}$ at $t = 4/J_{\mathrm{Q}}$ and $t = 8/J_{\mathrm{Q}}$ are plotted in Fig. 4.1.

We observe a linear trend of the data in the logarithmic representation. Therefore, we apply the fit function

$$\log\left(\sigma^2_{\text{average}}\right) = a\cdot\log(M) + \log(b) \tag{4.8a}$$

$$\sigma^2_{\text{average}} = b\cdot M^a, \tag{4.8b}$$

leading to

$$a(t_0 = 4/J_{\mathrm{Q}}) = -1.000 \pm 0.006, \qquad b(t_0 = 4/J_{\mathrm{Q}}) = 0.021 \pm 0.001, \tag{4.9a}$$

$$a(t_0 = 8/J_{\mathrm{Q}}) = -0.999 \pm 0.003, \qquad b(t_0 = 8/J_{\mathrm{Q}}) = 0.0206 \pm 0.0006. \tag{4.9b}$$

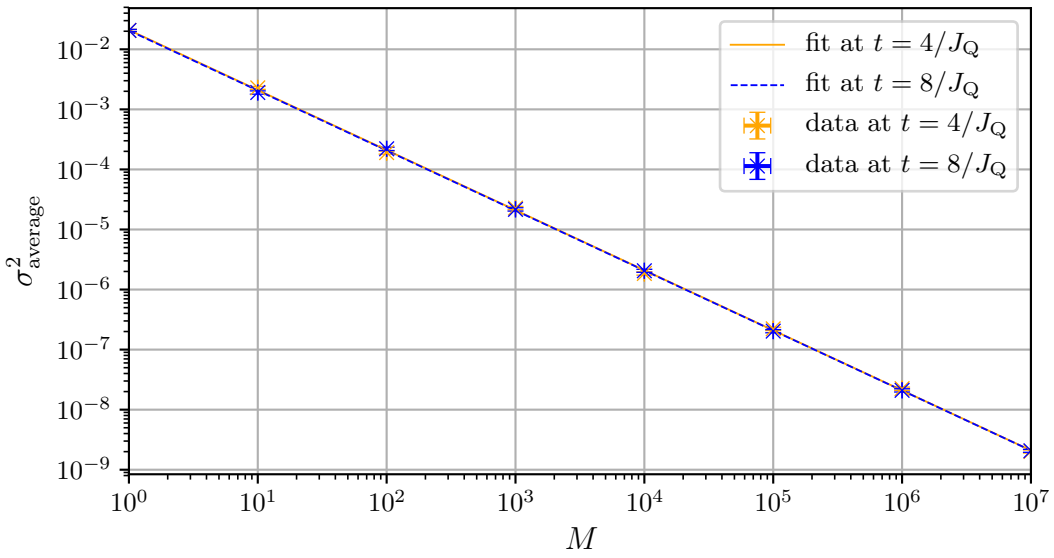

Figure 4.1: Log-log plot of the variance of the averaged autocorrelation $g^{zz}(t)$ at two different times in terms of M. The data are estimated from (4.4), (4.6b) and (4.7). The resulting fit parameters are shown in (4.9).

Since we predicted a value of $a = -1.0$ corresponding to (4.2), the numerically estimated values for a confirm the expectation. The prefactor b describes the time-dependent variance of the single-sample autocorrelation. To determine its behavior, we compute

$$\sigma^2_{\text{sample}}(t) = \frac{1}{M}\sum_{i=1}^{M}\left(\tilde{g}^{\alpha\alpha}_{(i)}(t)\right)^2 - \left(\frac{1}{M}\sum_{i=1}^{M}\tilde{g}^{\alpha\alpha}_{(i)}(t)\right)^2, \qquad \alpha \in \{x, z\}, \tag{4.10}$$

for $M = 4 \cdot 10^6$ samples. The results for the standard deviation are presented in Fig. 4.2.

Since the autocorrelations are forced to the value $\frac{1}{4}$ at $t = 0$, clearly σ_{sample} is small at the beginning. As t increases the standard deviation somehow converges to a certain value, which we estimate to be

$$\lim_{t\to\infty} \sigma_{\text{sample}}(t) = 0.144\,32 \pm 0.000\,05. \tag{4.11}$$

We present an analytical argument for this in the following.

The first thing we realize is that the average of all autocorrelations dies out over time due to decoherence, i.e.,

$$\lim_{t\to\infty} g^{\alpha\beta}(t) = \lim_{t\to\infty} \overline{\tilde{g}^{\alpha\beta}(t)} = 0 \tag{4.12}$$

and thus

$$\lim_{t\to\infty} \sigma^2_{\text{sample}}(t) = \lim_{t\to\infty} \overline{(\tilde{g}^{\alpha\beta}(t))^2}. \tag{4.13}$$

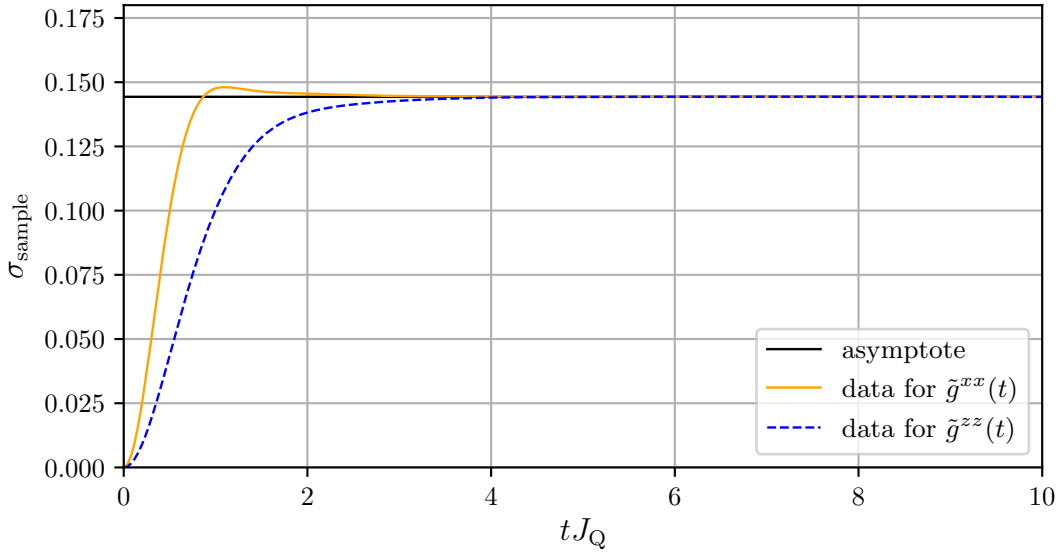

Figure 4.2: Standard deviations of the single-sample autocorrelations $\tilde{g}^{\alpha\alpha}(t)$ over time. For both autocorrelations σ_{sample} converges to an asymptote at the value (4.11).

Correspondingly, we only need to discuss the quadratic expectation value of the autocorrelations at large times. Next, we introduce the vector signal

$$\tilde{\vec{g}}_\alpha = \frac{1}{2}\text{Tr}\left(\vec{\boldsymbol{S}}(t)\boldsymbol{S}^\alpha(0)\right) \tag{4.14}$$

and the rotational matrix $\boldsymbol{R}(t)$ resulting from

$$\vec{\boldsymbol{S}}(t) = \boldsymbol{R}(t)\vec{\boldsymbol{S}}(0). \tag{4.15}$$

Inserting (4.15) into (4.14) yields

$$\tilde{\vec{g}}_\alpha = \frac{1}{2}\text{Tr}\left(\boldsymbol{R}(t)\vec{\boldsymbol{S}}(0)\boldsymbol{S}^\alpha(0)\right) = \frac{1}{4}\vec{R}_\alpha(t), \tag{4.16}$$

where

$$\vec{R}_\alpha(t) = \boldsymbol{R}(t)\,\vec{\text{e}}_\alpha. \tag{4.17}$$

For the square of the vector signal we obtain

$$\left(\tilde{\vec{g}}_\alpha\right)^2 = \frac{1}{16}\vec{R}_3(t)^2 = \frac{1}{16}, \tag{4.18}$$

where we used the orthogonality of $\boldsymbol{R}(t)$, since the time evolution operator preserves the scalar product. Obviously, this relation also holds on average. Due to (4.12) the expectation value of the column vector $\vec{R}_\alpha(t)$ vanishes at infinite times. In addition, we assume that the variance for every component of this vector is equal for $t \to \infty$. This is supported by the fact that at infinite times the spin-vector resulting from a single sample is not correlated to its initial alignment anymore. By means of this, the desired standard deviation for infinite times eventually yields

$$\lim_{t\to\infty} \sigma_{\text{sample}}(t) = \frac{1}{4\sqrt{3}} \approx 0.14434. \tag{4.19}$$

This is consistent with the numerically estimated value (4.11) up to a relative error of

$$\Delta\sigma_{\text{rel}} = 0.01\,\%. \tag{4.20}$$

Finally, we provide an approximate computation of the standard deviation of the autocorrelations depending on the number of drawn samples. To this end, we replace the single-sample standard deviation at any times by (4.19). Thereby, the statistical error reads

$$\sigma_{\text{stat}}(M) \approx \frac{1}{4\sqrt{3M}}. \tag{4.21}$$

In the following subsection we discuss the error resulting from the time discretization and the CFET.

4.1.2 Time-discretization and CFET error

To study the behavior of the time-discretization error, we compute $g^{zz}(t)$ in the strong-field regime and $C = 4.0$ for different step widths

$$\delta t_\nu = 40/J_{\text{Q}} \cdot 2^{-\nu}, \qquad \nu \in \{4, 5, 6, 7, 8, 9, 10, 11, 12, 13\}, \tag{4.22}$$

on the intervall $tJ_{\text{Q}} \in [0, 40]$ by averaging over $M = 4 \cdot 10^5$ mean-field configurations. Our aim is basically to estimate the error between the finite-discretization results and the exact results. However, since we cannot access exact numerical results, we take the most accurate discretization $\nu = 13$ as the reference result. Correspondingly, the error is computed by

$$\Delta Q^2(\nu) = \frac{1}{2^\nu + 1} \sum_{m=0}^{2^\nu} \left(g^{zz}_{(13)}(m\delta t_\nu) - g^{zz}_{(\nu)}(m\delta t_\nu) \right)^2, \qquad \nu < 13. \tag{4.23}$$

This quantity certainly represents the time-discretization error for broad time steps δt_ν. Though, when ν is increased we expect a growing contribution by the statistical error $\sigma(t) := \sigma_{\text{average}}(t)$ because this is also present in the subtraction. Considering this, we replace the averaged autocorrelations by

$$g^{zz}_{(\nu)}(t) = \hat{g}^{zz}_{(\nu)}(t) \pm \sigma(t), \tag{4.24}$$

where we call $\hat{g}^{zz}_{(\nu)}(t)$ the exact autocorrelation from the statistical point of view. Inserting this into (4.23) yields

$$\begin{aligned}\Delta Q^2(\nu) = &\frac{1}{2^\nu+1}\sum_{m=0}^{2^\nu}\Big(\hat{g}^{zz}_{(13)}(m\delta t_\nu) - \hat{g}^{zz}_{(\nu)}(m\delta t_\nu)\Big)^2 \\ &\pm \frac{2}{2^\nu+1}\sum_{m=0}^{2^\nu}\Big(\hat{g}^{zz}_{(13)}(m\delta t_\nu) - \hat{g}^{zz}_{(\nu)}(m\delta t_\nu)\Big)\Big(\sigma_{(13)}(m\delta t_\nu) - \sigma_{(\nu)}(m\delta t_\nu)\Big) \\ &+ \frac{1}{2^\nu+1}\sum_{m=0}^{2^\nu}\Big(\sigma_{(13)}(m\delta t_\nu) - \sigma_{(\nu)}(m\delta t_\nu)\Big)^2.\end{aligned} \tag{4.25}$$

The first sum is the bare time-discretization error adjusted for the statistical error. To simplify the other sums, we assume ergodicity

$$\overline{f(\sigma_\rho)}^{\text{time}} = \overline{f(\sigma(t_0))}^{\text{config}}, \tag{4.26}$$

where on the left-hand-side, we average over time for an arbitrary set of configurations ρ and on the right-hand-side, we average over different sets of configurations at an arbitrary time t_0. By means of this, one finds

$$\pm\frac{1}{2^\nu+1}\sum_{m=0}^{2^\nu}\Big(\hat{g}^{zz}_{(13)}(m\delta t_\nu) - \hat{g}^{zz}_{(\nu)}(m\delta t_\nu)\Big)\Big(\sigma_{(13)}(m\delta t_\nu) - \sigma_{(\nu)}(m\delta t_\nu)\Big) \approx 0, \tag{4.27}$$

where we assumed that $\hat{g}^{zz}(m\delta t_\nu)$ is only weakly varying, and

$$\frac{1}{2^\nu+1}\sum_{m=0}^{2^\nu}\Big(\sigma_{(13)}(m\delta t_\nu) - \sigma_{(\nu)}(m\delta t_\nu)\Big)^2 = \frac{2}{2^\nu+1}\sum_{m=0}^{2^\nu}\sigma^2(m\delta t_\nu) = 2\sigma^2_{\text{stat}}, \tag{4.28}$$

where we used that the statistical errors $\sigma_{(\nu)}(m\delta t_\nu)$ and $\sigma_{(13)}(m\delta t_\nu)$ are uncorrelated. In conclusion, we subtract a constant offset $2\sigma^2_{\text{stat}}$ from $\Delta Q^2(\nu)$ to obtain the cleansed time-discretization error $\Delta\hat{Q}^2(\nu)$.

When finding a simple functional behavior $f(\delta t)$ of the remaining error, we are also able to cleanse the data from the discretization error of $\hat{g}^{zz}_{(13)}$. To this end we estimate its contribution in the remaining error according to

$$\Delta\hat{Q}^2(\nu) = \frac{1}{2^\nu+1}\sum_{m=0}^{2^\nu}\Big(\hat{g}^{zz}_{(13)}(m\delta t_\nu) - \hat{g}^{zz}_{(\nu)}(m\delta t_\nu)\Big)^2 \approx \Big(f(\delta t_{13}) - f(\delta t_\nu)\Big)^2 \tag{4.29a}$$

$$= f(\delta t_\nu)^2\Big(\frac{f(\delta t_{13})}{f(\delta t_\nu)} - 1\Big)^2. \tag{4.29b}$$

There, we neglected the time-dependence of the discretization error in the second step for simplicity. Later we will see that a functional behavior proportional to δt^2 results. Therefore, the bare quadratic time-discretization error is computed through

$$\Delta q^2(\nu) = \big(\Delta Q^2(\nu) - 2\sigma^2_{\text{stat}}\big)\cdot\Big(1 - \frac{1}{2^{2(13-\nu)}}\Big)^2, \tag{4.30}$$

where $\Delta Q^2(\nu)$ is estimated numerically through (4.23) and

$$2\sigma^2_{\text{stat}} \approx 1.041 \cdot 10^{-7}. \tag{4.31}$$

Furthermore, we consider an upper limit for the time-discretization error because the autocorrelation is restricted to $-\frac{1}{4} \leq g^{zz}(t) \leq \frac{1}{4}$. Because we observe a growing of $g^{zz}(t)$ at all times as the time widths δt is increased, we only regard the upper bound for our purpose given by

$$\Delta q^2_{\text{up}} = \frac{1}{2^{13}+1} \sum_{m=0}^{2^{13}} \Big(g^{zz}_{(13)}(m\delta t_{13}) - 0.25 \Big)^2. \tag{4.32}$$

Finally, we present the numerical results in Fig. 4.3. We provide data for the second-order (3.42) and the optimized fourth-order CFET (3.43). For both cases the fourth-order result for $\nu = 13$ is taken to be the reference result. Note that some data points are missing because they got negative by subtracting the statistical error. We conclude that the assumption of ergodicity is a rough approximation, but sufficient enough for this consideration. Since we have an upper limit for Δq^2, certainly the data converge to the corresponding value at broad time steps. However, for a large intervall the data behave linearly. By fitting

$$\log\Big(\Delta q^2_{(N)}(\delta t)\Big) = m_{(N)} \log\big(\delta t J_{\text{Q}}\big) + \log\big(A_{(N)}\big), \tag{4.33a}$$

$$\Delta q^2_{(N)}(\delta t) = A_{(N)} \big(\delta t J_{\text{Q}}\big)^{m_{(N)}} \tag{4.33b}$$

to the selected data points, we obtain

$$m_{(2)} = 3.91 \pm 0.04, \qquad A_{(2)} = 1.0 \pm 0.1, \tag{4.34a}$$

$$m_{(4)} = 4.012 \pm 0.007, \qquad A_{(4)} = 1.08 \pm 0.02, \tag{4.34b}$$

where (N) denotes the CFET order. Concludingly, we have $\Delta q^2 \propto \delta t^4$ and thus $\Delta q \propto \delta t^2$ for both CFETs. Indeed, this is surprising for the fourth-order CFET because its truncation error is of order δt^5. However, approximating the integrals with aid of the Trapez rule according to (3.44) entails an error $\propto \delta t^3$. Through the evaluation of the product of short-step TEOs this error increases to

$$L\delta t^3 = \frac{t}{\delta t}\delta t^3 \propto \delta t^2, \tag{4.35}$$

where L represents the number of time steps before time t. Since we are reliant on the Trapez rule due to the self-consistency problem, this error cannot be reduced. Therefore, the second-order CFET suffices for any applications in this thesis. Nevertheless, we use the optimized fourth-order CFET henceforth because this does not affect the computation time at all, but we access slightly more accuracy according to (4.34). Finally, we formulate a simple rule-of-thumb for the approximate time-discetization error

$$\Delta q(\delta t) \approx \big(\delta t J_{\text{Q}}\big)^2. \tag{4.36}$$

The next section deals with the iteration-error and the covergence of the self-consistency problem.

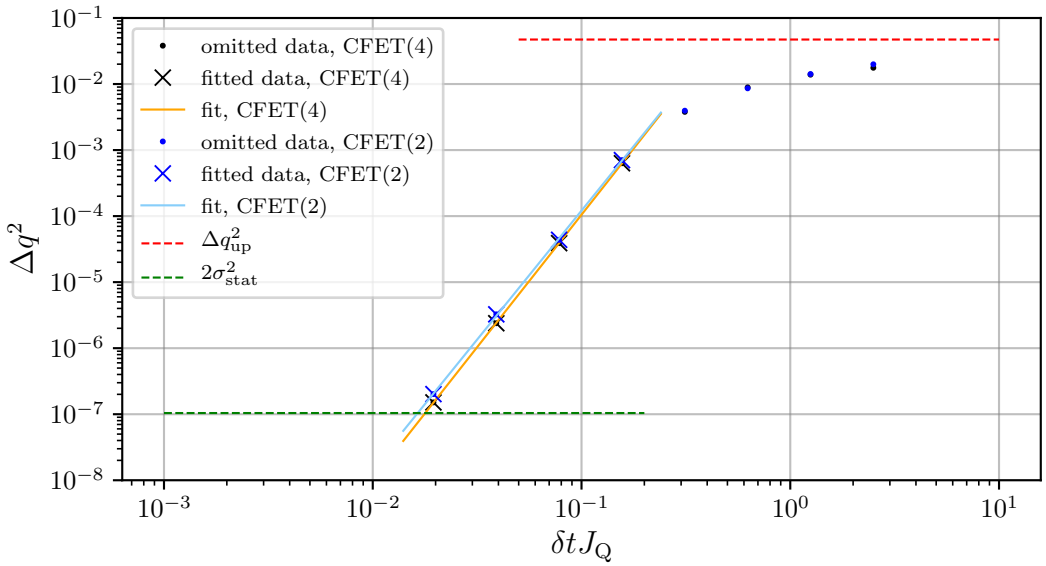

Figure 4.3: Log-log plot of the squared time-discretization error (4.30) vs. the step width δt. Shown are the data for the second-order and the optimized fourth-order CFET. Moreover, fits of the crossed data points according to (4.33) and the parameters (4.34) are plotted. The upper limit is estimated with the help of (4.32) and the statistical error is given by (4.31).

4.1.3 Iteration-error and convergence

The presented algorithm 1 reveals how to solve the self-consistency problem through numerical iteration. Basically, one inserts arbitrary initial autocorrelations and optimizes them during the iteration-steps $(n) \to (n+1)$. After reaching a certain error threshold, the algorithm is stopped and the latest results are adopted. This threshold should be chosen cleverly so that efficiency and reliability of the results is ensured. We define the iteration-error by

$$\Delta I^{\alpha\beta}_{(n+1)} = \frac{1}{L}\sum_{m=1}^{L} |g^{\alpha\beta}_{(n+1)}(m\delta t) - g^{\alpha\beta}_{(n)}(m\delta t)|, \tag{4.37}$$

where (n) denotes the previous and $(n+1)$ the latest result. This error is computed for all non-vanishing autocorrelations and for every $n > 0$ and subsequently compared to a proper error threshold ΔI_{th}. When setting this threshold, one must regard the statistical error of the computation because it limits the accuracy. From our practical experience we recommend

$$\Delta I_{\mathrm{th}} = \frac{3}{2}\sigma_{\mathrm{stat}}(M), \tag{4.38}$$

where $\sigma_{\text{stat}}(M)$ is given by (4.21). When all considered errors exceed ΔI_{th} during an iteration-step, the iteration-error is of the same magnitude as the statistical error. Thus, the accuracy is maximized and the iteration should be stopped.

We provide some results at different iteration-steps and for different initial autocorrelations in order to illustrate the convergence during the iterations. To this end, we consider the strong-field regime including a finite noise $C = 4.0$. Moreover, we draw $M = 4 \cdot 10^5$ samples leading to a threshold of

$$\Delta I_{\text{th}} \approx 0.000\,34, \tag{4.39}$$

and set the step width to $\delta t = 0.02/J_{\text{Q}}$. The computation is repeated for a step width of $\delta t = 0.002/J_{\text{Q}}$ to obtain a higher resolution of $g^{xx}(t)$. In Fig. 4.4 and 4.5 we present results for different sets of initial autocorrelations $v^{\alpha\beta}_{(0)}(t)$ given by

$$f_{\text{Exp}}(t) = \delta_{\alpha\beta}\frac{J_{\text{Q}}^2}{4}\mathrm{e}^{-tJ_{\text{Q}}}, \tag{4.40a}$$

$$f_{\text{Gau}}(t) = \delta_{\alpha\beta}\frac{J_{\text{Q}}^2}{4}\mathrm{e}^{-t^2J_{\text{Q}}^2}, \tag{4.40b}$$

$$f_{\text{Lin}}(t) = \delta_{\alpha\beta}\frac{J_{\text{Q}}^2}{4}. \tag{4.40c}$$

Furthermore, we listed the corresponding iteration-errors in Tab. C.1 and C.2. Fortunately, the convergence occurs very fast in around $4-5$ iteration steps. We compute the errors between the resulting autocorrelations for different initial functions f_i through

$$E^{\alpha\beta}(f_1, f_2) = \frac{1}{L}\sum_{m=1}^{L}|g^{\alpha\beta}_{(f_1)}(m\delta t) - g^{\alpha\beta}_{(f_2)}(m\delta t)|, \tag{4.41}$$

where $g^{\alpha\beta}_{(f_i)}$ is the final autocorrelation corresponding to f_i. This results in

$$E^{xx}(f_{\text{Exp}}, f_{\text{Gau}}) = 0.000\,14, \qquad E^{zz}(f_{\text{Exp}}, f_{\text{Gau}}) = 0.000\,12, \tag{4.42a}$$

$$E^{xx}(f_{\text{Gau}}, f_{\text{Lin}}) = 0.000\,35, \qquad E^{zz}(f_{\text{Gau}}, f_{\text{Lin}}) = 0.000\,39, \tag{4.42b}$$

$$E^{xx}(f_{\text{Lin}}, f_{\text{Exp}}) = 0.000\,33, \qquad E^{zz}(f_{\text{Lin}}, f_{\text{Exp}}) = 0.000\,33, \tag{4.42c}$$

which is of the same magnitude as the statistical error. Therefore, the final autocorrelations are equal up to numerical constraints, indicating that the algorithm is stable.

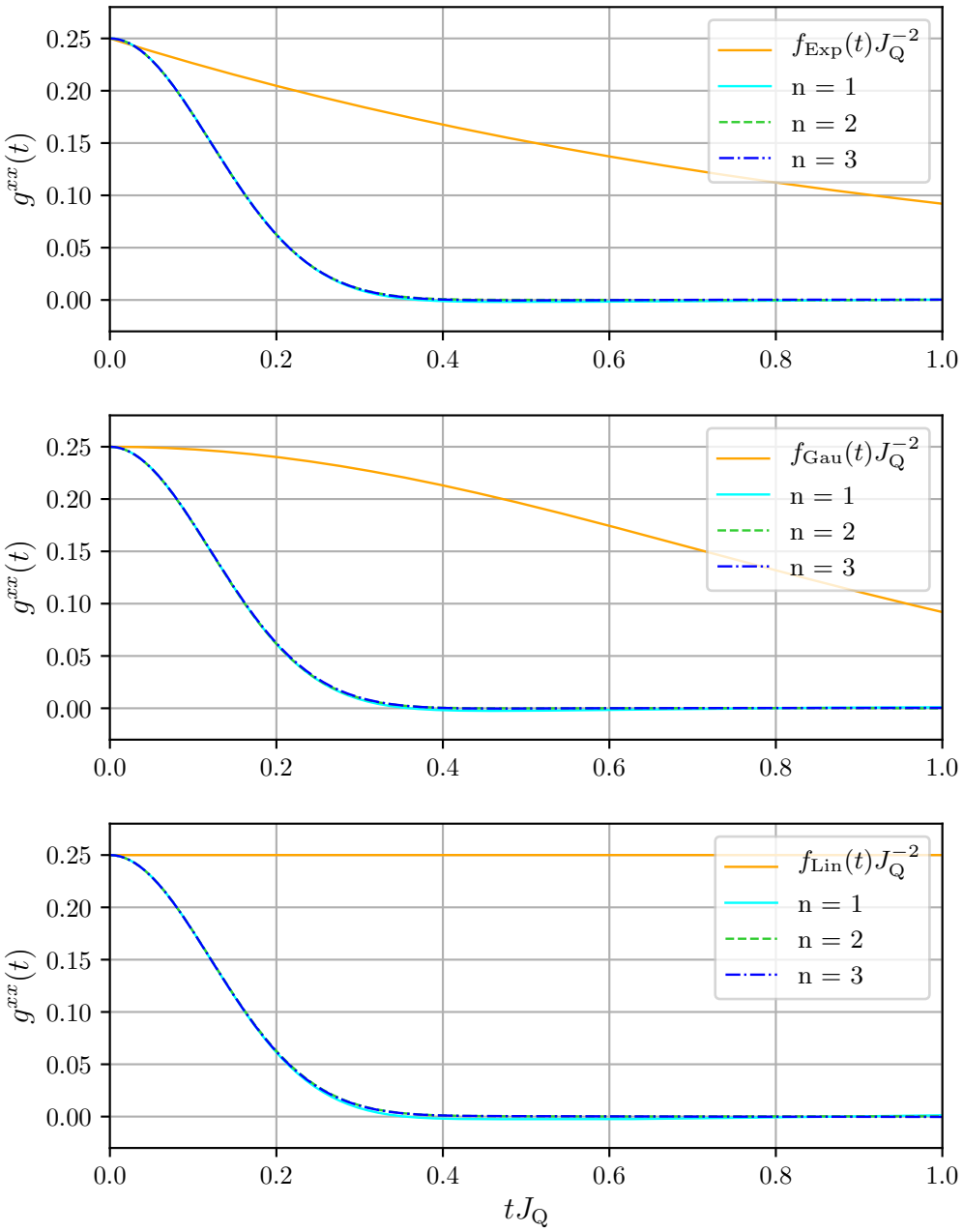

Figure 4.4: Plot of the autocorrelations $g^{xx}(t)$ during the iteration-steps $(n) \to (n+1)$ for different initial functions (4.40) to illustrate the convergence of the self-consistency problem. In each plot the curves for $n = 1, 2, 3$ lie above each other.

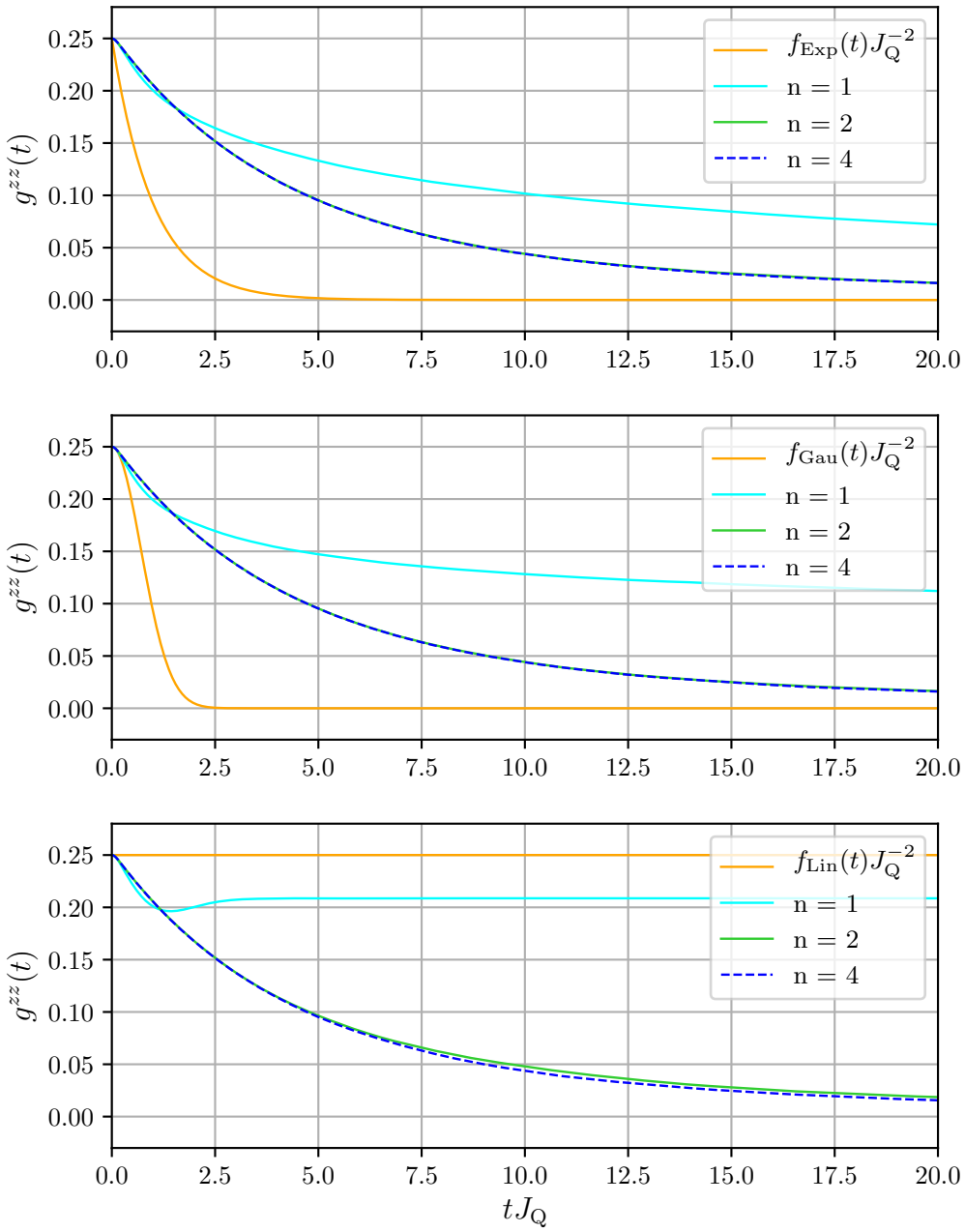

Figure 4.5: Plot of the autocorrelations $g^{zz}(t)$ during the iteration-steps $(n) \to (n+1)$ for different initial functions (4.40) to illustrate the convergence of the self-consistency problem. In each plot the curves for $n = 2, 4$ lie above each other.

4.2 Results in the strong-field regime

In chapter 2 we considered a surface-spin system subjected to a strong static field and a magnetic noise. By means of a RWA and S-DMFT, we derived a mean-field Hamiltonian (2.67) and corresponding self-consistency conditions (2.68). We provided an algorithm to solve this issue numerically through iteration in chapter 3. Based on this, we present and discuss our numerical results in the following.

4.2.1 Zero-noise results

At first, we consider a noise of $C = 0$ and set the numerical parameters to

$$M = 4 \cdot 10^5, \qquad \delta t = 0.01\, J_{\mathrm{Q}}^{-1}. \tag{4.43}$$

Corresponding to the error analysis in Sec. 4.1 the standard deviation of the averaged autocorrelations $g^{\alpha\alpha}(t)$ is around $3 \cdot 10^{-4}$. The results are plotted in Fig. 4.6 and 4.7. We find that $g^{xx}(t)$ decays faster than $g^{zz}(t)$ and by another trend. This difference between the autocorrelations clearly results from the anisotropy in the Hamiltonian (2.67). We fit a Gaussian function

$$f^{xx}(t) = \frac{1}{4}\mathrm{e}^{-\mu t^2} \tag{4.44}$$

to $g^{xx}(t)$ and obtain

$$\mu = (2.528 \pm 0.003)\, J_{\mathrm{Q}}^2. \tag{4.45}$$

The plot in Fig. 4.6 and the small least square error

$$\chi\left(f^{xx}\right) := \frac{1}{L+1}\sum_{m=0}^{L}\Big(f^{xx}(m\delta t) - g^{xx}(m\delta t)\Big) = 2.57 \cdot 10^{-6} \tag{4.46}$$

confirm the Gaussian behavior of $g^{xx}(t)$ very well. Furthermore, we fit two exponential functions

$$f_1^{zz}(t) = \frac{1}{4}\mathrm{e}^{-\nu t}, \tag{4.47a}$$

$$f_2^{zz}(t) = \frac{1}{4}\mathrm{e}^{-\rho\left[\sqrt{t^2+\kappa^2}-|\kappa|\right]} \tag{4.47b}$$

to $g^{zz}(t)$ yielding

$$\nu = (0.697 \pm 0.002)\, J_{\mathrm{Q}}, \qquad \chi\left(f_1^{zz}\right) = 2.31 \cdot 10^{-5}, \tag{4.48a}$$

$$\rho = (0.866 \pm 0.001)\, J_{\mathrm{Q}}, \qquad \chi\left(f_2^{zz}\right) = 7.44 \cdot 10^{-7}, \tag{4.48b}$$

$$\kappa = (0.324 \pm 0.002)\, J_{\mathrm{Q}}^{-1}. \tag{4.48c}$$

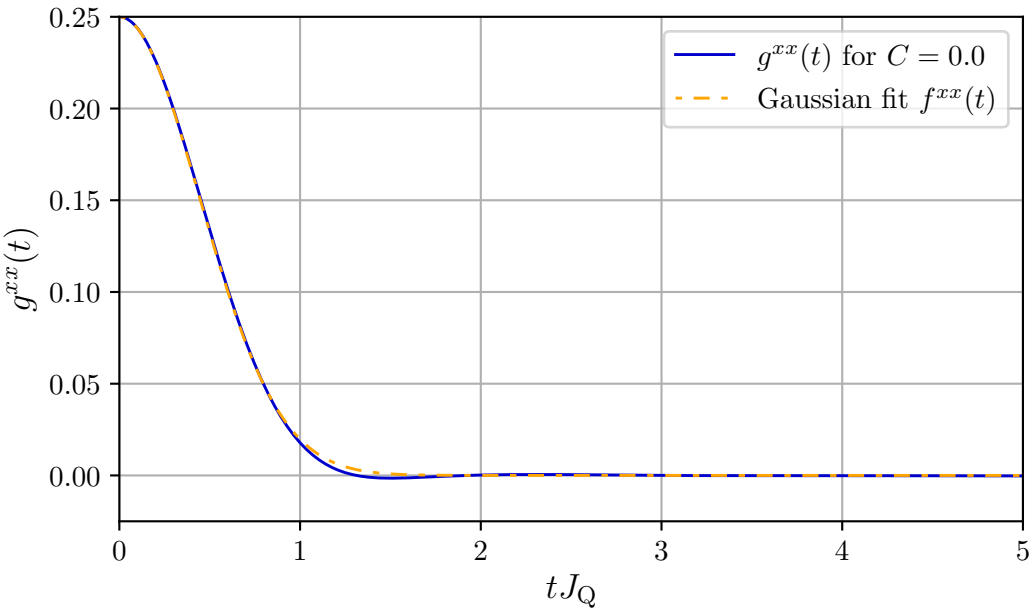

Figure 4.6: Numerically estimated autocorrelation $g^{xx}(t)$ for zero magnetic noise. The parameter of the Gaussian fit (4.44) is presented in (4.45).

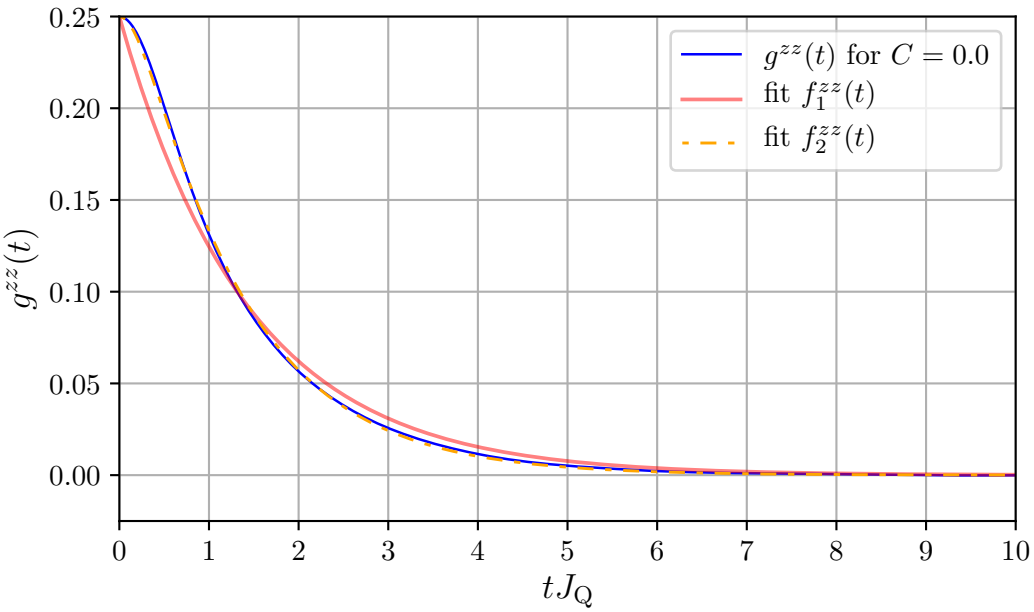

Figure 4.7: Numerically estimated autocorrelation $g^{zz}(t)$ for zero magnetic noise. The parameters of the fit functions (4.47) are presented in (4.48).

Considering this and Fig. 4.7, we deduce that the fit f_2^{zz} works better than the simple exponential function, but since $f_2^{zz}(t)$ converges to $f_1^{zz}(t)$ for $t \to \infty$, the long-time trend of $g^{zz}(t)$ seems to be exponential.

In conclusion, we find a visible difference between transversal and longitudinal decay, though they are not decaying on essentially different timescales as observed experimentally. In the following subsection we present our numerical results for a finite noise. According to the analytical calculation in Sec. 2.4, we expect a growing difference between the autocorrelations.

4.2.2 Finite-noise results

For the numerical evaluation of the finite-noise autocorrelations we choose the same parameters as in (4.43). We repeat some calculations with shorter time steps on a small time intervall in the beginning because the transversal autocorrelation decays essentially faster than the longitudinal one. This is not done to reduce the error of the estimation, but to obtain smoother curves for $g^{xx}(t)$. The resulting autocorrelations $g^{xx}(t)$ and $g^{zz}(t)$ are plotted in Fig. 4.8 and 4.9 for $C = 5.0, 10.0, 50.0$. Analogous to the case of zero noise, we fit a Gaussian function (4.44) to $g^{xx}(t)$ and find

$$C = 1.0: \qquad \mu = (10.71 \pm 0.01)\, J_{\mathrm{Q}}^2, \qquad \chi(f^{xx}) = 9.56 \cdot 10^{-7}, \tag{4.49a}$$

$$C = 5.0: \qquad \mu = (42.65 \pm 0.01)\, J_{\mathrm{Q}}^2, \qquad \chi(f^{xx}) = 5.29 \cdot 10^{-8}, \tag{4.49b}$$

$$C = 50.0: \qquad \mu = (403.9 \pm 0.2)\, J_{\mathrm{Q}}^2, \qquad \chi(f^{xx}) = 5.62 \cdot 10^{-8}. \tag{4.49c}$$

Furthermore, an exponential fit (4.47a) of $g^{zz}(t)$ leads to

$$C = 1.0: \qquad \nu = (0.3300 \pm 0.0006)\, J_{\mathrm{Q}}^2, \qquad \chi(f_1^{zz}) = 1.44 \cdot 10^{-5}, \tag{4.50a}$$

$$C = 5.0: \qquad \nu = (0.1598 \pm 0.0004)\, J_{\mathrm{Q}}^2, \qquad \chi(f_1^{zz}) = 5.52 \cdot 10^{-5}, \tag{4.50b}$$

$$C = 50.0: \qquad \nu = (0.054\,07 \pm 0.000\,06)\, J_{\mathrm{Q}}^2, \qquad \chi(f_1^{zz}) = 2.55 \cdot 10^{-5}. \tag{4.50c}$$

When fitting the second function (4.47b) to $g^{zz}(t)$, κ is forced to zero. Therefore, the second fit approximately equals the first one and we do not discuss it further. Through (2.74c), we predicted a Gaussian function for $g^{xx}(t)$ depending on the exponent

$$\mu_{\mathrm{theo}}(C) = 8C\, J_{\mathrm{Q}}^2. \tag{4.51}$$

Corresponding to this, we compute the relative errors between

$$\mu_{\mathrm{theo}}(C = 1.0) = 8\, J_{\mathrm{Q}}^2, \tag{4.52a}$$

$$\mu_{\mathrm{theo}}(C = 5.0) = 40\, J_{\mathrm{Q}}^2, \tag{4.52b}$$

$$\mu_{\mathrm{theo}}(C = 50.0) = 400\, J_{\mathrm{Q}}^2 \tag{4.52c}$$

and the numerically estimated values (4.49) yielding

$$\Delta_{\mu,\text{theo/num}}(C = 1.0) = 25.3\,\%, \tag{4.53a}$$
$$\Delta_{\mu,\text{theo/num}}(C = 5.0) = 6.21\,\%, \tag{4.53b}$$
$$\Delta_{\mu,\text{theo/num}}(C = 50.0) = 1.0\,\%, \tag{4.53c}$$

which is consistent with the analytical argument because we assumed a large noise and neglected any mean-field contributions. The second analytical statement (2.75) predicted $g^{zz}(t)$ to be constant over time for a large noise. Although this behavior is clearly not visible in Fig. 4.9, $g^{zz}(t)$ decays essentially slower than $g^{xx}(t)$ for large C. Therefore, the longitudinal autocorrelation is approximately constant at timescales of the transversal decay in consistency with the analytical prediction. Moreover, we confirm that the difference between the decay of $g^{xx}(t)$ and $g^{zz}(t)$ is amplified by the presence of a magnetic noise in agreement with the experimental claim [25]. The next step is to study the dependence of C and particularly to quantify the difference between the longitudinal and transversal decay. Subsequently, we compare our results to experimental data and estimate proper values for C and J_Q.

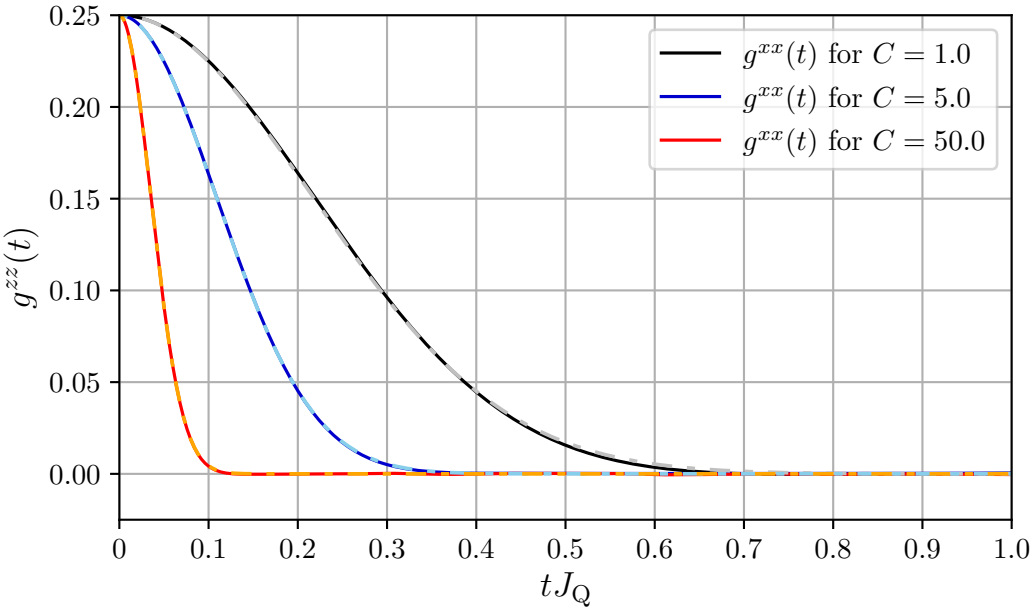

Figure 4.8: Numerically estimated autocorrelations $g^{xx}(t)$ for finite magnetic noises C and corresponding Gaussian fits (dashed lines). The fit parameters according to (4.44) are presented in (4.49).

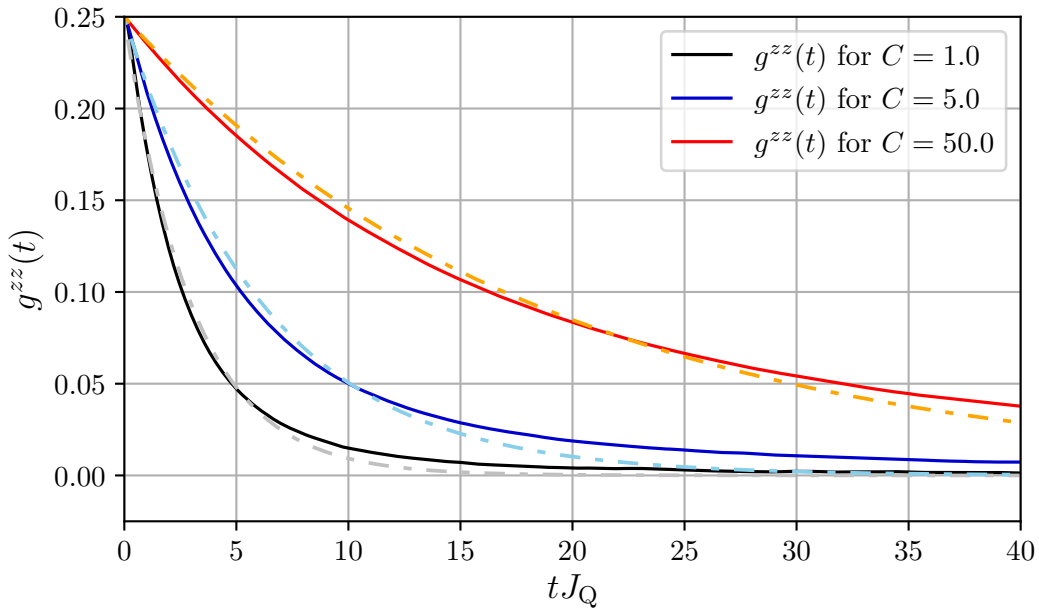

Figure 4.9: Numerically estimated autocorrelations $g^{zz}(t)$ for finite magnetic noises C and corresponding exponential fits (dashed lines). The fit parameters according to (4.47a) are presented in (4.50).

4.2.3 Noise effects

In order to directly compare our numerical results to the experimenal data, at first, we have to determine an optimal value of the phenomenological parameter C, since it affects $g^{xx}(t)$ and $g^{zz}(t)$ by a different manner. To this end, we define the typical decay time $t^{\alpha\alpha}(\xi, C)$ describing the time at which the autocorrelation $g^{\alpha\alpha}(t)$ equals ξ, i.e., the inverse function. We compute the autocorrelations for a proper domain of C and estimate $t^{\alpha\alpha}(\xi, C)$ for fixed $\xi < \frac{1}{4}$. Since the Gaussian fit succeeds for $g^{xx}(t)$, we compute the decay time by means of the fit parameter via

$$t^{xx}(\xi, C) = \sqrt{\frac{1}{\mu(C)} \ln \frac{1}{4\xi}}, \tag{4.54}$$

where $\mu(C)$ refers to (4.44). The decay time for $g^{zz}(t)$ is estimated manually, while determining the two surrounding time steps t_m and t_{m+1} and linearly interpolating $g^{zz}(t)$ on the corresponding intervall

$$l_m(t) = \frac{g^{zz}(t_{m+1}) - g^{zz}(t_m)}{\delta t} (t - t_m) + g^{zz}(t_m). \tag{4.55}$$

Thereby, the decay time yields

$$t^{zz} = t_m + \delta t \frac{\xi - g^{zz}(t_m)}{g^{zz}(t_{m+1}) - g^{zz}(t_m)}. \tag{4.56}$$

In Fig. 4.10 and 4.11 we plotted the the results for $\xi = \frac{1}{4\mathrm{e}}$ and moreover the analytical function

$$T^{xx}_{\mathrm{app}}\left(\xi = \tfrac{1}{4\mathrm{e}}, C\right) J_{\mathrm{Q}} = \sqrt{\frac{1}{8C} \ln \frac{1}{4\xi}} = \sqrt{\frac{1}{8C}} \tag{4.57}$$

because we expect this behavior for a large noise according to (4.51). Considering the fit parameters (4.49) from the previous section we observe that the absolut difference between the predicted value $8C$ and the resulting exponent μ is not varying much. Hence, we fit

$$T^{xx}_{\mathrm{fit}}\left(C\right) J_{\mathrm{Q}} = \sqrt{\frac{1}{8(C+R)}} \tag{4.58}$$

to t^{xx} leading to

$$R = 0.319 \pm 0.001, \qquad \chi\left(T^{xx}_{\mathrm{fit}}\right) = 2.34 \cdot 10^{-6}. \tag{4.59}$$

The corresponding curve is also shown in Fig. 4.10. We notice that $T^{xx}_{\mathrm{app}}(C)$ is different from the data for small C because it diverges at $C = 0$. For large C the function converges to the data as expected, though. By $T^{xx}_{\mathrm{fit}}(C)$ we provide a proper description of the decay time even for small noises. This reveals that the mean-field contributions to the Gaussian exponent of $g^{xx}(t)$ are weakly fluctuating in terms of the noise.

Since we have not found any simple and at the same time suitable fit for $g^{zz}(t)$, an analytically or numerically motivated behavior of t^{zz} is missing at this point. However, as we see later the fraction of the decay times follows a surprisingly strong linear trend. Therefore, we apply a fit of

$$T^{zz}_{\mathrm{fit}}(\xi = \tfrac{1}{4\mathrm{e}}, C) = (pC + w) \cdot T^{xx}_{\mathrm{fit}}(\xi = \tfrac{1}{4\mathrm{e}}, C) = \frac{pC + w}{\sqrt{8(C+R)}} \tag{4.60}$$

to the data, where R is given by (4.59) finding

$$p = 7.058 \pm 0.005, \qquad \chi\left(T^{zz}_{\mathrm{fit}}\right) = 2 \cdot 10^{-4}, \tag{4.61a}$$

$$w = 2.22 \pm 0.01, \tag{4.61b}$$

which turns out to be quite successful, see Fig. 4.11.

The numerical decay times $t^{xx}(\xi)$ and $t^{zz}(\xi)$ cannot be compared to experimental data so far because they are estimated in units of J_{Q}^{-1}. In contrast, the fraction of them

$$F(\xi, C) := \frac{t^{zz}(\xi, C)}{t^{xx}(\xi, C)} \tag{4.62}$$

is clearly unitless and thus forms a suitable parameter to characterize the system. In particular, it measures the discrepancy between the decay of $g^{xx}(t)$ and $g^{zz}(t)$. We provide a plot of $F(\xi, C)$ vs. C at three different ξ in Fig. 4.12. Applying a linear fit

$$F_{\mathrm{fit}}(\xi, C) = p(\xi) \cdot C + w(\xi) \tag{4.63}$$

leads to the parameters

$$\xi = 1/4\sqrt{\mathrm{e}}: \quad p = 4.727 \pm 0.003, \quad w = 1.846 \pm 0.003, \quad \chi\left(F_{\mathrm{fit}}\right) = 0.002, \tag{4.64a}$$
$$\xi = 1/4\mathrm{e}: \quad p = 7.066 \pm 0.006, \quad w = 2.216 \pm 0.006, \quad \chi\left(F_{\mathrm{fit}}\right) = 0.007, \tag{4.64b}$$
$$\xi = 1/4\mathrm{e}^2: \quad p = 11.85 \pm 0.02, \quad w = 2.57 \pm 0.02, \quad \chi\left(F_{\mathrm{fit}}\right) = 0.087. \tag{4.64c}$$

The suitability of the linear fit is remarkable and suggests a physical meaning, e.g., a conserved quantity. We did not investigate this further. In the following, we compare our numerical results for F to the corresponding fraction of the experimental data in order to find a suitable value for J_{Q} and C.

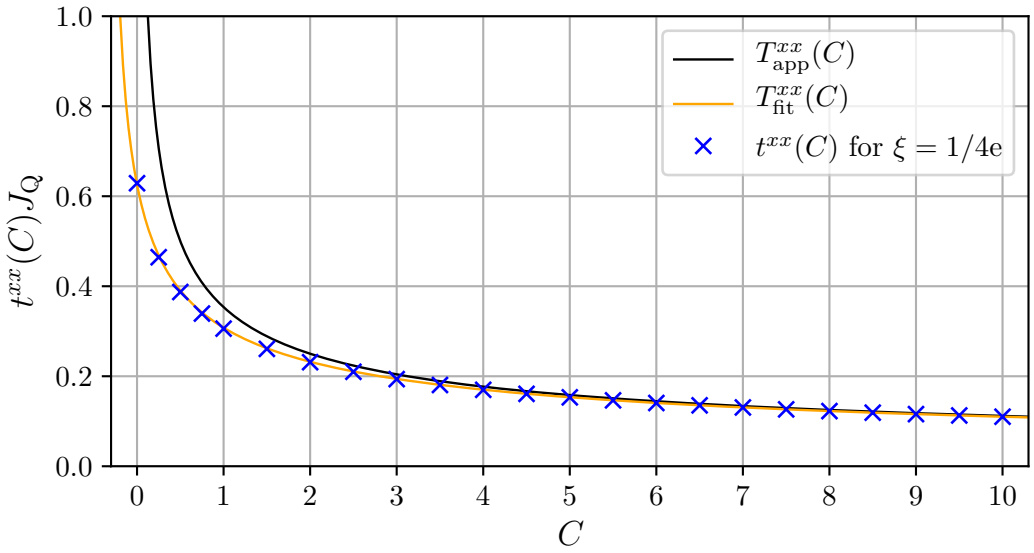

Figure 4.10: Decay time $t^{xx}(\xi, C)$ vs. the noise at $\xi = \frac{1}{4\mathrm{e}}$. In addition we show the analytical approximation (4.57) and a suitable fit function (4.58).

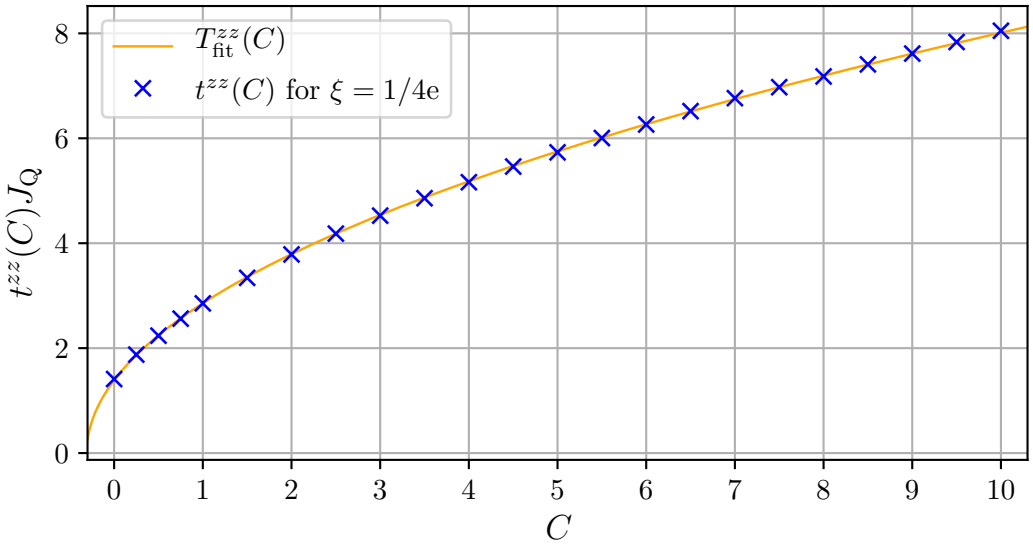

Figure 4.11: Decay time $t^{zz}(\xi, C)$ vs. the noise at $\xi = \frac{1}{4\text{e}}$. The fit function is provided in (4.60).

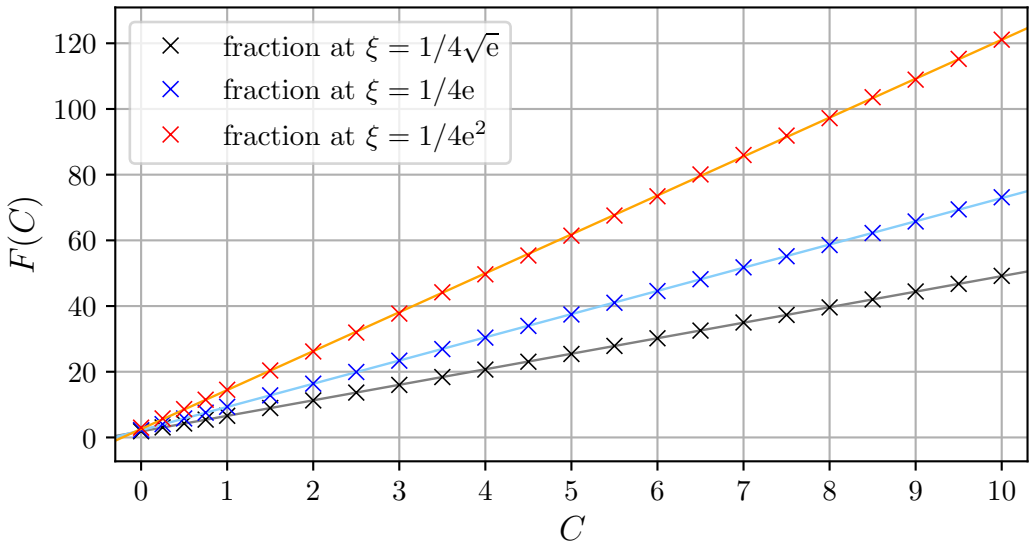

Figure 4.12: Decay-time fraction $F(\xi, C)$ at $\xi = \frac{1}{4\sqrt{\text{e}}}, \frac{1}{4\text{e}}, \frac{1}{4\text{e}^2}$ vs. the noise and linear fit functions. The corresponding fit parameters can be found in (4.64).

4.2.4 Comparison to the experimental results

Fortunately, we received experimental data (not published yet) from the research group of Prof. A. Sushkov (Department of Physics, Boston University, Boston, Massachusetts 02215, USA) [25]. Their measurements for the autocorrelations are listed in Tab. B.1 and B.2 and plotted in Fig. 4.13 and 4.14. Henceforth, we denote numerical (n) and experimental (e) results by an additional index so that they can be distinguished. We fit a Gaussian function

$$q^{xx}(t) = \frac{1}{4}\mathrm{e}^{-ut^2} \tag{4.65}$$

to the data for $g_{\mathrm{e}}^{xx}(t)$ yielding

$$u = (3.3 \pm 0.2)\,\mu\mathrm{s}^{-2}, \tag{4.66}$$

with the error-weighted least square error

$$\chi_{\mathrm{e}}\left(q^{xx}\right) := \frac{1}{Z}\sum_{l=1}^{Z}\frac{g_{\mathrm{e}}^{xx}(\tau_l) - q^{xx}(\tau_l)}{\Delta g_{\mathrm{e}}^{xx}(\tau_l)} = 1.607, \tag{4.67}$$

where $\Delta g_{\mathrm{e}}^{xx}(\tau_l)$ is the standard deviation of the experimental data. We conclude that the data approximately behave Gaussian according to the resulting fit function in Fig. 4.13. Thus, we already find a great agreement between experimental observations and numerics because the Gaussian trend is confirmed for both transversal autocorrelations. We access the desired decay-time fraction through an exponential fit of the longitudinal autocorrelation

$$q^{zz}(t) = \frac{1}{4}\mathrm{e}^{-vt}, \tag{4.68}$$

which results in

$$v = (0.038 \pm 0.003)\,\mu\mathrm{s}^{-1}, \qquad \chi_{\mathrm{e}}\left(q^{zz}\right) = 0.897. \tag{4.69}$$

For an approximate comparison this relative error is acceptable, however, the suitability of the exponential function is rather given at short times as we see in Fig. 4.14. Moreover, a single data point at $t \approx 28\,\mu\mathrm{s}$ deviates strongly from the rest and shifts the fit downwards. Therefore, we apply another exponential fit to some selected data, which are drawn in red in Tab. B.2 and Fig. 4.14, while obtaining

$$v = (0.035 \pm 0.002)\,\mu\mathrm{s}^{-1}, \qquad \chi_{\mathrm{e}}\left(q^{zz}\right) = 0.407. \tag{4.70}$$

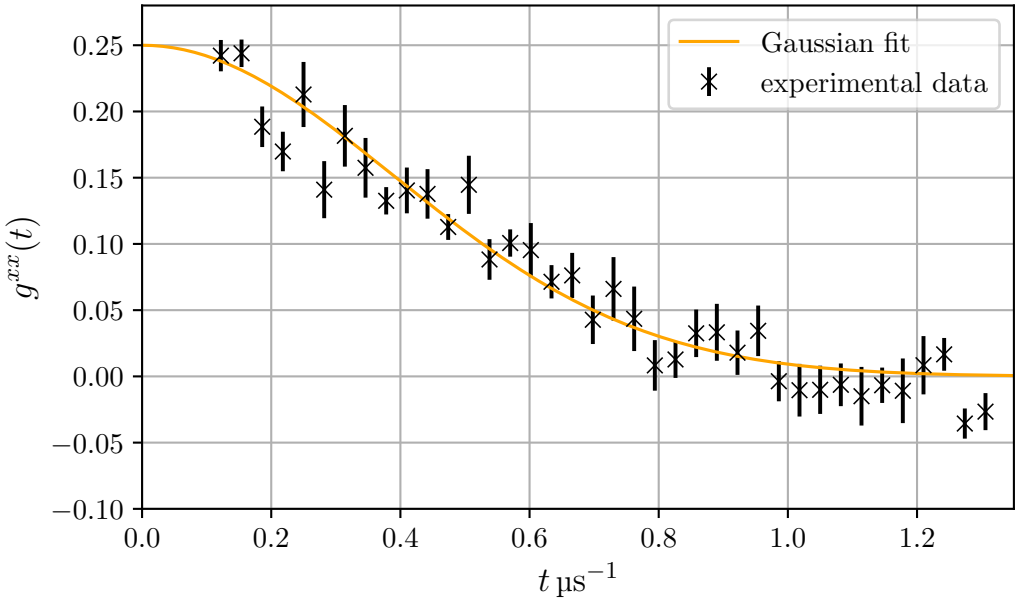

Figure 4.13: Plot of the experimental data of the transversal autocorrelation [25]. The parameter of the Gaussian fit (4.65) is given by (4.66).

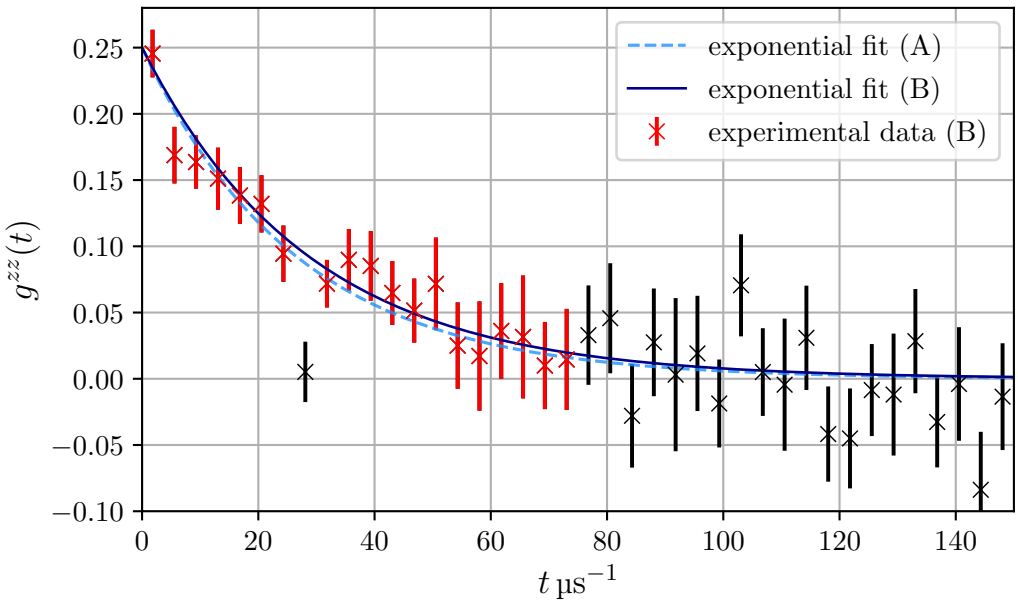

Figure 4.14: Plot of the experimental data of the transversal autocorrelation [25]. The parameter of the exponential fit (4.68) is given by (4.69) for all data (A) and by (4.69) for the selected data (B).

By means of the fit parameters (4.66) and (4.70), we are now able to compute the fraction

$$F_{\text{exp}}(\xi) = \frac{t^{zz}(\xi)}{t^{xx}(\xi)} = \frac{\sqrt{u}}{v}\sqrt{\ln\frac{1}{4\xi}}, \tag{4.71}$$

and thus an optimal value $C(\xi)$, while demanding equality of $F_{\text{exp}}(\xi)$ and $F(\xi, C)$.

Assuming an accurate agreement between theory and experiment one would find a single optimal C independent of ξ. However, because several numerical issues, e.g., the fitting of $g^{zz}(t)$ hamper the comparison, a slight depending on ξ is expected. We provide our results for the optimal noise $C_{\text{opt}}(\xi)$ in Fig. 4.15. For $\xi \to \frac{1}{4}$ we observe that the optimal value decreases abrupt. This is not surprising because both nominator and denominator of the fractions F tend to zero. Hence, the computation gets instable and susceptible to small differences between numerical data, experimental data and especially the applied fits. Furthermore, by reducing ξ we find a weak decreasing of C_{opt}. This is again unproblematic because the suitability of the exponential fit is questionable for large times. Finally, on a large intervall for ξ we find a plateau. Therefore, we estimate the true optimal value of the noise to be somewhere around $C_{\text{opt}} = 6 - 8$. In the following, we try to determine it with more accuracy.

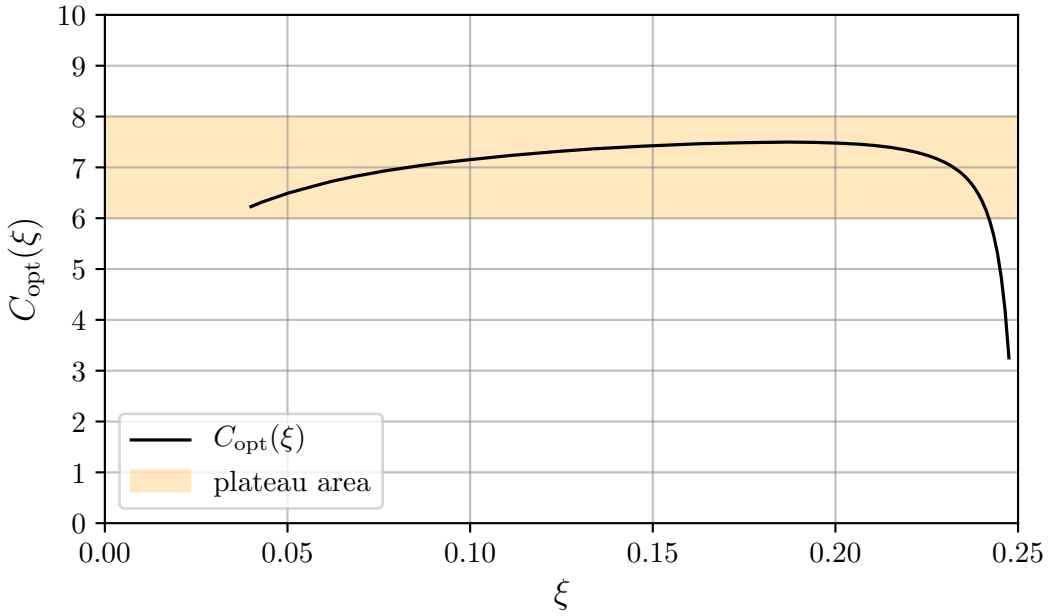

Figure 4.15: Optimal value of the noise vs. the considered decay ξ.

Since the fluctuations of the experimental data and the applied fits are considerable error sources, we are clearly limited in accuracy. Therefore, we do not use any sophisticated algorithm to determine the best matching between numerics and experiment. Instead, we

simply compute the autocorrelations on a finer discretization on the estimated intervall for C. Subsequently, we determine an optimal energy or timescale, respectively, through minimizing the square error between the numerical and experimental data

$$\chi^{xx} = \frac{1}{Z}\sum_{l=1}^{Z}\frac{g_{\mathrm{n}}^{xx}(\tau_i) - g_{\mathrm{e}}^{xx}(\tau_i)}{\Delta g_{\mathrm{e}}^{xx}(\tau_l)}. \tag{4.72}$$

There, τ_i are the time steps of the experimental data in µs, Z is the total number of time steps and $\Delta g_{\mathrm{e}}^{xx}(\tau_i)$ the standard deviation of $g_{\mathrm{e}}^{xx}(\tau_i)$. We remind the reader that τ_i has to be converted to $1/J_{\mathrm{Q}}$ before it can be inserted to $g^{\alpha\alpha}(\tau_i)$. Because the (converted) numerical time domain is different from the experimental one, we linearly interpolate the numerical data to find the required $g^{xx}(\tau_i)$. The coupling constants J_{Q}, minimized errors χ^{xx}, Gaussian fit parameters μ, resulting root-mean-squared (RMS) magnetic fields

$$B_{\mathrm{N}} := \sqrt{\overline{b^2}^{\mathrm{N}}} = \frac{4J_{\mathrm{Q}}\sqrt{C}}{\gamma_{\mathrm{s}}} = \frac{2J_{\mathrm{Q}}\sqrt{C}}{\mu_{\mathrm{B}}}, \tag{4.73}$$

and the resulting average minimum dipole distances

$$r_{\min} = \left(\frac{\mu_0\mu_{\mathrm{B}}^2}{8J_{\mathrm{Q}}\sqrt{\pi}}\right)^{\frac{1}{3}} \tag{4.74}$$

are listed in Tab. C.3 depending on C. Furthermore, we plotted J_{Q} in terms of the noise in Fig. 4.16. On the considered interval for C the dependency is roughly linear. Therefore, we apply a fit

$$J_{\mathrm{lin}}(C) = m_J C + n_J \tag{4.75}$$

yielding

$$m_J = -0.0165 \pm 0.0003, \qquad \chi\left(J_{\mathrm{lin}}\right) = 7.23 \cdot 10^{-7}, \tag{4.76a}$$

$$n_J = 0.357 \pm 0.002. \tag{4.76b}$$

Now that J_{Q} and C are somehow fixed, we are able to directly compare the corresponding autocorrelation $g_{\mathrm{n}}^{zz}(t)$ to the experimental results $g_{\mathrm{e}}^{zz}(\tau)$. Analogous to (4.72), we compute the square error χ^{zz}. We calculate this for all given experimental data (A) and a selected couple of experimental data (B), which are drawn red in Tab. B.2. The resulting errors $\chi^{zz}(C)$ are listed in Tab. C.4. From this, we find a minimum at $C = 6.0$ (A) and $C = 6.8$ (B). The corresponding results for these values are shown in Fig. 4.17 and 4.18 together with the experimental data. According to the plot and the weakly varying errors, the numerically estimated transversal autocorrelations $g_{\mathrm{n}}^{xx}(t)$ are almost equal. This is not surprising because the rescaling shifts the Gaussian results above each other. In contrast, the numerical results for $g_{\mathrm{n}}^{zz}(t)$ are visibly different due to the rescaling.

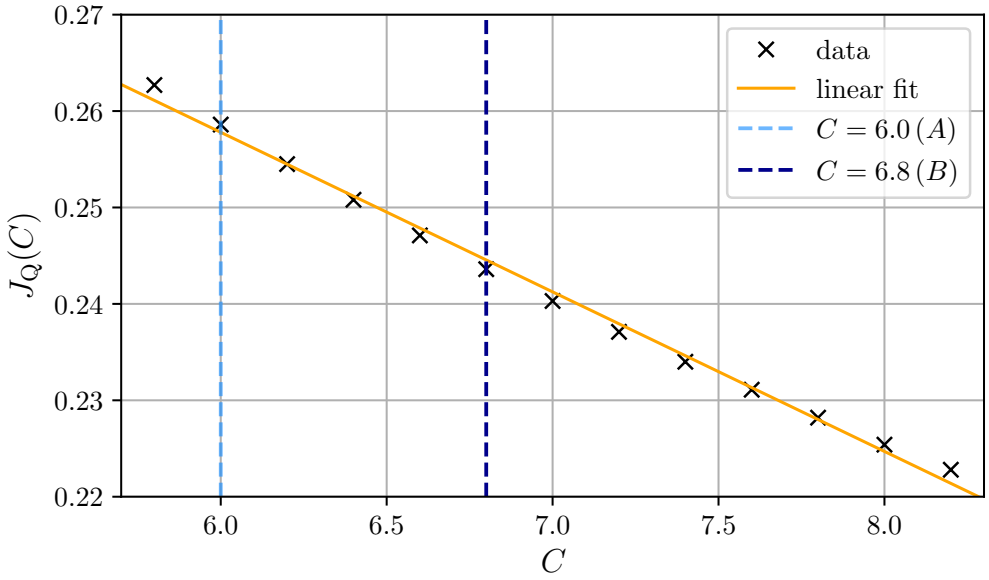

Figure 4.16: Coupling constant J_Q in dependence of the noise parameter C. The parameters of the linear fit (4.75) are shown in (4.76).

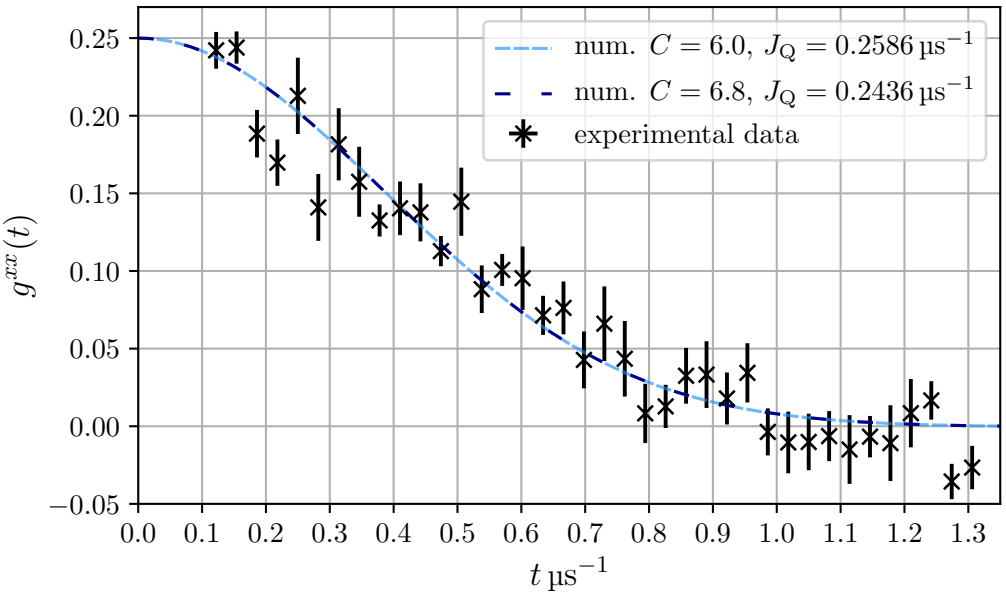

Figure 4.17: Plot of the numerical data for $C = 6.0$ (A) and $C = 6.8$ (B) including the experimental data of the transversal autocorrelation from Ref. [25]. The timescale is estimated from a fit of the numerical results to the experimental data for each C, see Tab. C.3.

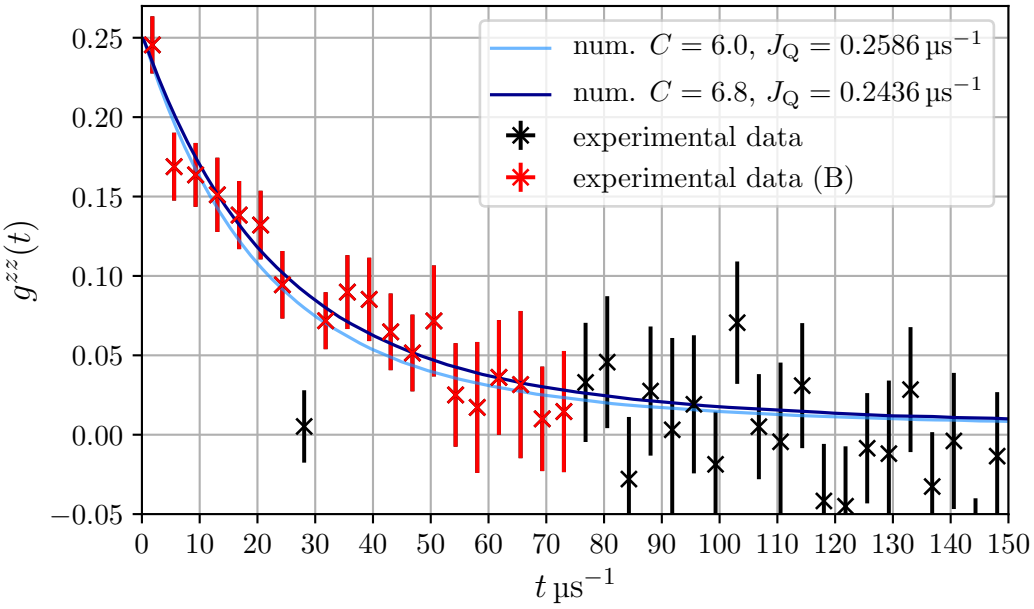

Figure 4.18: Plot of the numerical data for $C = 6.0$ (A) and $C = 6.8$ (B) including the experimental data of the longitudinal autocorrelation from Ref. [25]. The timescale is fixed through a fit of the transversal autocorrelation for each C, see Tab. C.3. The square error between experiment and numerics for $g^{zz}(t)$ is listed in Tab. C.4 for each C.

At short times, the accordance between $g_n^{zz}(t)$ and $g_e^{zz}(t)$ for $C = 6.8$ is great and better than for $C = 6.0$. At long times one hardly finds a statement, though, because the experimental data are fluctuating strongly and moreover fall slightly below zero on average, which is neither expected due to decoherence nor captured by numerics. According to these conclusions, we finally agree on

$$C = 6.8 \pm 0.8, \qquad J_Q = (0.24 \pm 0.01)\,\mu s^{-1} \tag{4.77}$$

to be realistic values characterizing magnetic noise and energy scale. The corresponding RMS field reads

$$B_N = (14.52 \pm 0.07)\,\mu s, \tag{4.78}$$

while the average minimum dipole distance yields

$$r_{min} = (6.66 \pm 0.12)\,nm. \tag{4.79}$$

From the experimental measurements we adopt a typical distance of roughly (5 ± 1) nm [25] leading to a relative error of

$$\Delta_r = 25\,\% \tag{4.80}$$

between experimental and numerical value. Although this result is acceptable, we briefly discuss some error sources that could be responsible for this.

At first, one clearly has to mention the neglect of local inhomogeneities and S-DMFT as relevant error sources. Those approximations are indeed fundamentally for this thesis and their errors cannot be quantified easily. The computation of coupling constants through applying the continuum limit forms another error source during the modelling. We emphasize that the value of $r_{\min}$ is directly affected, since its relation to J_{Q} follows from this. Other error sources occur in connection with the magnetic noise induced by shallow proton spins. The assumption that the noise obeys the same variance $\overline{b^2}$ at each site is not fully justified because in experiment the distance between the surface spins and nearby proton spins varies slightly from site to site [25]. Therefore, the effective magnetic field at each surface spin also varies leading to a site-dependent variance $\overline{b_i^2}$.

In summary, the numerical results are in great agreement with the experimental data. By comparing the computed typical distance to the corresponding experimental observation we demonstrated consistency up to an acceptable deviation. The following section deals with the zero-field limit, where the magnetic noise contributes to all spatial dimensions contrary to the strong-field regime.

4.3 Results in the zero-field limit

In Sec. 2.6 we considered the surface-spin system in the zero-field limit while including an isotropic magnetic noise. By means of S-DMFT, we derived self-consistency conditions (2.111) with respect to the Hamiltonian (2.98). A brief symmetry discussion revealed that any autocorrelations $g^{\alpha\beta}(t)$ or $v^{\alpha\beta}(t)$ with $\alpha \neq \beta$ are zero again so that we only consider a longitudinal and transversal decay. We present our numerical results in the following.

4.3.1 Zero-noise results

We set the numerical parameters to

$$M = 4 \cdot 10^5, \qquad \delta t = 0.01\, J_{\parallel}^{-1} = \frac{1}{4\sqrt{2}} 0.01\, J_{\mathrm{Q}}^{-1}, \tag{4.81}$$

leading to a standard deviation of roughly $2 \cdot 10^{-4}$ due to the statistics. The analysis of the time discretization error in Sec. 4.1.2 referred to the strong-field regime and is therefore not reliably applicable here. We rechecked that the time discretization error for this choice of δt does not exceed the magnitude of the statistical error. The resulting autocorrelations for $C_{\mathrm{ZF}} = 0$ are shown in Fig. 4.19. In contrast to the strong-field results for $C = 0$, the longitudinal autocorrelation decays faster than the transversal autocorrelation. This is not surprising because the prefactor $\frac{5}{2}$ in front of $g^{xx}(t)$ in the first self-consistency condition (2.111a) clearly strengthens the transversal autocorrelation. In the strong-field regime, it is not the self-consistency problem but the Hamiltonian (2.67) containing the distorting

prefactors in front of the longitudinal and transversal contibutions implying anisotropy. Transferring those factors to the self-consistency problem would lead to an amplifying factor of 4 concerning $g^{zz}(t)$ relative to $g^{xx}(t)$. The difference between the decays is therefore even stronger than in the zero-field limit as can be seen in the corresponding plots in Fig. 4.6 and 4.7.

We apply Gaussian fits to the autocorrelations according to

$$G^{\alpha\alpha}(t) = \frac{1}{4} \mathrm{e}^{-\mu^{\alpha\alpha} t^2}, \tag{4.82}$$

which result in

$$\mu^{xx} = (0.333 \pm 0.002)\, J_{\parallel}^2 = (10.66 \pm 0.06)\, J_{\mathrm{Q}}^2, \qquad \chi(G^{xx}) = 5.75 \cdot 10^{-5}, \tag{4.83a}$$

$$\mu^{zz} = (0.686 \pm 0.004)\, J_{\parallel}^2 = (22.0 \pm 0.1)\, J_{\mathrm{Q}}^2, \qquad \chi(G^{zz}) = 3.12 \cdot 10^{-5}. \tag{4.83b}$$

By comparing the fit parameters to (4.45) we find that $g^{xx}(t)$ and $g^{zz}(t)$ both decay faster in the zero-field limit due to the increased energy scale $J_{\parallel} = 4\sqrt{2} J_{\mathrm{Q}}$. In the following section we include a finite noise in our numerical computation.

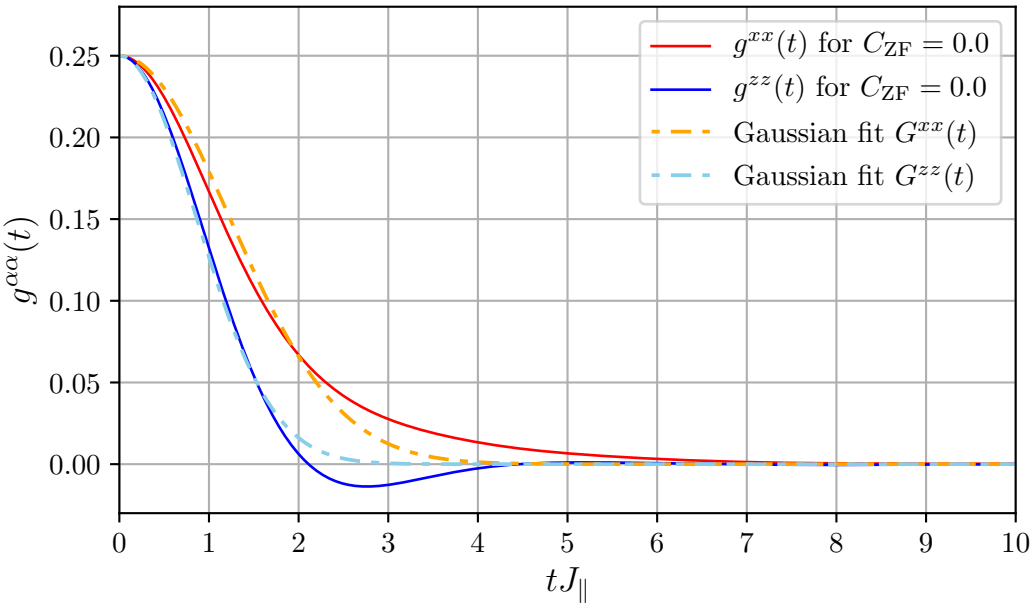

Figure 4.19: Numerically estimated transversal and longitudinal autocorrelation in the zero-field limit and for zero magnetic noise. The parameters of the Gaussian fits are listed in (4.83).

4.3.2 Finite-noise results

The numerical parameters are set as in (4.81). In Sec. 2.6 we introduced the noise parameter C_{ZF} required in the zero-field limit. It is related to the noise in the strong-field

regime through $C_{\mathrm{ZF}} = \frac{C}{2}$ at the magic angle. By means of this, we assume a value of $C_{\mathrm{ZF}} = 3.4$ to be realistic according to the result of the strong-field consideration (4.77). Before discussing the numerical results for this C_{ZF}, at first we consider the case of a large noise to check consistency with the analytical prediction made at the end of Sec. 2.6.

We provide numerical results for $C_{\mathrm{ZF}} = 25.0, 100.0$ in Fig. 4.20. Apparently, both autocorrelations are very similar to each other, which is again contrary to the strong-field regime. Actually, this result is not astonishing because the magnetic noise is appearing in both self-consistency conditions with the same strength so that both autocorrelations are affected by it in a similar way. For large C_{ZF} the mean-field contributions get subdominant leading to an isotropic self-consistency problem and thus to $g^{xx}(t) \approx g^{zz}(t)$. In addition to the numerical results, we also show the analytical prediction from (2.116) in Fig. 4.20. The numerics clearly confirm the predicted trend $g^{\alpha\alpha}_{\mathrm{app}}(t)$ for large C_{ZF}. We observe small deviations in the position of the dip and some weak decay in the numerical results, which is caused by the remaining mean-field contributions. Those were simply neglected against the noise in the analytical consideration.

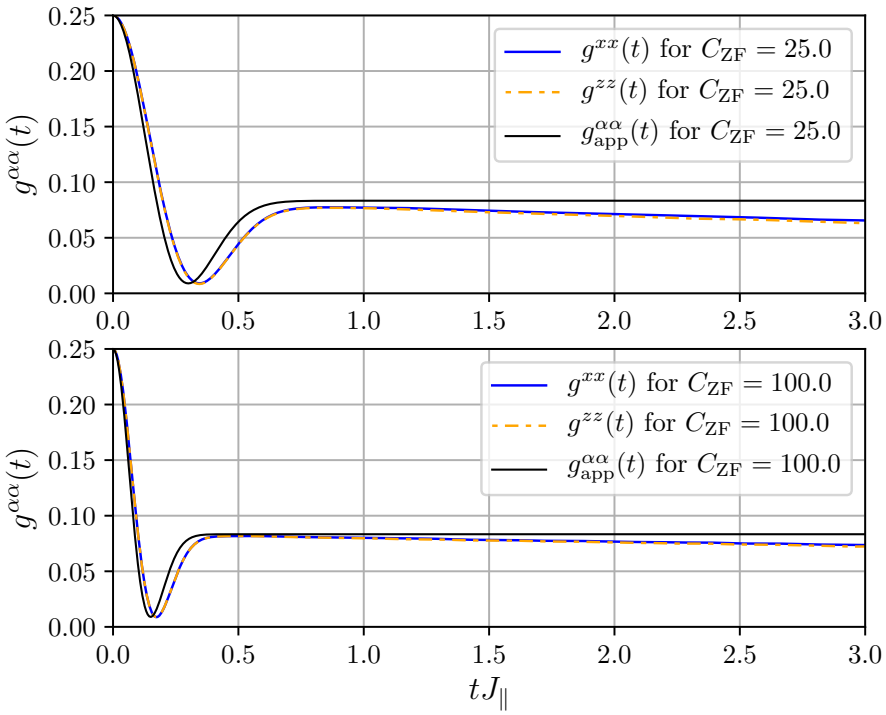

Figure 4.20: Numerically estimated autocorrelations for two large values of C_{ZF}. The analytical prediction $g^{\alpha\alpha}_{\mathrm{app}}(t)$ is given by (2.116).

In Fig. 4.21 we finally present our results for a value of $C_{\mathrm{ZF}} = 3.4$. Both autocorrelations are still very similar to each other due to the dominant contributions from the noise. Since we found a nice accordance between prediction and numerics apart from the weak decay

at long times, we assume that a product of the analytical function with an exponential decay properly reflects the results. Correspondingly, we fit

$$Q^{\alpha\alpha}(t) = g^{\alpha\alpha}_{\mathrm{app}}(t)\mathrm{e}^{-\nu^{\alpha\alpha}t} = \frac{1}{12}\left(1 + 2\left(1 - 2t^2 J_\parallel^2 C_{\mathrm{ZF}}\right)\mathrm{e}^{-t^2 J_\parallel^2 C_{\mathrm{ZF}}}\right)\mathrm{e}^{-\nu^{\alpha\alpha}t} \tag{4.84}$$

to both autocorrelations, which results in

$$\nu^{xx} = (0.203 \pm 0.002)\, J_\parallel, \qquad \chi\left(Q^{xx}\right) = 3.91 \cdot 10^{-5}, \tag{4.85a}$$

$$\nu^{zz} = (0.232 \pm 0.002)\, J_\parallel, \qquad \chi\left(Q^{zz}\right) = 3.06 \cdot 10^{-5}. \tag{4.85b}$$

Overall, the applied fits work out well, see Fig. 4.21. Although there are some deviations at the dip, we find a very nice agreement at longer times. Since $g^{\alpha\alpha}_{\mathrm{app}}(t)$ fastly converges to a constant value, the long-time decay is dominated by the exponential function.

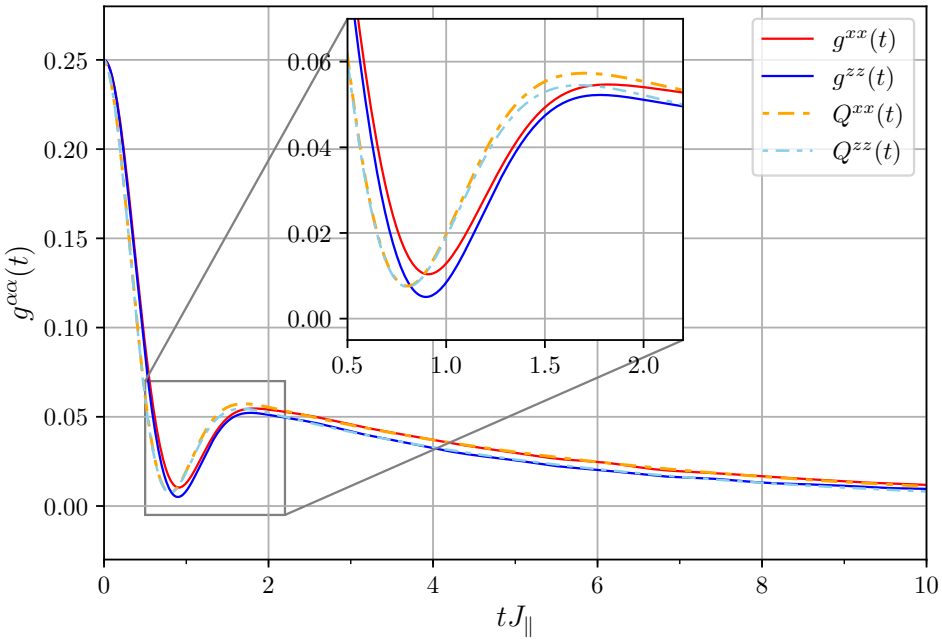

Figure 4.21: Numerically estimated transversal and longitudinal autocorrelation in the zero-field limit for $C_{\mathrm{ZF}} = 3.4$. The parameters of the fit functions (4.84) are given by (4.85).

In summary, the zero-field autocorrelations essentially differ from the strong-field autocorrelations. For zero noise this difference basically results from prefactors in the self-consistency conditions causing various mean-field anisotropies in both cases. Considering a finite magnetic noise in the strong-field regime increases the anisotropy because the noise only contributes in z-direction, as the RWA eliminates its transversal components. In contrast to this, a finite noise in the zero-field limit leads to rather similar autocorrelations

because the isotropic noise reduces the mean-field anisotropy. The final results in Fig. 4.21 are characterized by a dip in the beginning followed by an exponential decay. At short times this trend is similar to that of an isolated spin in a static magnetic noise, which is also relevant in the frozen-fluctuations CSM, see Refs. [8, 38].

5 Summary and outlook

The purpose of this theoretical thesis was to establish S-DMFT, while employing it to a system of dipolar surface spins. From the experimental point of view, the topic is motivated by the observation that the considered surface spins affect shallow NV centers in diamond leading to their decoherence. Due to this issue, it is certainly of interest to gain a detailed insight into the surface-spin dynamics and in particular to the spin autocorrelations. From the theoretical point of view, we established a model which is capable of dealing with large disordered spin ensembles by limited numerical effort.

In chapter 2, we started with setting up the Hamiltonian for a system of dipolar spins that are randomly distributed on a planar surface. On the basis of an experimental setup in Ref. [25], we considered two extensions to the Hamiltonian: First, the experimentalists applied a strong static magnetic field to the system and measured their autocorrelations in the induced Larmor rotating frame. Second, the surface spins are affected by a magnetic field noise resulting from proton spins near the surface. To regard this in theory, we added the corresponding Zeeman-terms to the Hamiltonian, turned to the Larmor rotating frame, and averaged the Hamiltonian over time with aid of the RWA. In the resulting effective Hamiltonian only the z-component of the noise survived.

Subsequently, the effective Hamiltonian was prepared for S-DMFT, while introducing local Overhauser fields representing the environment of each spin. We neglected any local inhomogeneities and thus assumed equality of these fields on average. Then, we established S-DMFT in three fundamental steps: At first, we justifed that the local Overhauser field of a particular spin can be replaced by an unsettled time-dependent mean-field. In the second step we replaced the local Overhauser field by a Gaussian random mean-field with zero average, reasoned through the central limit theorem. Third, we determined the second moments, while deriving self-consistency conditions connecting mean-field autocorrelations to single-spin autocorrelations. Through exploiting symmetries of the system, it was shown that only the transversal and the longitudinal autocorrelations are non-zero. Furthermore, we elaborated that the magnetic noise is simply reduced to a constant offset in the longitudinal condition.

After establishing S-DMFT for the system in the strong-field regime, we were also able to employ it to the system in the zero-field limit. In doing so, we derived a similar self-consistency problem, but with a magnetic noise contributing to both the longitudinal and transversal conditions. In summary, S-DMFT provides a substantially simplified Hamiltonian capturing the affect of a Gaussian mean-field on a single spin. The properties of this field are self-consistently connected to the dynamics of the single spin.

The subsequent chapter treated the numerical implementation of the remaining issue. We furnished an algorithm to solve the self-consistency problem through iteration and

expounded two crucial steps in detail: the sampling of a Gaussian random field and the computation of TEOs via CFETs. Throughout the presented procedure, three numerical error sources occur, which were examined in the beginning of chapter 4. There, we formulated simple rules-of-thumb for an efficient and reliable choice of the number of drawn samples, the time-step width and the iteration-error threshold. Moreover, we demonstrated fast convergence of the estimated autocorrelations during the iterations.

Thereby, we were finally able to compute the desired autocorrelations depending on the magnetic noise strength. In general, we found that the presence of the noise considerably influences the dynamics. When omitting it in the strong-field consideration, we observe that the longitudinal decay happens slower than the transversal decay. By switching it on, this difference is increased because the noise only contributes to the z-direction so that the initial anisotropy is amplified. As a result, the transversal autocorrelation accurately follows a fast-decaying Gaussian trend, while the longitudinal decay is slowed down enormously behaving roughly exponential. From our theoretical perspective, we can clearly agree on the experimental claim that the noise is mainly responsible for the essential difference in the timescales. In our numerical estimation, this difference is easily adjustable through varying the variance of the noise. By means of this, we were able to determine an optimal value for the coupling constant and the noise variance, while comparing our numerics to the experimental data from Ref. [25]. With respect to the fixed parameters, the numerical results are in a great accordance with the received data and therefore confirm the observed slowdown of the longitudinal dynamics.

With aid of the continuum limit, we estimated the average minimum dipole distance from the obtained coupling constant. By doing so, the experimentally observed value $\propto 5\,\mathrm{nm}$ [25] was slightly overestimated. As possible reasons for this deviation we named various error sources, such as the neglect of local inhomogeneities, the usage of the continuum limit, or the assumption of a site-independent noise variance. In future considerations one could actually try to extend the system to a slight local variance of the magnetic noise variance to get even closer to the experiment. Thereby, we expect the single-spin autocorrelations to smear into a set of functions each depending on the local noise variance.

In the zero-field limit we obtain a vastly different behavior of the autocorrelations. In fact, the transversal decay is slowed down relative to the longitudinal decay when the magnetic noise is switched off. Through the presence of a magnetic noise, this anisotropy is mitigated because the noise contributes to both autocorrelations in the same way contrary to the strong-field regime. For a realistic value of it, we finally obtained two similar autocorrelations passing a dip in the beginning followed by an exponential decay. As an outlook, one could also consider the system in the case of an arbitrary aligned weak field, where the RWA is not applicable. Thereby, we expect several originally present symmetries to vanish so that the crossing autocorrelations are non-zero. Due to this the numerical effort of the sampling is increased, though the procedure is not substantially more complex as can be seen in Sec. 3.2.

According to the remarkable agreement between the numerical curves for the fixed parameters and the experimental data, we conclude that S-DMFT worked very well in the strong-field regime. Moreover, we assume the results for other noise variances and

those in the zero-field limit to be valid as well, although we have no experimental data or results from other approaches for comparison. In Sec. 2.3.2 we expounded that the general applicability of S-DMFT highly depends on the topology of the system: while the classical substitution is hardly justified for the CSM, the full approach appears to be working for the two-dimensional dipole-dipole model, although mean-field approaches are known to rather succeed in high dimensions. Beside this, we also expect the applicability to be dependent on the interaction range because the substitution of the local Overhauser field by a Gaussian mean-field is rather justified in the case of a long-range interaction.

From our point of view, a powerful advantage of S-DMFT is not only the low numerical effort but also that the approach is easily expandable, as we experienced in this work. In this sense, another outlook could be to consider externally applied pulses to the spin system confirming or predicting further experimental observations.

A Correlations in spin models on Bethe lattices at infinite temperature

Our goal is to find an analytical argument supporting the assumption that pair-correlations are subdominant in our disordered spin system. To do so, we consider a simplified model describing spin-$\frac{1}{2}$ on a Bethe lattice [44] with a nearest-neighbor coupling at infinite temperature. We try to determine the scaling of the two-time correlation functions $g_{k0}^{\rho\gamma}(t)$, $k \neq 0$, with regard to the coordination number z denoting the number of nearest neighbors. The Bethe lattice is fully determined by z and the fact that it is loop-free [44]. In Fig. A.1 we show a cutout of it with $z = 3$ and with $z = 4$.

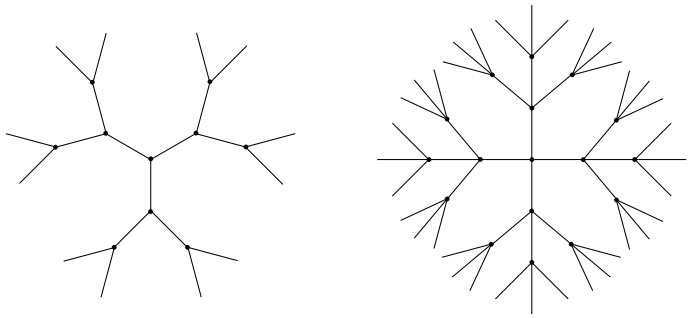

Figure A.1: Cutout of a Bethe lattice with $z = 3$ (left) and with $z = 4$ (right). The sites of the lattice are represented by dots.

We consider the general Hamiltonian

$$\boldsymbol{H}_{\text{Bethe}} = \frac{1}{\sqrt{z}} \sum_{<i,j>} \sum_{\alpha\beta} l^{\alpha\beta} \boldsymbol{S}_i^{\alpha} \boldsymbol{S}_j^{\beta} \tag{A.1}$$

with arbitrary couplings $l^{\alpha\beta}$ allowing for anisotropy. Since we have infinite temperature corresponding to $\boldsymbol{\rho} = \mathbb{1}/d$, the correlation functions simplify to the trace

$$g_{k0}^{\rho\gamma}(t) = \langle \boldsymbol{S}_k^{\rho}(t) \boldsymbol{S}_0^{\gamma}(0) \rangle = \frac{1}{d} \text{Tr} \left(\boldsymbol{S}_k^{\rho}(t) \boldsymbol{S}_0^{\gamma}(0) \right). \tag{A.2}$$

With aid of the Heisenberg equation of motion

$$\frac{\mathrm{d}}{\mathrm{d}t} \boldsymbol{A}(t) = \mathtt{i} \left[\boldsymbol{H}, \boldsymbol{A}(t) \right] = -\boldsymbol{L}\boldsymbol{A}(t), \tag{A.3}$$

where $\boldsymbol{L}$ denotes the Liouville operator, we compute the first time derivative

$$\frac{\mathrm{d}}{\mathrm{d}t} g_{i0}^{\rho\gamma}(t) = \langle \boldsymbol{L}\boldsymbol{S}_k^{\rho}(t) \boldsymbol{S}_0^{\gamma}(0) \rangle = -\frac{1}{\sqrt{z}} \sum_{j,<j,k>} \sum_{\alpha\beta\varphi} l^{\alpha\beta} \epsilon_{\alpha\rho\varphi} \langle \left[\boldsymbol{S}_j^{\beta} \boldsymbol{S}_k^{\varphi} \right] (t) \boldsymbol{S}_0^{\gamma}(0) \rangle. \tag{A.4}$$

Apparently, a single action of the Liouville operator onto $\boldsymbol{S}_k^\rho$ multiplies another spin operator at a surrounding site j to it. Similarly, applying $\boldsymbol{L}$ once more produces terms with three spin operators. Therefore, multiple actions of $\boldsymbol{L}$ lead to complex clusters $\boldsymbol{C}$ which consist of spin operators at certain sites $p \in C$ of the lattice. To determine the scaling of the correlation function $g_{k0}^{\rho\gamma}(t)$ we require details about any of those clusters because they are clearly connected to $\boldsymbol{S}_k^\rho(t)$ through (A.3) and vice versa. Thus, it is expedient to determine the scaling of the general correlation function

$$g^\gamma(\boldsymbol{C}, t) = \langle \boldsymbol{C}(t) \boldsymbol{S}_0^\gamma(0) \rangle \tag{A.5}$$

rather than that of the special case. For the corresponding derivative we find

$$\frac{\mathrm{d}}{\mathrm{d}t} g^\gamma(\boldsymbol{C}, t) = \frac{1}{\sqrt{z}} \sum_{\boldsymbol{C}'} l\left(\boldsymbol{C}, \boldsymbol{C}'\right)\, g^\gamma(\boldsymbol{C}', t), \tag{A.6}$$

where the sum runs over any clusters $\boldsymbol{C}'$, that can be reached from $\boldsymbol{C}$ by a single commutation with the Hamiltonian. The factor $l(C, C')$ denotes the corresponding coupling multiplied by any other factors resulting from the commutation. Now, it is the strategy to claim a scaling of the general correlation functions and subsequently show that an action of $\boldsymbol{L}$ according to (A.6) does not violate this claim. Before performing this, we find some general statements quantifying the clusters in the following.

First of all, since $s = \frac{1}{2}$, any product of spin operators at a single site can be referred back to a single spin operator or the unity because the product of two Pauli matrices obeys

$$\underline{\underline{\sigma}}^\alpha \underline{\underline{\sigma}}^\beta = \delta_{\alpha\beta} \underline{\underline{\sigma}}_0 + \mathtt{i} \sum_\gamma \epsilon_{\alpha\beta\gamma} \underline{\underline{\sigma}}^\gamma. \tag{A.7}$$

Correspondingly, we only need to distinguish between empty or occupied sites in our clusters.

Secondly, it is usefull to introduce a quantity

$$\kappa(\boldsymbol{C}) = \kappa_1(\boldsymbol{C}) + \kappa_2(\boldsymbol{C}), \tag{A.8}$$

characterizing the spread of a cluster $\boldsymbol{C}$ on the Bethe lattice. We denote $\kappa_1(\boldsymbol{C})$ as the minimum number of links, that are required to reach all occupied sites $p \in C$ and moreover $p = 0$. The number of non-occupied sites that are covered by this set of links (henceforth called covering) is captured by $\kappa_2(\boldsymbol{C})$. For clarity, we provide an example in Fig. A.2, where we consider a cluster consisting of four spin operators. By connecting the occupied sites and $p = 0$ as demanded, we count $\kappa_1 = 6$ required links. Moreover, we find $\kappa_2 = 3$ as the number of empty sites in this covering. Finally, this results in $\kappa = 9$. In fact, these definitions are unique for the Bethe lattice because it is a loop-free. Considering other lattices one possibly requires more precise constraints for them.

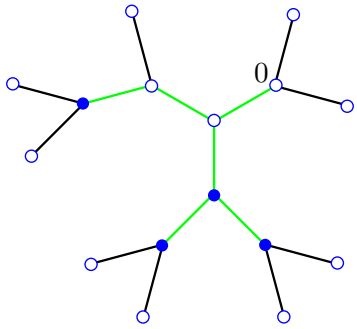

Figure A.2: Cutout of a Bethe lattice with $z = 3$ and spin-$\frac{1}{2}$. A site can either be occupied (filled circle) or empty (unfilled circle). The covering is illustrated by the green links.

Indeed, $\kappa(\boldsymbol{C})$ describes the minimum number of commutations, that are necessary to reach the cluster $\boldsymbol{C}$ from $\boldsymbol{S}_0^\gamma$ and vice versa. Particularly, at $t = 0$ one finds

$$g^\gamma(\boldsymbol{C}, 0) = 0, \qquad \forall \boldsymbol{C} \neq \boldsymbol{S}_0^\gamma, \tag{A.9}$$

and because of this

$$\frac{\mathrm{d}^n}{\mathrm{d}t^n} g^\gamma(\boldsymbol{C}, t)\Big|_{t=0} = 0 \tag{A.10}$$

for any $n < \kappa(\boldsymbol{C})$, since $\boldsymbol{S}_0^\gamma$ cannot be reached from $\boldsymbol{C}$ with less than $\kappa(\boldsymbol{C})$ commutations. In the following, we determine the scaling of $g^\gamma(\boldsymbol{C}, t)$.

The claim is that the general correlation functions are suppressed with the number of nearest neighbors according to

$$g^\gamma(\boldsymbol{C}, t) \propto \frac{1}{z^{\kappa(\boldsymbol{C})/2}}. \tag{A.11}$$

We show that this is consistent with the equations of motion (A.6) by proving that the scaling of the right-hand-side is equal to that of the left-hand-side. To this end, we consider all possible processes leading from $\boldsymbol{C}$ to $\boldsymbol{C}'$. Clearly, an action of the Liouville operator onto $\boldsymbol{C}$ only affects a single link (i, j) of the cluster. Accordingly, we consider the link processes illustrated in Fig. A.3. The corresponding commutations read

$$\begin{aligned}
\left[\boldsymbol{S}_i^\alpha \boldsymbol{S}_j^\beta, \boldsymbol{S}_i^\rho\right] &= \mathtt{i} \sum_\omega \epsilon_{\alpha\rho\omega} \boldsymbol{S}_i^\omega \boldsymbol{S}_j^\beta, && \rho \neq \alpha, \\
\left[\boldsymbol{S}_i^\alpha \boldsymbol{S}_j^\beta, \boldsymbol{S}_j^\rho\right] &= \mathtt{i} \sum_\omega \epsilon_{\beta\rho\omega} \boldsymbol{S}_i^\alpha \boldsymbol{S}_j^\omega, && \rho \neq \beta,
\end{aligned} \tag{A.12a}$$

$$\begin{aligned}
\left[\boldsymbol{S}_i^\alpha \boldsymbol{S}_j^\beta, \boldsymbol{S}_i^\rho \boldsymbol{S}_j^\beta\right] &= \frac{\mathtt{i}}{2} \sum_\omega \epsilon_{\alpha\rho\omega} \boldsymbol{S}_i^\omega, && \rho \neq \alpha, \\
\left[\boldsymbol{S}_i^\alpha \boldsymbol{S}_j^\beta, \boldsymbol{S}_i^\alpha \boldsymbol{S}_j^\delta\right] &= \frac{\mathtt{i}}{2} \sum_\omega \epsilon_{\beta\delta\omega} \boldsymbol{S}_j^\omega, && \rho \neq \beta,
\end{aligned} \tag{A.12b}$$

where the left-hand-side represents $\boldsymbol{LC}$ while the right-hand-side represents the resulting cluster $\boldsymbol{C}'$. Obviously, we do not insert the total clusters $\boldsymbol{C}$ to these equations, since only single links are participating in the commutations.

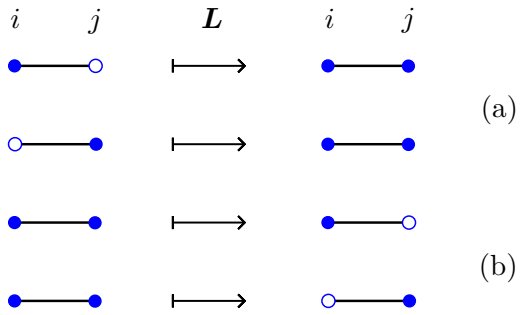

Figure A.3: All possible link processes leading from $\boldsymbol{C}$ to $\boldsymbol{C}'$. Here, we do not distinguish between links that are part of the covering and links that are not.

Moreover, a process where both sites are occupied before and after applying the Liouville operator, is not considered, since the belonging commutation yields zero according to

$$\left[\boldsymbol{S}_i^\alpha \boldsymbol{S}_j^\beta, \boldsymbol{S}_i^\rho \boldsymbol{S}_j^\delta\right] = [\boldsymbol{S}_i^\alpha, \boldsymbol{S}_i^\rho]\ \boldsymbol{S}_j^\beta \boldsymbol{S}_j^\delta + \boldsymbol{S}_i^\rho \boldsymbol{S}_i^\alpha\ \left[\boldsymbol{S}_j^\beta, \boldsymbol{S}_j^\delta\right] \tag{A.13a}$$

$$= \mathtt{i} \sum_\omega \epsilon_{\alpha\rho\omega} \boldsymbol{S}_i^\omega\ \frac{\mathtt{i}}{2} \sum_\chi \epsilon_{\beta\delta\chi} \boldsymbol{S}_j^\chi + \frac{\mathtt{i}}{2} \sum_\omega \epsilon_{\rho\alpha\omega} \boldsymbol{S}_i^\omega\ \mathtt{i} \sum_\chi \epsilon_{\beta\delta\chi} \boldsymbol{S}_j^\chi \tag{A.13b}$$

$$= -\frac{1}{2} \sum_{\omega,\chi} \epsilon_{\beta\delta\chi} \Big(\epsilon_{\alpha\rho\omega} + \epsilon_{\rho\alpha\omega}\Big) \boldsymbol{S}_i^\omega \boldsymbol{S}_j^\chi = 0, \tag{A.13c}$$

where $\alpha \neq \rho$ and $\beta \neq \delta$. Note that we used (A.7) for this calculation and thus restricted the spin to $s = \frac{1}{2}$. For larger spins this process may contribute. Turning back to the non-zero commutators (A.12), we remind the reader of coupling constants and importantly a $z^{-1/2}$ resulting from the Hamiltonian (A.1) and not explicitly appearing in the equations. While considering this we discuss the scaling of the link processes due to their multiplicity below.

The processes (A.12a) describe an occupation of an empty site next to an occupied site. Corresponding to our characterization (A.8) we distinguish between (a.i) an occupation expanding the covering of $\boldsymbol{C}$ over the lattice and (a.ii) an occupation at a site, which is already part of the covering. These cases are illustrated in Fig. A.4.

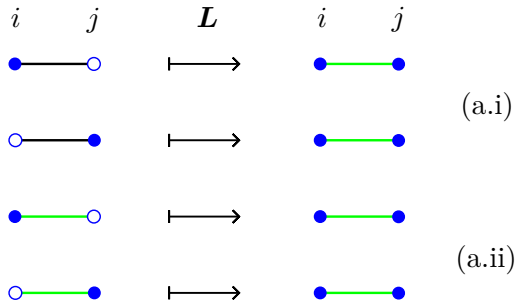

Figure A.4: All possible link processes of category (a). Links of the covering are drawn in green.

(a.i) In the first case, clearly κ_1 increases by one due to the additional link. The number of non-occupied sites κ_2, however, is not affected. In conclusion this leads to

$$\kappa(\boldsymbol{C}') = \kappa(\boldsymbol{C}) + 1. \tag{A.14}$$

Furthermore, there are at maximum z neighbors of an occupied site from which $\boldsymbol{C}$ can be expanded. This number is multiplied to the number of occupied sites

$$P_{\max}(\boldsymbol{C}) = \kappa_1(\boldsymbol{C}) - \kappa_2(\boldsymbol{C}) + 1, \tag{A.15}$$

which serve as an upper limit for the multitude of resulting terms. Together with the prefactor $z^{-1/2}$ by the Hamiltonian and (A.14) this leads to

$$P_{\max}(\boldsymbol{C})\frac{z}{\sqrt{z}}\frac{1}{z^{\kappa(\boldsymbol{C}')/2}} = P_{\max}(\boldsymbol{C})\frac{1}{z^{\kappa(\boldsymbol{C})/2}} \propto \frac{1}{z^{\kappa(\boldsymbol{C})/2}}, \tag{A.16}$$

where we omitted $P_{\max}(\boldsymbol{C})$, since it is not related to the coordination number. Thus, the claim is not violated by this process.

(a.ii) An occupation of an empty site, which is already covered by the cluster, clearly reduces κ_2 by one and keeps κ_1 constant, since the cluster is not expanded. Correspondingly, the characteristic quantity of the resulting cluster yields

$$\kappa(\boldsymbol{C}') = \kappa(\boldsymbol{C}) - 1. \tag{A.17}$$

Moreover, $\kappa_1(\boldsymbol{C})$ serves as an upper limit for the number of possibilities to fill an empty site by this process. To comprehend this, consider an extremal case, e.g., a chain with alternating occupied and empty sites. There, an occupation can take place at every of the links. Thus, the total number of possibilities is κ_1 for this case. In conclusion, the scaling for the considered process yields

$$\kappa_1(\boldsymbol{C})\frac{1}{\sqrt{z}}\frac{1}{z^{\kappa(\boldsymbol{C}')/2}} = \kappa_1(\boldsymbol{C})\frac{1}{z^{\kappa(\boldsymbol{C})/2}} \propto \frac{1}{z^{\kappa(\boldsymbol{C})/2}}, \tag{A.18}$$

which is again consistent with the claim (A.11).

Apparently, by (A.12b) an occupied site can be emptied next to another occupied site. We distinguish between processes, where (b.i) the covering of $\boldsymbol{C}$ is decreased, and those, where (b.ii) it stays unchanged, see Fig. A.5. Moreover, we assign any process where the site $p = 0$ is emptied to case (b.ii), since $p = 0$ is per definition part of the covering.

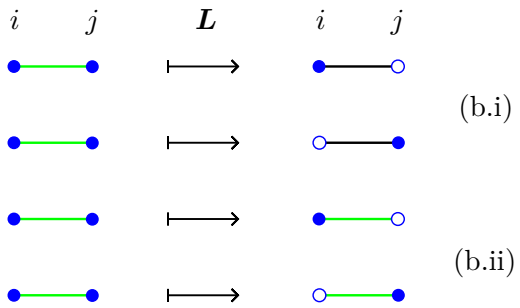

Figure A.5: All possible link processes of category (b). Links of the covering are drawn in green.

(b.i) Emptying a site at the edge of the cluster leads to a reduction of κ_1 by one. As κ_2 is not affected, we have

$$\kappa(\boldsymbol{C}') = \kappa(\boldsymbol{C}) - 1. \tag{A.19}$$

Furthermore, there can be at maximum $\propto P_{\max}$ possibilities for such a process for any cluster, since the number of occupied edge sites is limited by this. Correspondingly, we obtain

$$P_{\max}(\boldsymbol{C})\frac{1}{\sqrt{z}}\frac{1}{z^{\kappa(\boldsymbol{C}')/2}} = P_{\max}(\boldsymbol{C})\frac{1}{z^{\kappa(\boldsymbol{C})/2}} \propto \frac{1}{z^{\kappa(\boldsymbol{C})/2}} \tag{A.20}$$

for the scaling, which is consistent with the statement (A.11).

(b.ii) When emptying a site without changing the covering of the cluster, clearly κ_2 is increased by one while κ_1 stays constant. Hence, these processes lead to

$$\kappa(\boldsymbol{C}') = \kappa(\boldsymbol{C}) + 1. \tag{A.21}$$

We determine $\propto 2\kappa_1$ to be the upper limit for the number of possibilities. An extremal case for this is, e.g., a fully occupied chain. Every inner site can be emptied through both neighbors leading to $\propto 2\kappa_1$ possibilities. In conclusion, we find

$$2\kappa_1\frac{1}{\sqrt{z}}\frac{1}{z^{\kappa(\boldsymbol{C}')/2}} = 2\kappa_1\frac{1}{z^{\kappa(\boldsymbol{C})/2+1}} \propto \frac{1}{z^{\kappa(\boldsymbol{C})/2+1}}. \tag{A.22}$$

This scaling is clearly subdominant against the claim (A.11) and thus does not violate it.

Summarizingly, the claim is consistent with the equations of motion (A.6). By means of the starting conditions (A.9) and

$$g^\gamma(\boldsymbol{S}_0^\gamma, 0) = \langle \boldsymbol{S}_0^\gamma \boldsymbol{S}_0^\gamma \rangle = \frac{1}{4} \propto 1, \tag{A.23}$$

we showed that

$$g^{\gamma}(\boldsymbol{C},t) \propto \frac{1}{z^{\kappa(\boldsymbol{C})/2}} \tag{A.24}$$

is valid because $\kappa(\boldsymbol{S}_0^{\gamma}) = 0$. Thus, the pair-correlations $g_{k0}^{\rho\gamma}(t)$, $k \neq 0$, are suppressed with at least z^{-1} relative to the autocorrelations. Assuming a Gaussian behavior of the dynamic mean-field is therefore certainly justified. Moreover, the second moments of the collective field

$$\boldsymbol{V}^{\alpha}(t) = \frac{1}{\sqrt{z}} \sum_{i,<i,0>} \sum_{\gamma} l^{\alpha\gamma} \boldsymbol{S}_i^{\gamma}(t) \tag{A.25}$$

yield

$$\langle \boldsymbol{V}^{\alpha}(t)\boldsymbol{V}^{\beta}(0)\rangle = \frac{1}{z} \sum_{\substack{i,<i,0>\\ j,<j,0>}} \sum_{\gamma\rho} \left(l^{\alpha\gamma} l^{\beta\rho}\right)^2 \langle \boldsymbol{S}_i^{\gamma}(t)\boldsymbol{S}_j^{\rho}(0)\rangle \tag{A.26a}$$

$$= \frac{1}{z} \sum_{\gamma\rho} \left(l^{\alpha\gamma} l^{\beta\rho}\right)^2 \left(\overbrace{\sum_{i,<i,0>}}^{\propto z} \underbrace{\langle \boldsymbol{S}_i^{\gamma}(t)\boldsymbol{S}_i^{\rho}(0)\rangle}_{\propto 1} + \overbrace{\sum_{\substack{i,<i,0>\\ j,<j,0>\\ i\neq j}}}^{\propto z^2} \underbrace{\langle \boldsymbol{S}_i^{\gamma}(t)\boldsymbol{S}_j^{\rho}(0)\rangle}_{\propto z^{-2}} \right) \tag{A.26b}$$

$$= \frac{1}{z} \sum_{\gamma\rho} \sum_{i,<i,0>} \left(l^{\alpha\gamma} l^{\beta\rho}\right)^2 \langle \boldsymbol{S}_i^{\gamma}(t)\boldsymbol{S}_i^{\rho}(0)\rangle + \mathcal{O}\left(z^{-1}\right). \tag{A.26c}$$

Thus, the sum over the pair-correlations is suppressed and can be neglected for large z.

Clearly, the Bethe lattice differs substantially from the surface-spin system considered in this thesis. Both the topology and the range of the interaction are not comparable. However, one could see the nearest-neighbor interaction in the Bethe lattice for large z as a simple realization of the long-range interaction which is present in the surface-spin system. Local fluctuations of the coupling constants could be added to the consideration above and would not change the scaling in the end. Therefore, we adopt this appendix as an analytical argument supporting S-DMFT for the considered surface-spin system. By means of (A.24), we justified that the mean-field is Gaussian, see step 2, and moreover that only the autocorrelations contribute to the dynamics, see step 3.

B Experimental data

In this appendix we intend to list the received experimental data [25].

Table B.1: Experimental data for the spin polarization $P_{\mathrm{e}}^{xx}(t) = 4g_{\mathrm{e}}^{xx}(t)$ in transversal direction and its standard deviation $\Delta P_{\mathrm{e}}^{xx}$ in dependence of the time [25].

$t/\mu\mathrm{s}$	P_{e}^{xx}	$t/\mu\mathrm{s}$	P_{e}^{xx}
0.122	0.969 ± 0.047	0.73	0.264 ± 0.096
0.154	0.976 ± 0.042	0.762	0.174 ± 0.097
0.186	0.754 ± 0.061	0.794	0.033 ± 0.076
0.218	0.679 ± 0.06	0.826	0.051 ± 0.056
0.25	0.851 ± 0.098	0.858	0.13 ± 0.072
0.282	0.564 ± 0.086	0.89	0.133 ± 0.086
0.314	0.726 ± 0.093	0.922	0.072 ± 0.067
0.346	0.63 ± 0.09	0.954	0.138 ± 0.076
0.378	0.53 ± 0.041	0.986	-0.015 ± 0.061
0.41	0.562 ± 0.069	1.018	-0.042 ± 0.08
0.442	0.551 ± 0.075	1.05	-0.04 ± 0.073
0.474	0.451 ± 0.039	1.082	-0.025 ± 0.064
0.506	0.578 ± 0.088	1.114	-0.06 ± 0.089
0.538	0.353 ± 0.061	1.146	-0.027 ± 0.053
0.57	0.403 ± 0.041	1.178	-0.043 ± 0.098
0.602	0.381 ± 0.082	1.21	0.034 ± 0.088
0.634	0.286 ± 0.05	1.242	0.067 ± 0.049
0.666	0.305 ± 0.068	1.274	-0.142 ± 0.046
0.698	0.171 ± 0.073	1.306	-0.106 ± 0.056

Table B.2: Experimental data for the spin polarization $P_e^{zz}(t) = 4g_e^{zz}(t)$ in longitudinal direction and its standard deviation ΔP_e^{zz} in dependence of the time. The red data are selected to apply optimized fits (B) [25].

$t/\mu s$	P_e^{zz}	$t/\mu s$	P_e^{zz}
1.8	0.982 ± 0.072	76.8	0.132 ± 0.15
5.57	0.675 ± 0.085	80.55	0.183 ± 0.166
9.29	0.655 ± 0.08	84.3	-0.112 ± 0.156
13.06	0.604 ± 0.093	88.05	0.11 ± 0.163
16.83	0.553 ± 0.086	91.8	0.012 ± 0.231
20.55	0.528 ± 0.086	95.55	0.077 ± 0.174
24.32	0.378 ± 0.085	99.3	-0.075 ± 0.133
28.09	0.021 ± 0.091	103.05	0.282 ± 0.154
31.8	0.287 ± 0.072	106.8	0.02 ± 0.132
35.57	0.359 ± 0.093	110.55	-0.018 ± 0.2
39.34	0.341 ± 0.105	114.3	0.124 ± 0.157
43.06	0.259 ± 0.097	118.05	-0.167 ± 0.144
46.83	0.206 ± 0.097	121.8	-0.18 ± 0.151
50.55	0.287 ± 0.14	125.55	-0.034 ± 0.139
54.3	0.1 ± 0.13	129.3	-0.048 ± 0.184
58.05	0.069 ± 0.165	133.05	0.114 ± 0.157
61.8	0.144 ± 0.144	136.8	-0.131 ± 0.137
65.55	0.126 ± 0.185	140.55	-0.016 ± 0.171
69.3	0.04 ± 0.132	144.3	-0.335 ± 0.175
73.05	0.058 ± 0.153	148.05	-0.054 ± 0.161

C Numerical data

This appendix contains the values of the iteration errors discussed in Sec. 4.1.3 as well as the final results of the comparison between the numerical and experimental data in the strong-field regime, see Sec. 4.2.4.

Table C.1: Values of the iteration Error ΔI^{xx} given by (4.37) during the iteration-steps $(n) \to (n+1)$ for different initial functions (4.40). The iteration is stopped, when the threshold (4.39) is reached.

$(n+1)$	$\Delta I^{xx}(f_{\mathrm{Exp}})$	$\Delta I^{xx}(f_{\mathrm{Gau}})$	$\Delta I^{xx}(f_{\mathrm{Lin}})$
2	0.000 87	0.000 95	0.0017
3	0.000 25	0.000 29	0.000 24

Table C.2: Values of the iteration Error ΔI^{zz} given by (4.37) during the iteration-steps $(n) \to (n+1)$ for different initial functions (4.40). The iteration is stopped, when the threshold (4.39) is reached.

$(n+1)$	$\Delta I^{zz}(f_{\mathrm{Exp}})$	$\Delta I^{zz}(f_{\mathrm{Gau}})$	$\Delta I^{zz}(f_{\mathrm{Lin}})$
2	0.046	0.069	0.14
3	0.000 49	0.000 51	0.0022
4	0.000 25	0.000 25	0.000 24

Table C.3: Values of the coupling constant J_Q, transversal least-square error (4.72), Gaussian fit parameter μ, RMS field (4.73) and average minimum dipole distance (4.74) in dependence of the noise parameter C.

C	$J_\mathrm{Q}/\,\mu\mathrm{s}^{-1}$	χ^{xx}	$\mu/\,J_\mathrm{Q}^2$	$B_\mathrm{N}/\,\mu\mathrm{T}$	$r_\mathrm{min}/\,\mathrm{nm}$
5.8	0.2627	1.5882	49.18 ± 0.02	14.39	6.5
6.0	0.2586	1.5884	50.78 ± 0.02	14.4	6.54
6.2	0.2545	1.5885	52.38 ± 0.02	14.41	6.57
6.4	0.2508	1.5883	53.98 ± 0.02	14.43	6.61
6.6	0.2471	1.5886	55.58 ± 0.02	14.44	6.64
6.8	0.2436	1.5887	57.18 ± 0.02	14.45	6.67
7.0	0.2403	1.5889	58.78 ± 0.02	14.46	6.7
7.2	0.2371	1.589	60.38 ± 0.02	14.47	6.73
7.4	0.234	1.589	61.98 ± 0.02	14.48	6.76
7.6	0.2311	1.5891	63.58 ± 0.02	14.49	6.79
7.8	0.2282	1.5893	65.18 ± 0.02	14.49	6.82
8.0	0.2254	1.5894	66.78 ± 0.02	14.5	6.84
8.2	0.2228	1.5893	68.38 ± 0.02	14.51	6.87

Table C.4: Values of the longitudinal least-square error for considering all data (A) and for considering selected data (B) in dependence of the noise parameter C.

C	$\chi^{zz}_{(\mathrm{A})}$	$\chi^{zz}_{(\mathrm{B})}$
5.8	0.9372	0.5465
6.0	0.9263	0.4835
6.2	0.9275	0.4264
6.4	0.937	0.4003
6.6	0.9481	0.3789
6.8	0.9733	0.3698
7.0	0.9944	0.3741
7.2	1.0329	0.3916
7.4	1.0759	0.4155
7.6	1.1145	0.4442
7.8	1.153	0.4819
8.0	1.2066	0.5326
8.2	1.2616	0.5901

Bibliography

[1] D. Loss and D. P. DiVincenzo, "Quantum computation with quantum dots", Phys. Rev. A **57**, 120 (1998).

[2] D. P. DiVincenzo, "The physical implementation of quantum computation", Fortschr. Phys. **48**, 771 (2000).

[3] J. Schliemann, A. Khaetskii, and D. Loss, "Electron spin dynamics in quantum dots and related nanostructures due to hyperfine interaction with nuclei", J. Phys. Condens. Matter **15**, R1809 (2003).

[4] B. Urbaszek, X. Marie, T. Amand, O. Krebs, P. Voisin, P. Maletinsky, A. Hogele, and A. Imamoglu, "Nuclear spin physics in quantum dots: an optical investigation", Rev. Mod. Phys. **85**, 79 (2013).

[5] M. Gaudin, "Diagonalisation d'une classe d'hamiltoniens de spin", J. Phys. France **37**, 1087 (1976).

[6] M. Gaudin, *La fonction d'onde de bethe* (Masson, Paris, 1983).

[7] A. V. Khaetskii, D. Loss, and L. Glazman, "Electron spin decoherence in quantum dots due to interaction with nuclei", Phys. Rev. Lett. **88**, 186802 (2002).

[8] I. A. Merkulov, A. L. Efros, and M. Rosen, "Electron spin relaxation by nuclei in semiconductor quantum dots", Phys. Rev. B **65**, 205309 (2002).

[9] G. Chen, D. L. Bergman, and L. Balents, "Semiclassical dynamics and long-time asymptotics of the central-spin problem in a quantum dot", Phys. Rev. B **76**, 45312 (2007).

[10] B. Fauseweh, P. Schering, J. Hüdepohl, and G. S. Uhrig, "Efficient algorithms for the dynamics of large and infinite classical central spin models", Phys. Rev. B **96**, 054415 (2017).

[11] R. van den Berg, G. P. Brandino, O. E. Araby, R. M. Konik, V. Gritsev, and J.-S. Caux, "Competing interactions in semiconductor quantum dots", Phys. Rev. B **90**, 155117 (2014).

[12] J. R. Maze, P. L. Stanwix, J. S. Hodges, S. Hong, J. M. Taylor, P. Cappellaro, L. Jiang, M. V. G. Dutt, E. Togan, A. S. Zibrov, A. Yacoby, R. L. Walsworth, and M. D. Lukin, "Nanoscale magnetic sensing with an individual electronic spin in diamond", Nature **455**, 644 (2008).

[13] G. Balasubramanian, I. Y. Chan, R. Kolesov, M. Al-Hmoud, J. Tisler, C. Shin, C. Kim, A. Wojcik, P. R. Hemmer, A. Krueger, T. Hanke, A. Leitenstorfer, R. Bratschitsch, F. Jelezko, and J. Wrachtrup, "Nanoscale imaging magnetometry with diamond spins under ambient conditions", Nature **455**, 648 (2008).

[14] J. Holzgrafe, J. Beitner, D. Kara, H. S. Knowles, and M. Atatüre, "Error corrected spin-state readout in a nanodiamond", npj Quantum Inf. **5**, 13 (2019).

[15] A. Gruber, A. Dräbenstedt, C. Tietz, L. Fleury, J. Wrachtrup, and C. von Borczyskowski, "Scanning confocal optical microscopy and magnetic resonance on single defect centers", Science **276**, 2012 (1997).

[16] F. Jelezko and J. Wrachtrup, "Single defect centres in diamond: a review", phys. stat. sol. (a) **203**, 3207 (2006).

[17] G. Balasubramanian, P. Neumann, D. Twitchen, M. Markham, R. Kolesov, N. Mizuochi, J. Isoya, J. Achard, J. Beck, J. Tissler, V. Jacques, P. R. Hemmer, F. Jelezko, and J. Wrachtrup, "Ultralong spin coherence time in isotopically engineered diamond", Nature Mater. **8**, 383 (2009).

[18] R. Schirhagl, K. Chang, M. Loretz, and C. L. Degen, "Proposed spin amplification for magnetic sensors employing crystal defects", Annu. Rev. Phys. Chem. **65**, 83 (2014).

[19] T. Rosskopf, A. Dussaux, K. Ohashi, M. Loretz, R. Schirhagl, H. Watanabe, S. Shikata, K. M. Itoh, and C. L. Degen, "Investigation of surface magnetic noise by shallow spins in diamond", Phys. Rev. Lett. **112**, 147602 (2014).

[20] B. Grotz, J. Beck, P. Neumann, B. Naydenov1, R. Reuter, F. Reinhard, F. Jelezko, J. Wrachtrup, D. Schweinfurth, and B. Sarkar, "Sensing external spins with nitrogen-vacancy diamond", New J. Phys. **13**, 055004 (2011).

[21] M. S. Grinolds, M. Warner, K. D. Greve, Y. Dovzhenko, L. Thiel, R. L. Walsworth, S. Hong, P. Maletinsky, and A. Yacoby, "Subnanometre resolution in three-dimensional magnetic resonance imaging of individual dark spins", Nature Nanotech. **9**, 279 (2014).

[22] B. A. Myers, A. Das, M. C. Dartiailh, K. Ohno, D. D. Awschalom, and A. C. B. Jayich, "Probing surface noise with depth-calibrated spins in diamond", Phys. Rev. Lett. **113**, 027602 (2014).

[23] A. O. Sushkov, I. Lovchinsky, N. Chisholm, R. L. Walsworth, H. Park, and M. D. Lukin, "Magnetic resonance detection of individual proton spins using quantum reporters", Phys. Rev. Lett. **113**, 197601 (2014).

[24] M. Schaffry, E. M. Gauger, J. J. L. Morton, and S. C. Benjamin, "Proposed spin amplification for magnetic sensors employing crystal defects", Phys. Rev. Lett. **107**, 207210 (2011).

[25] K. Rezai and A. O. Sushkov, "Private communication", (2019).

[26] A. Georges, G. Kotliar, W. Krauth, and M. J. Rozenberg, "Dynamical mean-field theory of strongly correlated fermion systems and the limit of infinite dimensions", Rev. Mod. Phys. **68**, 13 (1996).

[27] D. Vollhardt, A. Avella, and F. Mancini, "Dynamical mean-field theory of electronic correlations in models and materials", AIP Conf. Proc. **1297**, 339 (2010).

[28] K. Byczuk and D. Vollhardt, "Derivation of the curie-weiss law in dynamical mean-field theory", Phys. Rev. B **65**, 134433 (2002).

[29] J. Otsuki and Y. Kuramoto, "Dynamical mean-field theory for quantum spin systems: test of solutions for magnetically ordered states", Phys. Rev. B **88**, 024427 (2013).

[30] A. J. Bray and M. A. Moore, "Replica theory of quantum spin glasses", J. Phys. C: Solid State Phys. **13**, L655 (1980).

[31] D. R. Grempel and M. J. Rozenberg, "Fluctuations in a quantum random heisenberg paramagnet", Phys. Rev. Lett. **80**, 389 (1998).

[32] S. Sachdev and J. Ye, "Gapless spin-fluid ground state in a random quantum heisenberg magnet", Phys. Rev. Lett. **70**, 3339 (1993).

[33] A. Georges, O. Parcollet, and S. Sachdev, "Mean field theory of a quantum heisenberg spin glass", Phys. Rev. Lett. **85**, 840 (2000).

[34] M. H. Levitt, *Spin dynamics: basics of nuclear magnetic resonance* (John Wiley and Sons, Chichester, 2001).

[35] M. Fox, *Quantum optics* (Oxford University Press, Oxford, 2006).

[36] Italian Physical Society. Ed. by B. Maraviglia, *Physics of nmr spectroscopy in biology and medicine* (North-Holland, Amsterdam, 1988).

[37] S. Blanes, F. Casas, J. A. Oteo, and J. Ros, "The magnus expansion and some of its applications", Phys. Rep. **470**, 151 (2009).

[38] D. Stanek, "Dynamics and decoherence in the central spin model, From a quantum mechanical to a classical description", PhD thesis (TU Dortmund, 2013).

[39] H. Georgii, *Stochastik: einführung in die wahrscheinlichkeitstheorie und statistik* (Walter de Gruyter GmbH, Berlin/Boston, 2015).

[40] B. H. Bransden and C. J. Joachain, *Quantum mechanics*, second edition (Prentice Hall, Harlow, 2000).

[41] W. Magnus, "On the exponential solution of differential equations for a linear operator", Commun. Pure Appl. Math. **7**, 649 (1954).

[42] S. Blanes, F. Casas, J. A. Oteo, and J. Ros, "A pedagogical approach to the magnus expansion", Eur. J. Phys. **31**, 907 (2010).

[43] A. Alvermann and H. Fehske, "High-order commutator-free exponential time-propagation of driven quantum systems", J. Comput. Phys. **230**, 5930 (2011).

[44] E. N. Economou, *Green's functions in quantum physics* (Springer, Berlin, 2006).

Acknowledgements/Danksagung

At first, I want to thank Prof. Götz S. Uhrig for assigning this interesting subject to me and furthermore for his excellent mentoring. The numerous discussions helped me very much throughout the completing of this master thesis. Moreover, I want to thank Dr. Jörg Bünemann for taking over the role as the second corrector.

For the collaboration on the topic including the provision of experimental data and the reply on many detailed questions, I like to thank Kristine Rezai, Prof. Alex O. Sushkov and co-workers.

Furthermore, I'm expressing my great gratitude to Mohsen Yarmohammadi for many useful theoretical discussions and the correction of this thesis. For much computational support and many recommendations I like to thank Philipp Schering very much. Beyond this, I'm also saying thanks to my fellows Philipp Scherer and Dag-Björn Hering and further to the full chair of TIa for many talks - not only about physics - in our weekly coffee breaks.

Besonders bedanken möchte ich mich an dieser Stelle bei meinen Eltern und Geschwistern, die mich nicht nur bei der Anfertigung dieser Arbeit, sondern mein ganzes Leben lang unterstützen. Das weiß ich sehr zu schätzen. Zuletzt, aber nicht weniger, möchte ich mich sehr bei meiner Freundin Yvonne für die guten Ratschläge und die Geduld, auch wenn es mal stressig wurde, bedanken.

Eidesstattliche Versicherung
(Affidavit)

Name, Vorname
(Last name, first name)

Matrikelnr.
(Enrollment number)

Ich versichere hiermit an Eides statt, dass ich die vorliegende Bachelorarbeit/Masterarbeit* mit dem folgenden Titel selbstständig und ohne unzulässige fremde Hilfe erbracht habe. Ich habe keine anderen als die angegebenen Quellen und Hilfsmittel benutzt sowie wörtliche und sinngemäße Zitate kenntlich gemacht. Die Arbeit hat in gleicher oder ähnlicher Form noch keiner Prüfungsbehörde vorgelegen.

I declare in lieu of oath that I have completed the present Bachelor's/Master's* thesis with the following title independently and without any unauthorized assistance. I have not used any other sources or aids than the ones listed and have documented quotations and paraphrases as such. The thesis in its current or similar version has not been submitted to an auditing institution.

Titel der Bachelor-/Masterarbeit*:
(Title of the Bachelor's/ Master's* thesis):

*Nichtzutreffendes bitte streichen
(Please choose the appropriate)

Ort, Datum
(Place, date)

Unterschrift
(Signature)

Belehrung:
Wer vorsätzlich gegen eine die Täuschung über Prüfungsleistungen betreffende Regelung einer Hochschulprüfungsordnung verstößt, handelt ordnungswidrig. Die Ordnungswidrigkeit kann mit einer Geldbuße von bis zu 50.000,00 € geahndet werden. Zuständige Verwaltungsbehörde für die Verfolgung und Ahndung von Ordnungswidrigkeiten ist der Kanzler/die Kanzlerin der Technischen Universität Dortmund. Im Falle eines mehrfachen oder sonstigen schwerwiegenden Täuschungsversuches kann der Prüfling zudem exmatrikuliert werden. (§ 63 Abs. 5 Hochschulgesetz - HG -).

Die Abgabe einer falschen Versicherung an Eides statt wird mit Freiheitsstrafe bis zu 3 Jahren oder mit Geldstrafe bestraft.

Die Technische Universität Dortmund wird gfls. elektronische Vergleichswerkzeuge (wie z.B. die Software „turnitin") zur Überprüfung von Ordnungswidrigkeiten in Prüfungsverfahren nutzen.

Die oben stehende Belehrung habe ich zur Kenntnis genommen:

Official notification:
Any person who intentionally breaches any regulation of university examination regulations relating to deception in examination performance is acting improperly. This offense can be punished with a fine of up to €50,000.00. The competent administrative authority for the pursuit and prosecution of offenses of this type is the chancellor of TU Dortmund University. In the case of multiple or other serious attempts at deception, the examinee can also be unenrolled, section 63, subsection 5 of the North Rhine-Westphalia Higher Education Act (*Hochschulgesetz*).

The submission of a false affidavit will be punished with a prison sentence of up to three years or a fine.

As may be necessary, TU Dortmund will make use of electronic plagiarism-prevention tools (e.g. the "turnitin" service) in order to monitor violations during the examination procedures.

I have taken note of the above official notification:**

Ort, Datum
(Place, date)

Unterschrift
(Signature)

**Please be aware that solely the German version of the affidavit ("Eidesstattliche Versicherung") for the Bachelor's/ Master's thesis is the official and legally binding version.